

STUDENTS' SPACE ASSOCIATION
THE FACULTY OF POWER AND AERONAUTICAL ENGINEERING
WARSAW UNIVERSITY OF TECHNOLOGY



PRELIMINARY DESIGN REVIEW

ATTITUDE DETERMINATION AND CONTROL SYSTEM

Phase B of PW-Sat2 student satellite project

June 2015

Issue 2 (November 2016 update)

Revisions

Date	Changes	Responsible
2015-01-18	First issue	Paweł Jaworski
2015-05-29	Latest editorial changes	Dominik Roszkowski
2016-11-22	Corrected to new template, added disclaimer	Dominik Roszkowski

Attention Phase B documentation may be outdated in many points. Please be aware of that and do not depend on Phase B or Phase A documents only. More recent documentation is available on project website.

Published by

Students' Space Association

Warsaw University of Technology, 2015

This work is licensed on CC BY-NC 3.0

Project logo by Krzysztof Karaś

Artist's impressions by Marcin Świetlik

Quote as: PW-Sat2 Team, *Phase B Documentation – Preliminary Design Review – Attitude Determination and Control System (Issue 2)*, Students' Space Association, Warsaw University of Technology, pw-sat.pl 2015







	PW-Sat2	Preliminary Design Review	
	2016-11-22	Attitude Determination and Control System	
	Phase B		

Table of contents

1	Introduction	7
2	Phase A Review	8
3	ADCS Requirements	9
4	Hardware Description	11
4.1	Actuators.....	11
4.1.1	Magnetorquers.....	11
4.2	Sensors.....	12
4.2.1	Sun Sensor.....	13
4.2.2	Magnetometer	15
4.2.3	Gyroscope	17
4.3	Conclusions	18
5	Photodiodes	19
5.1	Algorithm	19
5.2	Visibility & Configuration.....	21
5.3	Spectral sensitivity & albedo	23
5.4	Testing.....	24
6	ADCS Architecture	26
6.1	Determination	27
6.2	Control.....	30
6.3	ADCS Modes.....	30
7	Design Analysis	33
7.1	Disturbance Torques.....	33
7.1.1	Gravity Gradient.....	33
7.1.2	Aerodynamic Torque.....	34
7.1.3	Solar Radiation Pressure Torque	36
7.1.4	Magnetic Torque	36
7.1.5	Conclusions	37
7.2	Dynamics & Kinematics.....	38
7.2.1	General Formulation	39
7.2.2	Linearized Formulation	40
7.3	Attitude Determination and Estimation	42
7.3.1	Wahba's Problem	42
7.3.2	The TRIAD Algorithm.....	43
7.3.3	The General Form of TRIAD Algorithm	43
7.3.4	Multiplicative Extended Kalman Filter (MEKF)	44
7.4	Attitude Control.....	53



	PW-Sat2	Preliminary Design Review	
	2016-11-22	Attitude Determination and Control System	
	Phase B		

7.4.1	Magnetorquers.....	53
7.4.2	Detumbling Control Mode	56
7.4.3	Sun Pointing Control Mode.....	59
8	Simulation Software	63
8.1	Overview	63
8.2	Sensors' Model	67
8.3	Simulations Results	68
8.3.1	Sun Pointing Mode.....	69
8.3.2	Detumbling Mode	80
9	Conclusions	85
10	Future Work	86
11	Appendix A Coordinate Systems	87
12	Appendix B Nomenclature	89
13	References	90

	PW-Sat2	Preliminary Design Review	
	2016-11-22	Attitude Determination and Control System	
	Phase B		



List of figures

Figure 4-1 iMTQ Board	12
Figure 4-2 OSRAM SFH2430 Photodiode	14
Figure 4-3 OSRAM SFH2430 directional characteristic	14
Figure 4-4 SSBV Sun Sensor	15
Figure 4-5 ESL Deployable Magnetometer	17
Figure 4-6 ADXRS453 Gyroscope	18
Figure 5-1 Illuminated photodiode	19
Figure 5-2 Visibility of configuration of 6 photodiodes	21
Figure 5-3 Solar radiation spectrum on Earth's surface and above the atmosphere	23
Figure 5-4 Spectral sensitivity of OSRAM SFH2430 photodiode	24
Figure 5-5 Test Stand for Sun Sensor and photodiodes testing	25
Figure 5-6 Configuration of 3 photodiodes for testing	25
Figure 6-1 ADCS Block Diagram for Sun Pointing Mode	27
Figure 6-2 Error between Earth to Sun and Satellite to Sun vectors	29
Figure 7-1 Disturbance torques dependency on orbit's altitude	38
Figure 7-2 Kalman filter cycle	45
Figure 7-3 Magnetic dipole generated by a single current loop	53
Figure 7-4 Earth's magnetic field	54
Figure 7-5 Underactuation of the magnetic control system	54
Figure 7-6 Continuous filter for input's derivative estimation	57
Figure 7-7 Time cycle for Detumbling mode	59
Figure 7-8 Spin stabilization around the satellite's X axis	60
Figure 7-9 Time cycle for Sun Pointing mode	62
Figure 8-1 Earth's magnetic field in ECI (left), Error between IGRF11 10th and 9th order in ECI (right)	63
Figure 8-2 Satellite's position and velocity in ECI based on J2 orbit propagator	64
Figure 8-3 Eclipse condition	64
Figure 8-4 Simulation software block diagram for Sun Pointing mode	66
Figure 8-5 Satellite's attitude error between true and estimated (small rotation vector norm) in Sun Pointing mode	70
Figure 8-6 Satellite's angular rate error between true and estimated (vector norm) in Sun Pointing mode	71
Figure 8-7 Satellite's angular rate in SBRF for control inputs based on EKF in Sun Pointing mode	72
Figure 8-8 Error between satellite's X axis, angular rate vector and Sun direction in Sun Pointing mode	73
Figure 8-9 Magnetic control dipole (0 in eclipse) in Sun Pointing mode	74
Figure 8-10 Power & Energy consumption in Sun Pointing mode	75
Figure 8-11 Attitude error between EKF & true and TRIAD & true (gyro integration in eclipse) for Sim. 1 & 6, small rotation vector norm	76
Figure 8-12 Angular rate error between EKF & true and gyro raw data & true for Sim. 1 & 6, vector norm	76
Figure 8-13 EKF convergence in initial 300s for Sim. 1 & 6 in Sun Pointing mode	77
Figure 8-14 Satellite's angular rate in SBRF in Detumbling mode	81
Figure 8-15 Satellite's angular rate vector norm in Detumbling mode	81
Figure 8-16 Control magnetic dipole in Detumbling mode	82
Figure 8-17 Power & Energy consumption in Detumbling mode	82
Figure 8-18 B-dot with high-pass filter (top) and without (bottom)	83
Figure 8-19 B-dot close-up in initial 300s with high-pass filter (top) and without (bottom)	83
Figure 11-1 ECI inertial and ORF orbital coordinate systems	87
Figure 11-2 SBRF satellite's body coordinate system	88

	PW-Sat2	Preliminary Design Review	
	2016-11-22	Attitude Determination and Control System	
	Phase B		



List of tables

Table 3-1 ADCS Requirements	9
Table 4-1 iMTQ Specification	12
Table 4-2 OSRAM SFH2430 Photodiode Specification	14
Table 4-3 SSBV Sun Sensor Specification	15
Table 4-4 XEN1210 Magnetometer Specification	16
Table 4-5 ESL External Magnetometer Specification	16
Table 4-6 ADXRS453 Gyroscope Specification	18
Table 6-1 ADCS on-orbit sequence	32
Table 7-1 Static, exponentially decaying atmosphere model's parameters	35
Table 7-2 MEKF Attitude and Angular Rate Estimation Algorithm	52
Table 8-1 Simulation's constant input parameters	68
Table 8-2 Variable simulation's parameters for Sun Pointing mode	69
Table 8-3 Sun Pointing mode simulations' results	78
Table 8-4 Variable simulation's parameters for Detumbling mode	80
Table 8-5 Detumbling mode simulations' results	84

	PW-Sat2	Preliminary Design Review	
	2016-11-22	Attitude Determination and Control System	
	Phase B		

Abbreviated terms

2U	2-Unit
ADCS	Attitude Determination and Control System
CAD	Computer Aided Design
CMOS	Complementary Metal-Oxide Semiconductor
COTS	Commercial Off-The-Shelf
CSS	Coarse Sun Sensor
ECI	Earth Centered Inertial
EKF	Extended Kalman Filter
FOV	Field of View
I2C	Inter-Integrated Circuit
IGRF	International Geomagnetic Reference Field
MEKF	Multiplicative Extended Kalman Filter
MEMS	Micro Electro-Mechanical Systems
MLI	Multi-Layer Insulation
MTM	Magnetometer
OBC	On-board Computer
PCB	Printed Circuit Board
PD	Proportional – Derivative
P-POD	Poly Picosatellite Orbital Deployer
PSD	Position Sensitive Device
PWM	Pulse-Width Modulation
SBRF	Satellite Body Reference Frame
SGP	Simplified General Perturbations
SSO	Sun Synchronous Orbit
TLE	Two Line Elements
TRIAD	TRLaxial Attitude Determination

	PW-Sat2	Preliminary Design Review	
	2016-11-22	Attitude Determination and Control System	
	Phase B		

1 INTRODUCTION

The main purpose of this document is to present current development of the ADCS subsystem for PW-Sat2 CubeSat. The document begins with the verification of the requirements and architecture of the ADCS in previous Phase A report from April 2014. Relevant changes are presented.

Attention Phase B documentation may be outdated in many places. Please be aware of that and do not depend on Phase B or Phase A documents only. More recent documentation is available on project website.



The major task of ADCS is pointing the deployed solar panels towards the Sun within predetermined accuracy. Thus the estimation of the attitude with the presence of noise is required. Second task of attitude control system is detumbling, i.e. deceleration satellite's rotational motion after P-POD deployment.

Since April 2014, major effort was put on testing the algorithms for attitude determination and estimation with the presence of expected sensors' noise. Moreover, attitude control strategy was changed taking into account expected disturbance torques acting on the satellite on orbit. To verify proposed approach, the simulation software was developed which utilizes environmental models, satellite dynamics and kinematics, sensors and actuators emulation with expected noise. Results for given attitude estimation and control algorithms are presented and thoroughly discussed.

The team also chose the sensors and actuators necessary for meeting the functional requirements. However, the final decision about the exact models of sensors has not been done. In the simulation software, one can modify the magnitude of sensors' errors as inputs and obtain desired performance of sensors in order to meet the overall ADCS requirements.

The comparison of several types of sensors is presented and possible trade-offs are discussed. Since purchased sensors will be COTS, low-cost, based on MEMS technology, choosing the sensors which worked properly on previous CubeSat missions is emphasized.

The photodiodes and magnetorquers have been purchased. Test stand for evaluating the photodiodes accuracy has been built. Possible configuration of photodiodes and the algorithms for determining Sun vector based on relative photodiodes measurements have been derived.

	PW-Sat2	Preliminary Design Review	
	2016-11-22	Attitude Determination and Control System	
	Phase B		



2 PHASE A REVIEW

The following problems from Phase A Report have been put into question and possible solutions have been proposed:

- Magnetorquers are not able to stabilize the attitude in ECI inertial frame when expected disturbance torques are considered. Using the reaction wheel is not considered because of mass, financial and volume constraints. Spin stabilization about the axis perpendicular to the deployed solar panels which is simultaneously collinear with the Sun direction has been examined in detail and proves to be feasible.
- With spin stabilization, the accuracy of Sun pointing can be significantly enhanced. Based on the simulations' results, Sun pointing error at the level of 5 degrees is feasible.
- Taking the pictures of the Earth is not considered, thus Nadir Pointing is not necessary.
- Accuracy of the magnetometer is crucial, so the team considers using magnetometer outside the CubeSat, on the deployable boom. This will make the measurements less sensitive to the magnetic disturbances generated by the on-board electronics.
- Simplicity of the algorithms and the system architecture is important. Number of ADCS modes has been minimized to 4 and transitions has been simplified. Also, number of photodiodes have to be minimized, even at the expense of not covering whole attitude sphere¹. Kalman filter can still estimate the attitude with only one reference measurement from the magnetometer, which takes place in eclipse when no photodiodes' outputs are available.
- The adaptation of the control gain in B-dot algorithm for detumbling mode in real-time applications is not considered. Constant gain gives satisfactory results, thus making the algorithm more complex should be avoided.

Detailed changes are presented in the following chapters.

¹ At least three photodiodes measurements are necessary to determine Sun direction using deterministic method. The normals of the photodiodes cannot be collinear. When the attitude sphere is fully covered, at least 3 photodiodes are illuminated for arbitrary Sun direction.

	PW-Sat2	Preliminary Design Review	
	2016-11-22	Attitude Determination and Control System	
	Phase B		

3 ADCS REQUIREMENTS



Taking into account changes in ADCS design approach, ADCS requirements have been refined and clarified.

The major performance requirements refer to the Sun pointing error and time of detumbling. Sensors' errors such as noise, bias, drift and temperature sensitivity contribute mostly to the whole system performance. However, the team cannot afford high precision sensors due to the financial and volume constraints. The error of attitude determination influence the control error. Based on the other subsystems requirements, simulation results presented in chapter 8 and the currently on-orbit CubeSats with similar ADCS architecture, the requirements are stated. The reader should take into account that some of these values can be changed.



Table below presents the summary of the ADCS requirements for both software and hardware. In terms of hardware - power, electrical and thermal requirements have not been examined, rather the performance has been emphasized. In next chapters, most requirements are explained in detail.

Table 3-1 ADCS Requirements

Requirement	Value	Unit
Software & General		
Control		
Sun pointing error with 2 coils working (>96% maximum solar energy)	15	deg
Detumbling possible from (angular rate vector norm) with 2 coils working	60	deg/s
Detumbling time for above condition	4	orbits
Autonomous detumbling from predetermined threshold	TBD	deg/s
control and determination algorithms must be able to run on Hercules TMS570	-	-
calculation time for one iteration during Detumbling	<20	ms
calculation time for one iteration during Sun Pointing (determination & control)	<150	ms
moment of inertia ratio about satellite X axis and Y axis	1.1	-
Determination		
attitude knowledge error in daylight (norm of small rotation vector)	<12	deg
Hardware		
Magnetorquers		
magnetic moment error of command value on each axis for operating temperature conditions	5 (3 σ)	%

	PW-Sat2	Preliminary Design Review	
	2016-11-22	Attitude Determination and Control System	
	Phase B		

switched off when magnetometer takes measurements	-	-
supply voltage	5	V
able to identify fault coil and isolate it from other subsystems components	-	-
Gyroscopes		
random noise	<0.5	deg/ \sqrt{s}
bias instability	<0.006	deg/ $\sqrt{s^3}$
scale factors & misalignments elements errors	<0.03 (σ)	-
supply voltage	3.3	V
Magnetometers		
random noise	<100 (σ)	nT
at least one redundant magnetometer is required	-	-
able to identify fault MTM and isolate it from other subsystems components	-	-
constant biases on each axis	<1000	nT
scale factors & misalignments elements errors	<0.03 (σ)	-
angle between output and true magnetic field vector	<2.5 (σ)	deg
supply voltage	3.3	V
sampling rate	>5	Hz
Photodiodes		
angle between output and true unit Sun vector	<15 (3σ)	deg
field of view (FoV) of single photodiode	>120	deg
constant biases on each axis for unit Sun vector	<0.03	-
scale factors & misalignments elements error	<0.03 (σ)	-
evident peak in spectral sensitivity between	(500,600)	nm
glass film on the photodiode's surface to protect from UV	-	-
supply voltage	3.3	V

	PW-Sat2	Preliminary Design Review	
	2016-11-22	Attitude Determination and Control System	
	Phase B		

4 HARDWARE DESCRIPTION

In this chapter, the choice of hardware is described. Each element is proven to be necessary. Possible trade-offs are presented. Detailed parameters of several sensors are compared taking into account flight heritage. The necessity of redundancy is examined.

4.1 ACTUATORS

The team has not considered the possibility of using even single reaction wheel due to financial, mass and volume constraints. Thus, it was necessary to come up with the control strategy utilizing only set of 3 perpendicular electromagnetic coils called magnetorquers. Further details on control approach are discussed in chapter 7.4. Simulation results prove that magnetorquers and spin stabilisation controller let the solar panels point the Sun with very good accuracy. Magnetorquers are widely used to detumble satellite after P-POD deployment. Since Sun tracking and detumbling are major tasks of ADCS, magnetorquers as the only actuators have been proven sufficient and thus chosen.

4.1.1 MAGNETORQUERS

Set of 3 perpendicular electromagnetic coils was purchased from ISIS (Innovative Solutions in Space). The board comprises of 2 rods and 1 air core. Temperature sensors and magnetometer are included together with control module applying PWM signal to the coils. Above elements are fabricated on single PCB and supports I2C bus.

On-board magnetometer is used for autonomous detumbling mode. However, since it is placed inside on iMTQ's PCB, not outside the CubeSat, it will be sensitive for magnetic disturbances from on-board electronics. For detumbling it is sufficient option, but for attitude estimation there are more stringent requirements. Thus the additional external magnetometer is being considered.

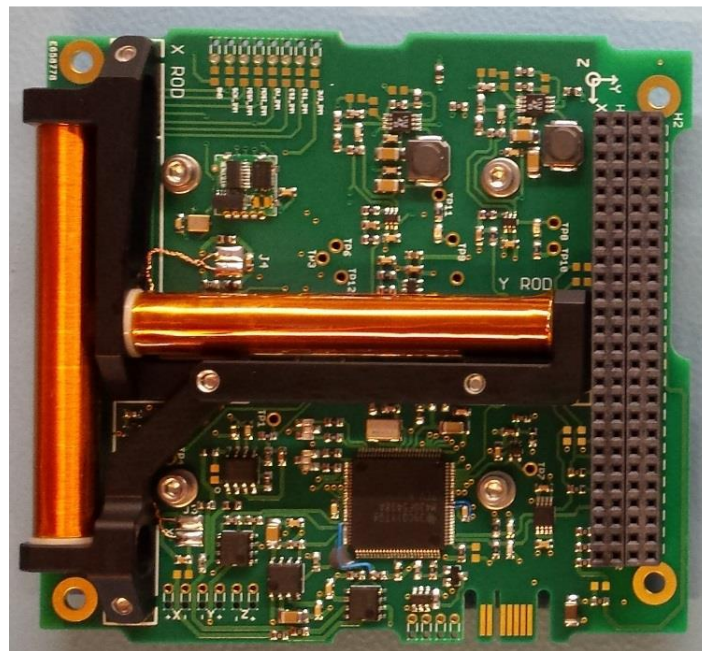


Figure 4-1 iMTQ Board



The figure above shows X & Y torque rods and I2C bus connector on the right. The Z air core is placed on the bottom side of the PCB. Table below shows overall specification of iMTQ [9].

Table 4-1 iMTQ Specification

Parameter	Value	Comment
Nominal magnetic dipole for torque rods (X, Y)	0.2 Am ²	5 V
Nominal magnetic dipole for air core (Z)	0.24 Am ²	5 V
Actuator power for rods (X, Y)	0.2 W	5 V, 20°C, 0.2 Am ²
Actuator power for air core (Z)	0.68 W	5 V, 20°C, 0.24 Am ²
Temperature sensor current consumption	<150 uA	-
Operational temperature range	-40 to +70°C	-
Mass	194 g	-

4.2 SENSORS

In Detumbling mode the magnetometer is used. The information from two subsequent samples is integrated to estimate the satellite's angular rate. The control law is simple and robust. Further details on B-Dot algorithm can be found in chapter 7.4.2.

	PW-Sat2	Preliminary Design Review	
	2016-11-22	Attitude Determination and Control System	
	Phase B		

In Sun Pointing mode the algorithm need to know current attitude and angular rate of the satellite with reference to ECI inertial frame. In order to calculate the satellite's attitude, two reference vectors are necessary (further details on Wahba's Problem in chapter 7.3.1). Comparing measured vectors with the reference vectors, the attitude can be calculated. The simplest approach widely used in practice, not only on CubeSat missions, utilizes magnetic field vector and Sun vector measurements. Thus magnetometer and Sun Sensors are necessary.

There are algorithms for estimating the angular rate of the satellite based only on magnetometer measurements [7]. However, this approach requires well-calibrated magnetometer with relatively good accuracy. The algorithm for state determination is made more complex. For these reasons, the team has decided to use a gyroscope. This approach has been proven to work well on CubeSat missions. However, attention has to be paid when testing and estimating errors of gyroscopes.

4.2.1 SUN SENSOR

Due to the financial constraints, the team is not able to purchase 6 fine Sun Sensors. Instead, coarse Sun Sensors (CSS) were chosen. Photodiodes placed at angles can provide information about the Sun direction. However, the accuracy is corrupt. Previous CubeSat missions such as AAUSat3, MaSat1 and RAX2 used a configuration of photodiodes to estimate Sun direction with success [3, 8]. OSRAM SFH2430 photodiodes have been purchased.

The possibility of purchasing one fine digital Sun Sensor is being considered. It would be placed on the face of deployed solar panels since the Sun tracking mode is the nominal ADCS mode. However, it is recommended to place it at angle, due to the biggest inaccuracies in outputs when the Sun direction coincides with Sun Sensor's normal [1].

Table below shows specification of OSRAM SFH2430 photodiode [5].



	PW-Sat2	Preliminary Design Review	
	2016-11-22	Attitude Determination and Control System	
	Phase B		

Table 4-2 OSRAM SFH2430 Photodiode Specification

Parameter	Value	Comment
Field of View (FoV)	120	-
Wavelength of max sensitivity	570 nm	-
Power dissipation	150 mW	-
Radiant sensitive area	7.02 mm ²	-
Rise and fall time	200 us	5V, 550 nm
Temperature coefficient	0.16 %/K	-
Noise equivalent power	0.033 pW/Hz ^{1/2}	-
Operating temperature range	-40 to +100 °C	-

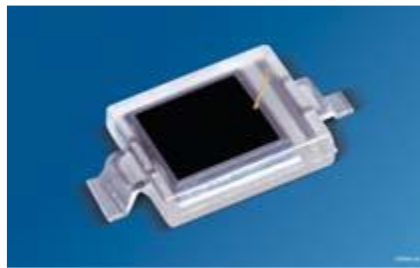


Figure 4-2 OSRAM SFH2430 Photodiode

Figure below shows the directional characteristic of OSRAM SFH2430 photodiode [5].

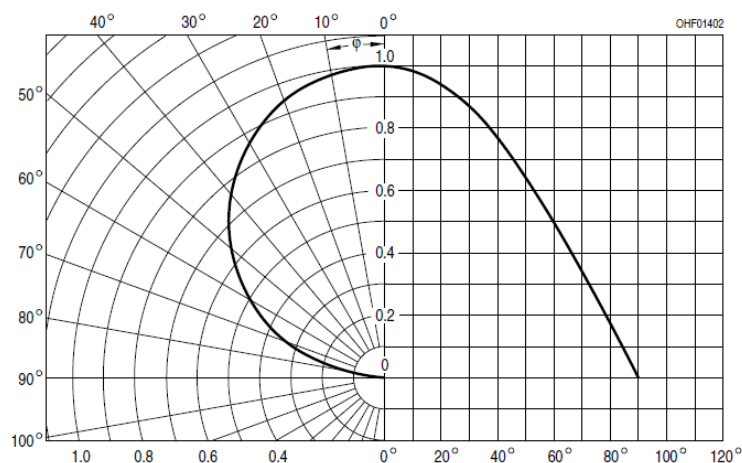




Figure 4-3 OSRAM SFH2430 directional characteristic

Above characteristic is cosine function in operating field of view. Tests will show, whether the cosine function can be used in the algorithm for calculating the Sun vector. The range of field of view corresponding to the

	PW-Sat2	Preliminary Design Review	
	2016-11-22	Attitude Determination and Control System	
	Phase B		

cosine approximation will be obtained after testing. Also the spectral sensitivity will have to be investigated. Further discussion about the photodiodes and derivation of the algorithm for extracting the Sun vector is presented in chapter 5.

Table below shows specification of considered fine digital CMOS PSD Sun Sensor from SSBV [10].

Table 4-3 SSBV Sun Sensor Specification

Parameter	Value
Field of View (FoV)	114
Accuracy	<0.5°
Update rate	>10 Hz
Operating temperature range	-25 to +50 °C
Supply voltage	5 V
Mass	< 5g
Power	<10 mA

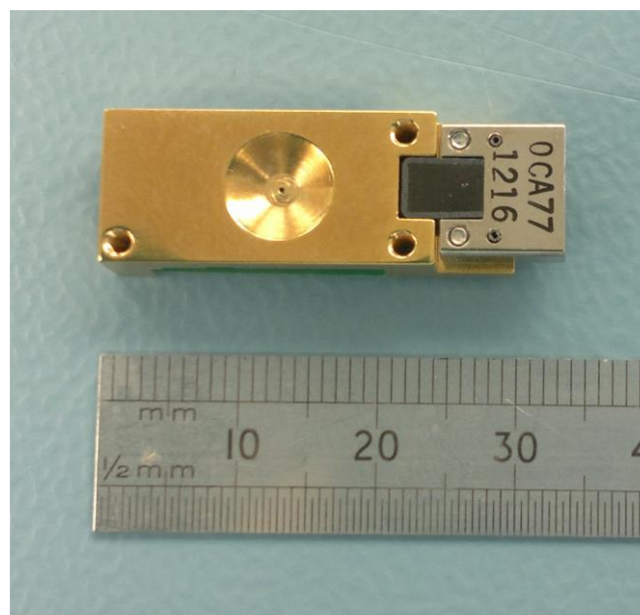




Figure 4-4 SSBV Sun Sensor

4.2.2 MAGNETOMETER

As stated in chapter 4.1.1, one magnetometer will be placed on PCB with magnetorquers. The sensor is reliable XEN1210 with flight heritage. It is single axis, based on Hall effect and was widely used with ISIS's iMTQ board. However, the need for additional, more accurate magnetometer was expressed in chapter 4.1.1. The

	PW-Sat2	Preliminary Design Review	
	2016-11-22	Attitude Determination and Control System	
	Phase B		

external magnetometer, which is less sensitive to internal disturbances is being considered to be purchased from ESL (Electronic Systems Laboratory, University of Stellenbosch). The MTM is placed on the deployable boom when the current burns the wire holding it in stowed configuration. This magnetometer is based on magneto-resistive technology. Outputs can be analogue or digital. It is currently being tested on QB50 precursor missions in ADCS subsystem.

Besides ESL magnetometer, other options are being considered. However, not deployable, rather internal magnetometers. For instance, digital ADIS16405 which was used on RAX [12].

Table below shows the specification of the internal single axis XEN1210 magnetometer [11].



Table 4-4 XEN1210 Magnetometer Specification

Parameter	Value
Field range	$\pm 63 \text{ uT}$
Bias (without calibration)	1500 nT
Noise	$55 \text{ nT}/\sqrt{\text{Hz}}$
Hysteresis	10 nT
Supply voltage	3.3 V
Resolution (24 bits)	7.5 nT/LSB
Operating temperature range	-40 to +125 °C

Table below shows the specification of the 3-axis ESL magnetometer on the deployable boom [6].

Table 4-5 ESL External Magnetometer Specification

Parameter	Value
Field range	$\pm 120 \text{ uT}$
Mass (with mounting structure)	13 g
Noise with filtering (rms)	<30 nT
Distance from base when deployed	~ 80 mm
Measurement time	2 ms
Supply voltage	3.3 V
Deployment voltage	8 V
Power consumption	33 mW

	PW-Sat2	Preliminary Design Review	
	2016-11-22	Attitude Determination and Control System	
	Phase B		

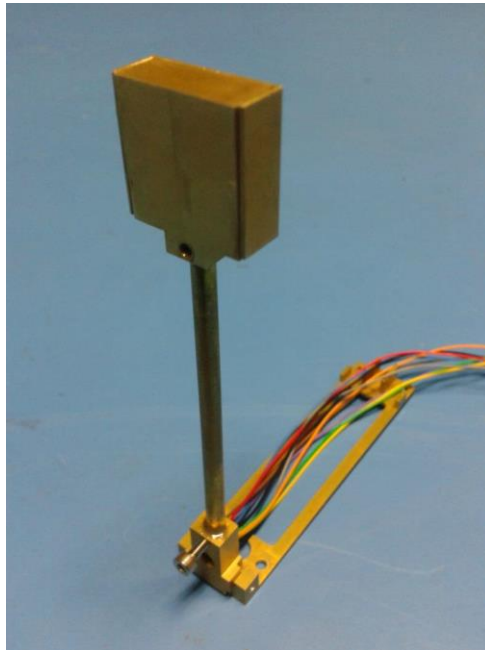


Figure 4-5 ESL Deployable Magnetometer

It should be verified, how accuracy of the magnetometer can be enhanced by placing it at the distance of 8 cm from working electronics. Moreover, the vibrations of the boom shortly after deployment have to be examined. Although they diminish quite rapidly, they may influence satellite's rotational movement. First results of QB50 precursor mission should give an insight to these problems.

4.2.3 GYROSCOPE

When choosing the gyroscope, critical performance parameters are noise, bias instability and temperature sensitivity. Digital MEMS sensors are more accurate since they usually have built-in low-pass filter and temperature compensation. Analog Devices' ADXRS453 has good performance characteristics. Sensor supports the SPI bus, so SPI to I2C bridge is required to solve the interface compatibility problems. ADXRS453 is single axis gyro, so 3 sensors, one on each orthogonal axis have to be used. This gyroscope has an excellent, low temperature sensitivity.

Table below shows the specification of the digital ADXRS453 gyroscope.



	PW-Sat2	Preliminary Design Review	
	2016-11-22	Attitude Determination and Control System	
	Phase B		

Table 4-6 ADXRS453 Gyroscope Specification

Parameter	Value	Comment
Measurement range	± 300 °/s	-
Noise density	0.015 °/s/ $\sqrt{\text{Hz}}$	at T=25 °C
	0.023 °/s/ $\sqrt{\text{Hz}}$	at T=105 °C
Bias instability	0.004 °/s	at T=40 °C
Cross-axis sensitivity	± 0.03	-
Nonlinearity	0.05 (rms)	FSR
Supply voltage	3.15 V	min
	5.25 V	max
Null output	± 0.4	at T=25 °C
Operating temperature range	-40 to $+125$ °C	-

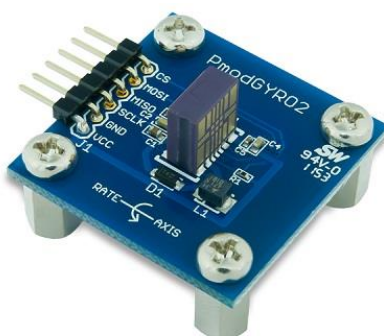




Figure 4-6 ADXRS453 Gyroscope

4.3 CONCLUSIONS

The team has to purchase several types of sensors in order to test their accuracy and performance. Precise testing procedure and means to numerically compare different sensors have to be designed. Electrical, thermal, mechanical and other environmental characteristics will have to be investigated in detail in order to assure interface compatibility with the other satellite's subsystems. In February 2015 the set of sensors for testing will be ordered.

	PW-Sat2	Preliminary Design Review	
	2016-11-22	Attitude Determination and Control System	
	Phase B		

5 PHOTODIODES

In this chapter, the algorithm for determining the Sun direction given the photodiodes measurements is presented. Software for testing the photodiodes' visibility for given configuration and the results for the simplest configuration are discussed. Final configuration has not been determined yet and number of concepts have to be optimized. Spectral sensitivity and Earth's albedo are investigated. Test stand and configuration of photodiodes for testing are presented.

5.1 ALGORITHM

Single photodiode provides one dimensional information about the Sun direction, i.e. it senses the angle between the photodiode's normal and the direction to the source of light. The concept is presented in the figure below.

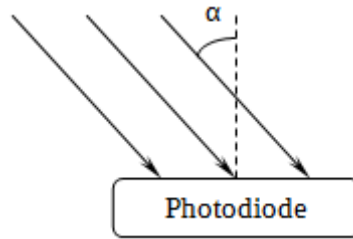


Figure 5-1 Illuminated photodiode

The current sensed in photodiode is dependent on intensity of the source of light and its direction. This can be written as:

$$I = I_{\max} \cos(\alpha) \quad (5.1)$$

where:



I_{\max} current sensed when the direction of light is collinear with the photodiode's normal [A]

α angle between photodiode's normal and source of light direction [deg].

If several photodiodes are placed at angles on satellite's faces, the Sun direction can be calculated using vector/matrix approach.

Let \mathbf{s} be the Sun unit vector which points towards the Sun and its origin coincides with the satellite's body frame origin. Also, let \mathbf{n}_1 be the unit vector collinear with the photodiode's normal which points outwards its surface. For single photodiode providing that it is illuminated by the Sun we can write:

$$\mathbf{n}_1 \circ \mathbf{s} = \cos(\alpha) \quad (5.2)$$

	PW-Sat2	Preliminary Design Review	
	2016-11-22	Attitude Determination and Control System	
	Phase B		

where \circ stands for dot product.

Taking into account 3 illuminated photodiodes which configuration is known, we can write:

$$\begin{aligned}
\mathbf{n}_1^T \mathbf{s} &= \cos(\alpha) \\
\mathbf{n}_2^T \mathbf{s} &= \cos(\beta) \\
\mathbf{n}_3^T \mathbf{s} &= \cos(\gamma)
\end{aligned} \tag{5.3}$$

where dot product is written as inner product. Substituting Eq. 5.1 into Eq. 5.3:

$$\begin{bmatrix} \mathbf{n}_1^T \\ \mathbf{n}_2^T \\ \mathbf{n}_3^T \end{bmatrix} \mathbf{s} = \frac{1}{I_{\max}} \begin{bmatrix} I_1 \\ I_2 \\ I_3 \end{bmatrix} \tag{5.4}$$

Inverting 3x3 matrix representing configuration of 3 illuminated photodiodes:

$$\mathbf{s} = \frac{1}{I_{\max}} \begin{bmatrix} \mathbf{n}_1^T \\ \mathbf{n}_2^T \\ \mathbf{n}_3^T \end{bmatrix}^{-1} \begin{bmatrix} I_1 \\ I_2 \\ I_3 \end{bmatrix} \tag{5.5}$$

In general, value of I_{\max} depends on intensity of source of light which is not known precisely. However, it can be seen that I_{\max} is vector \mathbf{s}' norm, therefore, we can normalize vector \mathbf{s}' to unity, obtaining unit Sun vector \mathbf{s} :



$$\mathbf{s}' = \begin{bmatrix} \mathbf{n}_1^T \\ \mathbf{n}_2^T \\ \mathbf{n}_3^T \end{bmatrix}^{-1} \begin{bmatrix} I_1 \\ I_2 \\ I_3 \end{bmatrix} \tag{5.6}$$

$$\mathbf{s} = \frac{\mathbf{s}'}{\|\mathbf{s}'\|} \tag{5.7}$$

The I_{\max} can be treated as a scaling factor thus it doesn't provide information about the direction of Sun vector \mathbf{s} . When the orientation of each photodiode in satellite's body frame is known, we can calculate the Sun vector in the satellite's body frame. This information is required in TRIAD algorithm and EKF outside eclipse.

In this derivation, it was assumed that I_{\max} is the same for all 3 photodiodes. In general, this is not true. Sun is not the only source of light on orbit, nevertheless it is the dominant one. Discussion on Earth reflectivity called *albedo* is presented in chapter 5.3. Other sources of light, like Moon and stars are negligible.

In order to determine which photodiodes are illuminated by the Sun, it is common to look for 3 greatest measurements. When configuration of the photodiodes provides full coverage of the attitude sphere, i.e. for arbitrary Sun direction at least 3 photodiodes are illuminated at a given time, this method is sufficient. However, if configuration doesn't provide full coverage, then a threshold has to be defined in order to determine if the photodiode is illuminated by the Sun or not. In general, induced voltage in photodiode not illuminated by the Sun will not be zero, due to weaker illumination by the Earth, Moon or stars.

	PW-Sat2	Preliminary Design Review	
	2016-11-22	Attitude Determination and Control System	
	Phase B		

5.2 VISIBILITY & CONFIGURATION

Software for testing the visibility of given photodiodes configuration was developed. As can be seen in chapter 5.1, at least 3 photodiodes have to be illuminated at a given time to calculate Sun vector. Field of view for each photodiode and photodiodes' normals are the inputs in visibility testing software. The output is the figure presenting the number of photodiodes illuminated for a given Sun direction and the attitude sphere percentage of coverage. Attitude sphere is an unit sphere and represents all possible unit Sun vector directions. The Sun direction is determined by 2 angles with step of 1° . Elevation angle is in the range of -90° to $+90^\circ$ and azimuth angle is in the range of 0° to 360° .

The figure of sensors visibility for simplest configuration of photodiodes is presented below. It was generated for six photodiodes, one on each satellite's face. Each photodiode's normal is collinear with the satellite's body frame axes. Field of view is 120° for each photodiode [5]. Thus, i -th photodiode is illuminated if $\mathbf{n}_i \cdot \mathbf{s} \geq \cos(60^\circ)$. Deployed solar panels were not considered.

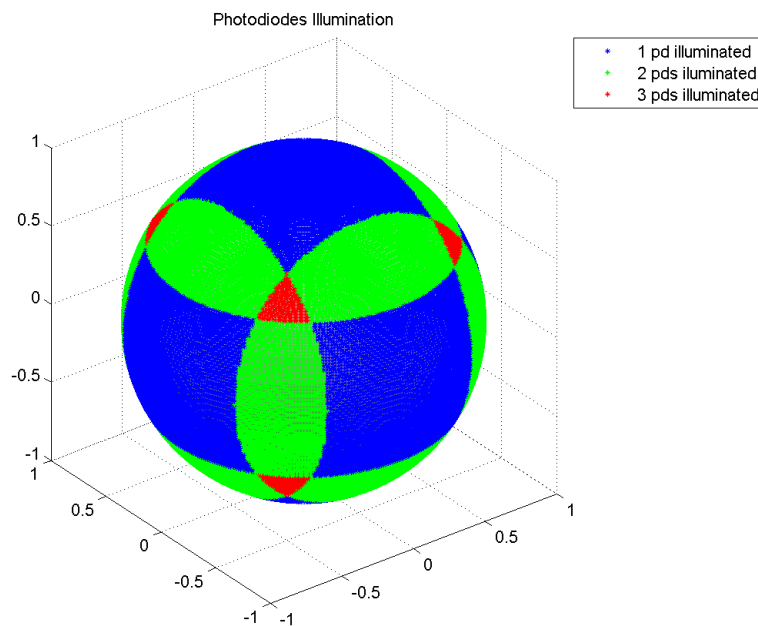




Figure 5-2 Visibility of configuration of 6 photodiodes

As expected, the simplest configuration with 6 photodiodes doesn't give good results. Only 2.16 % of the attitude sphere is covered.

The photodiodes' configuration on PW-Sat2 has to include several factors:



- No photodiode can be placed on $+Z$ and $-Z$ satellite's faces due to the communication hardware and sail deployment electronics which could be affected by the photodiodes' wires. Only 4 faces are available.

	PW-Sat2	Preliminary Design Review	
	2016-11-22	Attitude Determination and Control System	
	Phase B		

- Cut out in the deployable solar panels is necessary, so that photodiodes are not 'hidden' when solar panels are stowed. Also, configuration resulting in photodiode's shadowing by deployed solar panels has to be avoided.

With 4 faces available it is possible to obtain 94% coverage of the attitude sphere with 16 photodiodes, 4 on each face. However, optimization has not been done due to the uncertainty of fine Sun Sensor availability which would affect the photodiodes' configuration. Also, final configuration is strongly dependent on the field of view of each photodiode. Exact value of field of view will be known after the hardware tests.

It should be noted, that when Extended Kalman Filter is used for estimating the Sun vector based on photodiodes' measurements, not all 3 measurements are necessary. The filter can still estimate the Sun direction with only 1 or 2 measurements available, however the error grows with time.

	PW-Sat2	Preliminary Design Review	
	2016-11-22	Attitude Determination and Control System	
	Phase B		

5.3 SPECTRAL SENSITIVITY & ALBEDO

As mentioned in chapter 5.1, Sun is not the only source of light on orbit. Some of the sun light is reflected from the Earth's surface and atmosphere and affect the photodiode's induced current in the same way as direct sun light does. Thus it is necessary to discuss the corrupting effect of Earth albedo.

Reflected irradiance can be calculated by dividing the Earth's surface on cells obtaining the grid [3]. For each grid's cell the reflectivity can be calculated based on the averaged data obtained by Total Ozone Mapping Spectrometer (TOMS) data measured by the satellites. This is dependent on time and cloud coverage. However, using daily and annually averaged data gives comparable results [3]. Reflected irradiance also depends on the angles between the Sun vector and the grid's cell normal and the angle between the photodiode's normal and the grid's cell-to-satellite direction. Utilizing this model is not considered onboard the satellite due to high computational load.

Based on [14] the average Earth's albedo is 0.3 with peak of 0.4 for wavelengths in the range of (900, 1000) nm. On the other hand, solar radiation spectrum has its peak in the visible spectrum, around 500 nm and slowly decreases towards the infrared spectrum. The solar radiation spectrum is presented in the figure below.

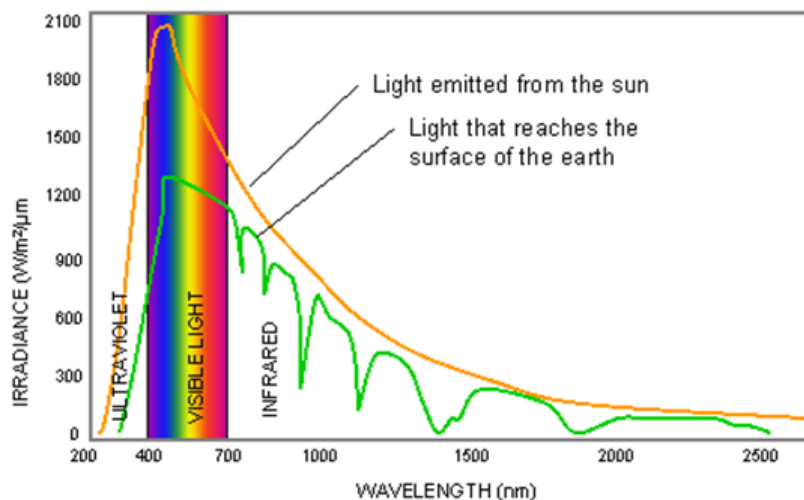




Figure 5-3 Solar radiation spectrum on Earth's surface and above the atmosphere

The Earth's albedo effect can be minimized by choosing the photodiodes with spectral sensitivity peak in the range of (500, 600) nm and lower sensitivity in infrared. The figure below presents spectral sensitivity for OSRAM SFH2430 photodiode [5].

	PW-Sat2	Preliminary Design Review	
	2016-11-22	Attitude Determination and Control System	
	Phase B		

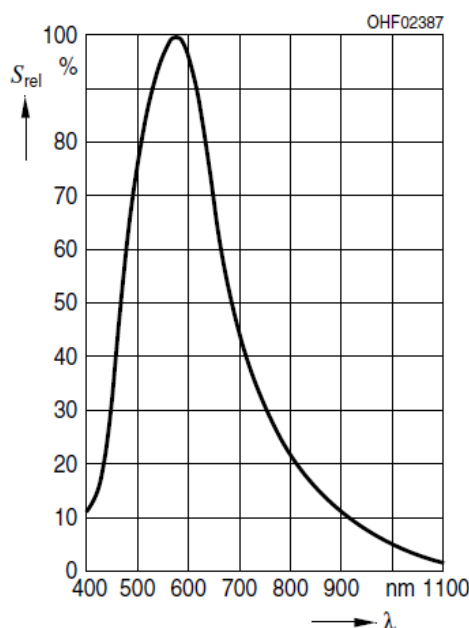




Figure 5-4 Spectral sensitivity of OSRAM SFH2430 photodiode

Spectral sensitivity of OSRAM SFH2430 has an evident peak around 570 nm. Based on [14] Earth's albedo in the range of (500, 600) nm is around 0.1 giving 10% relative error in photodiodes measurements due to the Earth's albedo. Although the Earth's albedo has its peak in infrared spectrum, the effect is weaker due to the photodiode's sensitivity.

5.4 TESTING

In order to evaluate the accuracy of OSRAM SFH2430 photodiodes, the team has to perform tests. The lamp with radiation spectrum close to the solar spectrum will be used as a Sun simulator. Test Stand allowing control of angles about 2 perpendicular axes will be utilized. Further details of lamp's and Test Stand's hardware and construction details can be found in [15] and [16].

The platform with controllable pitch and roll angles is presented in the figure below. Three photodiodes with predetermined configuration will be mounted on the platform. Sun direction will be constant in reference frame. By rotating the platform, components of the Sun vector in platform frame will be changed. Using the algorithm presented in chapter 5.1, calculated Sun vector components will be compared with the true values assuming that true platform orientation and true Sun direction are known. Noise and overall accuracy will be determined.

	PW-Sat2	Preliminary Design Review	
	2016-11-22	Attitude Determination and Control System	
	Phase B		

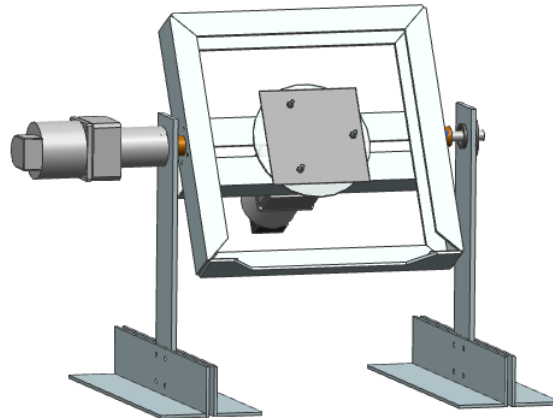


Figure 5-5 Test Stand for Sun Sensor and photodiodes testing



The figure below presents the CAD model of photodiode's board assembly for testing. Looking from above, the photodiodes are placed at the 120° from each other. The angle between each photodiode normal and the board's surface is 70° . In this configuration 3 photodiodes will be illuminated for platform pitch angles in the range of -40° to $+40^\circ$, assuming field of view of 120° for each photodiode. Platform roll angle is fully covered, i.e. between 0° and 360° .



Figure 5-6 Configuration of 3 photodiodes for testing

Each photodiode has its temperature sensor for temperature sensitivity compensation. Wholes on faces are due to accelerate heat exchange.

The effect of albedo can be simulated by placing another lamp with the spectral radiation peak in infrared spectrum next to the Sun simulating lamp. The photodiode's albedo sensitivity and error in Sun vector components can be evaluated.



	PW-Sat2	Preliminary Design Review	
	2016-11-22	Attitude Determination and Control System	
	Phase B		

6 ADCS ARCHITECTURE

In the introduction it was stated, that the control strategy has changed during Phase B. With 3 magnetorquers, the team has not developed the algorithm to maintain constant satellite's attitude in ECI inertial frame with the presence of the gravity gradient torque. Since nadir pointing is not considered after the mission plan review, the major task of the ADCS is Sun tracking. The team has decided to utilize the gyroscopic effect and stabilize the axis of rotation in ECI inertial frame. With this approach, pointing solar panels towards the Sun can be made possible, assuming that Sun vector is collinear with the satellite's +X axis perpendicular to deployed solar panels' plane. Further details on the Sun Pointing controller are presented in chapter 7.4.3.

With these requirements, ADCS is necessary to detumble the satellite after launch and then stabilize the magnitude and direction of angular rotation around satellite's +X axis.

In the figure below, the ADCS block diagram is presented. It is related to Sun Pointing mode, when the attitude determination and estimation algorithms are utilized. Thus information from Sun Sensor, magnetometer and gyroscope is necessary. In Detumbling mode, with B-Dot algorithm, only magnetometer data is used and no attitude determination and estimation is performed, making the ADCS calculations more simple.

	PW-Sat2	Preliminary Design Review	
	2016-11-22	Attitude Determination and Control System	
	Phase B		

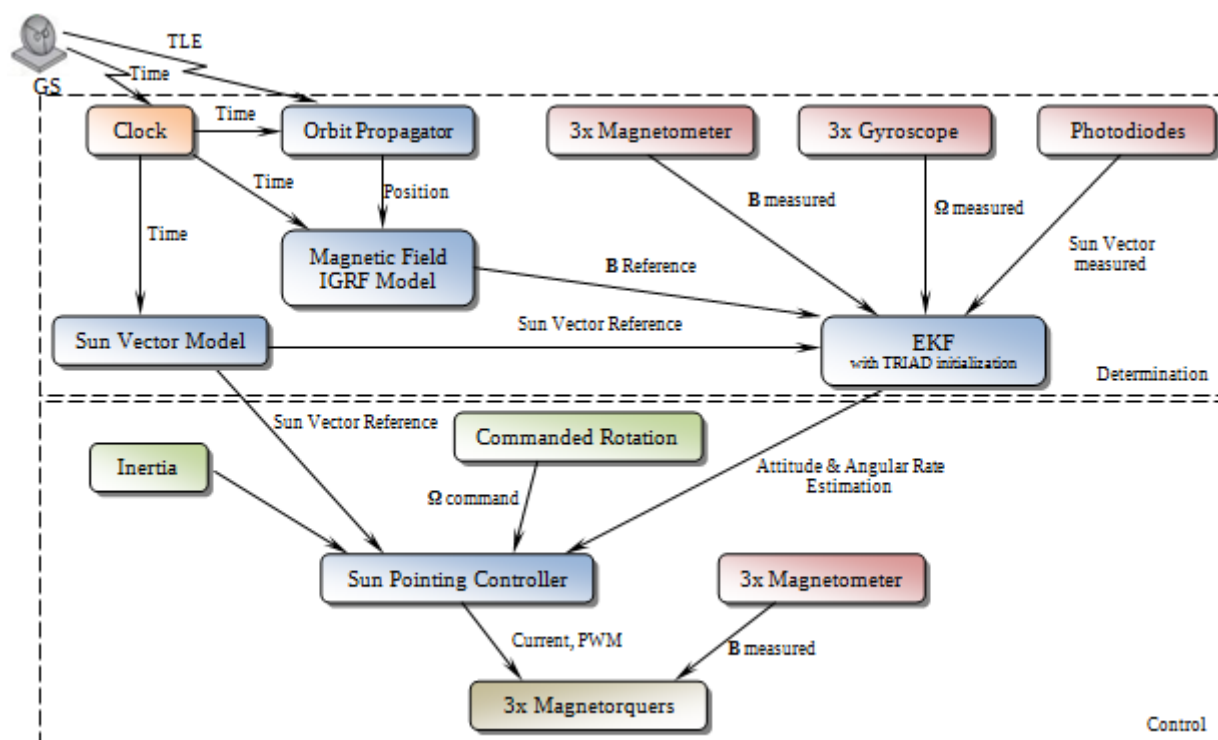


Figure 6-1 ADCS Block Diagram for Sun Pointing Mode



In following subsections, an overview of attitude and angular rate determination and control strategy is presented. Required algorithms and environmental models are described briefly. Detailed discussion on attitude and angular rate determination and estimation, as well as control algorithms is presented in chapters 7.3 and 7.4, respectively.

6.1 DETERMINATION

Attitude and angular rate determination and estimation algorithms are necessary only in Sun Pointing mode. Brief description of each algorithm and environmental models are presented below.

SGP4 Orbit Propagator

Satellite position has to be known in order to determine reference Earth's magnetic field in current satellite's position. SGP4 stands for Simplified General Perturbations and is based on Two Lines Elements (TLE). The algorithm is widely used to determine satellite's position and velocity, not only onboard CubeSats. Parameters necessary to obtain position and velocity vectors are updated by NORAD (North American Aerospace Defense) after several hours. The algorithm includes perturbation models accounting for Earth oblateness and atmospheric drag. The accuracy of the calculated position is estimated to be ~1km at the epoch and grows to ~3km after a day [17]. The error in position of ~10km would not affect the attitude estimation significantly. Therefore, update of TLE data should be sent by uplink not less often than after each 3 days.

	PW-Sat2	Preliminary Design Review	
	2016-11-22	Attitude Determination and Control System	
	Phase B		

IGRF Magnetic Field Model

Earth's magnetic field in current satellite's position has to be known in order to determine the satellite's attitude. Reference value in ECI inertial frame is then compared with measured data obtained from 3 axis magnetometer (for details see chapter 7.3.3). IGRF stands for International Geomagnetic Reference Field and the model's parameters are released by International Association of Geomagnetism and Aeronomy (IAGA). The algorithm is widely used in satellite's attitude determination algorithms, not only onboard CubeSats. Measurements are gathered by the satellite missions and spherical harmonic expansion is used to calculate magnetic field vector in given position. Parameters are updated every 5 years. New set of data will be released in 2015. In simulations IGRF11 released in 2010 is used. The accuracy of the reference model is estimated to be at the level of 20nT [18]. The algorithm, associated equations and list of parameters in spherical harmonic expansion can be found in [18].

Sun Position

Sun Position in ECI inertial frame has to be known in order to point the solar panels in the desired direction. This information is also required in comparing the Sun Sensor data with the reference in EKF and TRIAD algorithms. Only direction of the Sun vector is required, thus the distance to the Sun doesn't provide any useful information. Therefore, using the algorithm presented below, one calculates unit vector from the origin of ECI inertial frame to the Sun. Unit vector is expressed in ECI inertial frame. The derivation follows [1].

The mean longitude and mean anomaly of the Sun are calculated, respectively:

$$\phi_{\odot} = 280.46^{\circ} + 36000.771T_{UT1} \quad (6.1a)$$

$$M_{\odot} = 357.5277233^{\circ} + 35999.05034T_{UT1} \quad (6.1b)$$

where

$$T_{UT1} = \frac{JD(Y,M,D,h,m,s) - 2451545}{36525} \quad (6.2)$$



$$JD(Y, M, D, h, m, s) = 1721013.5 + 367Y - \text{INT}\left\{\frac{7}{4}\left[Y + \text{INT}\left(\frac{M+9}{12}\right)\right]\right\} + \text{INT}\left(\frac{275M}{9}\right) + D + \frac{60h+m+s/60}{1440} \quad (6.3)$$

where JD stands for Julian Date and Y, M, D, h, m, s stands for year, month, day, hour, minutes and seconds in GMT, respectively. INT denotes integer part (floor).

Both ϕ_{\odot} and M_{\odot} are reduced to the range 0° to 360° and the longitude of ecliptic is calculated in degrees:

$$\phi_{\text{ecliptic}} = \phi_{\odot} + 1.914666471^{\circ}\sin(M_{\odot}) + 0.019994643^{\circ}\sin(2M_{\odot}) \quad (6.4)$$

The obliquity of ecliptic can be determined as:

	PW-Sat2	Preliminary Design Review	
	2016-11-22	Attitude Determination and Control System	
	Phase B		

$$\varepsilon = 23.439291^\circ - 0.0130042^\circ T_{UT1} \quad (6.5)$$

Finally, the unit vector from the Earth's center to the Sun expressed in ECI inertial frame is:

$$\mathbf{e}_{\oplus\odot} = \begin{bmatrix} \cos(\phi_{\text{ecliptic}}) \\ \cos(\varepsilon)\sin(\phi_{\text{ecliptic}}) \\ \sin(\varepsilon)\sin(\phi_{\text{ecliptic}}) \end{bmatrix} \quad (6.6)$$

In accurate computations, the unit vector from the satellite's current position to the Sun is necessary. However, the error is negligible due to the large distance from Earth to the Sun. Figure below presents the concept.

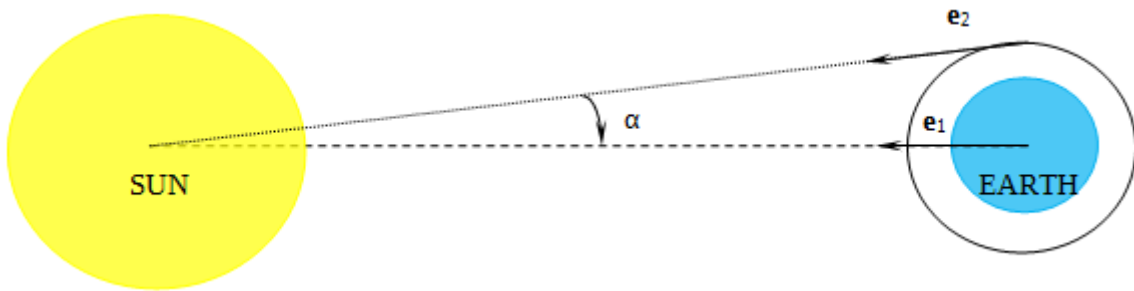


Figure 6-2 Error between Earth to Sun and Satellite to Sun vectors

Angle α corresponds to the maximum direction error between vectors \mathbf{e}_1 and \mathbf{e}_2 . Assuming spherical Earth with radius equal to 6371km, orbit of altitude 600 km and distance between Earth's and Sun's centers $1.5 \cdot 10^8$ km:

$$\alpha = \text{atan}\left(\frac{6371+600}{1.5 \cdot 10^8}\right) = 0.0027^\circ \quad (6.7)$$



This error can be neglected, thus assumption that Sun direction doesn't change along the orbit is sufficient.

TRIAD

Attitude of the object relative to some reference frame can be obtained by taking at least two measurements of unit vectors in body frame. One vector is not sufficient, because it provides information about 2 angles, however to calculate the attitude, 3 parameters are required. If components of measured unit vectors are known in the reference frame, then the attitude of the object can be calculated. The simplest algorithm is TRIAD (TRIAxial Attitude Determination). The general form of the algorithm include weights of the measured vectors, putting more "trust" in more accurate measurement. Using Sun Sensor and magnetometer, TRIAD can be used only outside eclipse. EKF is initialized with information from TRIAD, which in general is less accurate than filtered data.

Extended Kalman Filter

The attitude determination problem is nonlinear, therefore Extended Kalman Filter has to be used. EKF provides estimate of the noisy data and its output is more accurate than obtained from deterministic, static attitude

	PW-Sat2	Preliminary Design Review	
	2016-11-22	Attitude Determination and Control System	
	Phase B		

determination methods, for example TRIAD. Moreover, EKF provides information about the attitude in eclipse, when the Sun Sensor measurement is not available. Nevertheless, it has to be initialized with at least two observations outside eclipse.

6.2 CONTROL

In this chapter brief description of Sun Pointing and B-dot algorithm is presented. Further details can be found in chapter 7.4.

Sun Pointing

Sun Pointing mode requires spinning the satellite about satellite's +X axis and pointing it towards the Sun. Spin stabilization keeps the Sun tracking error in predetermined limits. The control law is based on the desired angular momentum, precession and nutation error. The control law requires therefore information about inertia matrix, current angular rate and attitude of the satellite with reference to ECI inertial frame.

B-Dot

B-Dot algorithm is the simplest one for detumbling. It is widely used to decelerate angular rotation after P-POD deployment. It needs information of Earth's magnetic field changes in satellite's frame. Therefore, two subsequent magnetometer measurements are required. The basic assumption is that the changes of magnetic field measurements in body frame are due to the satellite's rotational movement. Stability of the B-Dot control law is proven with Lyapunov's second method for stability. High-pass filter is utilized in order to filter data when calculating the discrete derivative based on noisy data. Built-in autonomous detumbling mode on iMTQ board activates when the predetermined threshold of the angular rate is exceeded.

6.3 ADCS MODES



As mentioned in chapter 2, the number of ADCS modes were minimized after mission plan review. Also, the simplicity of the ADCS is one of the dominant requirements, thus making the transitions between modes less complex had to be considered. In this chapter, 4 ADCS modes are presented.

- SAFE/OFF

In this mode, the ADCS is not working. Sensors' and actuators' power supply is cut off. ADCS will be in SAFE/OFF mode in initial phase of the mission. Also, transition to this mode has to be done autonomously when battery level drops below some predetermined threshold or after sending telecommand when data obtained from telemetry will denote the ADCS malfunction.

- DETUMBLING

This mode activates after first turn on of the power supply in the initial phase of the mission. Autonomous transition to this mode has to be done after exceeding predetermined threshold of the angular rate. DETUMBLING mode requires magnetometer and at least two actuators working properly.

	PW-Sat2	Preliminary Design Review	
	2016-11-22	Attitude Determination and Control System	
	Phase B		

- **STANDBY**

In this mode, the attitude is estimated based on sensors' data, but no attitude control is performed. Transition to this mode is possible after DETUMBLING mode or actuators' malfunction. Then, estimating the attitude is necessary to compare the data with experimental Sun Sensor's data and to check the overall performance of the attitude determination and estimation algorithms.

- **SUN POINTING**

This mode is activated after detumbling in initial phase of the mission, providing that solar panels are deployed. Transition to this mode is possible from STANDBY mode, after assuring EKF convergence, because controlling the attitude based on not filtered sensors data consumes much more energy. SUN POINTING mode requires all sensors and at least two actuators working properly.

In the table below, the timeline of the ADCS is presented. Nominal ADCS mode is Sun Pointing with rotation 5°/s about the satellite's X axis.





	PW-Sat2	Preliminary Design Review	
	2016-11-22	Attitude Determination and Control System	
	Phase B		

Table 6-1 ADCS on-orbit sequence

Nr	Event
1.	PW-Sat2 is deployed from P-POD, power is on, start ADCS system
2.	Start Detumbling mode
3.	When satellite's angular rate reached predetermined threshold, finish Detumbling
4.	Receive TLE orbital and time data from ground
5.	Start Standby mode
6.	When deployment of solar panels confirmed, start nominal Sun Pointing mode

	PW-Sat2	Preliminary Design Review	
	2016-11-22	Attitude Determination and Control System	
	Phase B		

7 DESIGN ANALYSIS

In this chapter detailed discussion of determination and control algorithm is presented. Algorithms for multiplicative EKF (MEKF) and solution of Wahba's Problem based on two observations are presented. Satellite's dynamics and kinematics equations are derived using the quaternion notation. Mathematical models of the disturbance torques are presented.

7.1 DISTURBANCE TORQUES

During the design of the ADCS, torques tending to destabilize the attitude of the satellite have to be investigated. In this subchapter, mathematical models of four dominant disturbance torques are presented: gravity gradient, aerodynamic, solar pressure and magnetic torques. The comparison of the magnitude of these disturbance torques is presented. Mathematical models presented are simple and appropriate for CubeSat ADCS design analysis. The most important issue is evaluating the magnitude and the nature of disturbance torques.

7.1.1 GRAVITY GRADIENT

Gravity acceleration around the Earth is not uniformly distributed. The magnitude of gravity may vary within the satellite's volume, generating the torque. Although on Earth this effect is negligible, on orbit, when stringent requirements for attitude have to be met, gravity gradient has to be modeled. Equations follow the derivation in [2].

Assuming that satellite's body frame is a principal axis frame, we can write:

$${}^sG_x = \frac{3\mu}{r^3} (I_{zz} - I_{yy}) {}^s\mathbf{A}(2,3) {}^s\mathbf{A}(3,3) \quad (7.1a)$$

$${}^sG_y = \frac{3\mu}{r^3} (I_{xx} - I_{zz}) {}^s\mathbf{A}(1,3) {}^s\mathbf{A}(3,3) \quad (7.1b)$$

$${}^sG_z = \frac{3\mu}{r^3} (I_{yy} - I_{xx}) {}^s\mathbf{A}(1,3) {}^s\mathbf{A}(2,3) \quad (7.1c)$$

where



r norm of the satellite's position vector in ECI inertial frame

${}^s\mathbf{A}$ transformation matrix from orbital frame to satellite's body frame

μ Earth's constant, $\mu = GM_\oplus$ where G is gravity constant and M_\oplus is Earth's mass

I_{xx} moment of inertia around X axis of satellite's frame, analogous I_{yy} and I_{zz}

When the principal axis frame slightly deviates from the satellite's body frame above approximation is correct. On the basis of PW-Sat2 CAD model which is almost a final version, principal axis frame deviates of -0.36° , -0.14° and -3.54° from satellite's X, Y and Z axes, respectively. Therefore, above equations can be used.

	PW-Sat2	Preliminary Design Review	
	2016-11-22	Attitude Determination and Control System	
	Phase B		

Transformation matrix ${}^s\mathbf{A}_o$ can be written as:

$${}^s\mathbf{A}_o = {}^s\mathbf{A}_i \cdot {}^i\mathbf{A}_o \quad (7.2)$$

Transformation matrix ${}^s\mathbf{A}_i$ can be obtained when the attitude of the satellite is known. Transformation matrix ${}^i\mathbf{A}_o$ can be calculated when the satellite's position and velocity vectors expressed in ECI inertial frame are known:

$${}^i\mathbf{A}_o = [{}^l\mathbf{o}_x \quad {}^l\mathbf{o}_y \quad {}^l\mathbf{o}_z] \quad (7.3)$$

where ${}^l\mathbf{o}_x$ is the unit vector defining the X axis of orbital frame expressed in ECI inertial frame, analogous ${}^l\mathbf{o}_y$ and ${}^l\mathbf{o}_z$. Unit vectors forming orbital frame can be calculated as:

$${}^l\mathbf{o}_z = -{}^l\mathbf{r}/\|{}^l\mathbf{r}\| \quad (7.4a)$$

$${}^l\mathbf{o}_y = -({}^l\mathbf{r} \times {}^l\mathbf{v})/\|{}^l\mathbf{r} \times {}^l\mathbf{v}\| \quad (7.4b)$$

$${}^l\mathbf{o}_x = {}^l\mathbf{o}_y \times {}^l\mathbf{o}_z \quad (7.4c)$$

For 2-unit CubeSat on orbit with altitude 600 km, gravity gradient torque norm is around 10^{-8} Nm.

7.1.2 AERODYNAMIC TORQUE

When calculating aerodynamic torque, commonly used approach is to divide the satellite into collection of N flat plates with area S_i and outward normal unit vector ${}^s\mathbf{n}_i$ expressed in satellite's body frame each [1]. In order to avoid self-shielding on concave satellite, PW-Sat2 with deployed solar panels is modeled as a prism with trapezoid cross-section.

In order to calculate aerodynamic force acting on a i-th plate, one have to determine atmospheric density and satellite's velocity relative to the atmosphere. Relative velocity can be easily obtained with assumption that the atmosphere co-rotates with Earth. Therefore, relative velocity vector expressed in ECI inertial frame will be:

$${}^l\mathbf{v}_{rel} = {}^l\mathbf{v} - [{}^l\mathbf{\Omega}_\oplus \times] {}^l\mathbf{r} \quad (7.5)$$

where ${}^l\mathbf{v}$ and ${}^l\mathbf{r}$ are satellite's velocity and position vectors expressed in ECI inertial frame, ${}^l\mathbf{\Omega}_\oplus$ is the Earth's angular rate vector expressed in ECI inertial frame thus ${}^l\mathbf{\Omega}_\oplus = [0 \quad 0 \quad \Omega_\oplus]^T$ for $\Omega_\oplus = 7.2921158553 \times 10^{-5}$ rad/s.

When calculating atmospheric density, the simplest approach is to use static, exponentially decaying atmosphere model, given by the equation [1]:

$$\rho = \rho_0 \exp\left(-\frac{h-h_0}{H}\right)$$

where h is the height of the satellite above the Earth's surface. Reference parameters h_0 , H_0 and ρ_0 can be read from the table below [1]:



	PW-Sat2	Preliminary Design Review	
	2016-11-22	Attitude Determination and Control System	
	Phase B		

Table 7-1 Static, exponentially decaying atmosphere model's parameters

h (km)	h₀ (km)	ρ₀ (kg/m³)	H (km)
450-500	450	1.585*10 ⁻¹²	62.2
500-600	500	6.967*10 ⁻¹³	65.8
600-700	600	1.454*10 ⁻¹³	79
700-800	700	3.614*10 ⁻¹⁴	109

Only altitudes from 450 to 800 km are presented, because only within this range the team looks for possible orbits.

Aerodynamic force expressed in satellite's body frame, acting on i-th plate can be calculated:

$${}^S\mathbf{F}_{\text{aero},i} = -\frac{1}{2}\rho C_D \|\mathbf{v}_{\text{rel}}\| {}^S\mathbf{v}_{\text{rel}} S_i \max(\cos\theta_{\text{aero},i}, 0) \quad (7.6a)$$



$$\cos\theta_{\text{aero},i} = {}^S\mathbf{n}_i \cdot {}^S\mathbf{v}_{\text{rel}} / \|\mathbf{v}_{\text{rel}}\| \quad (7.6b)$$

where C_D is dimensionless drag coefficient, for 2U CubeSats equal approximately 2.2. Finally, the aerodynamic torque can be obtained as:

$${}^S\mathbf{T}_{\text{aero}} = \sum_{i=1}^N {}^S\mathbf{r}_i \times {}^S\mathbf{F}_{\text{aero},i} \quad (7.7a)$$

where ${}^S\mathbf{r}_i$ is the vector from the satellite's center of mass to the center of pressure of the i-th plate. In simulations, center of pressure of each plate is assumed to be in its geometrical center.

For 2-unit CubeSat on orbit with altitude 600 km, aerodynamic torque norm is around 10⁻⁸ Nm.

	PW-Sat2	Preliminary Design Review	
	2016-11-22	Attitude Determination and Control System	
	Phase B		

7.1.3 SOLAR RADIATION PRESSURE TORQUE

Approach for calculating solar radiation pressure torque is similar to calculating aerodynamic torque. It is based on the division of the satellite into collection of N flat plates with area S_i and outward normal unit vector ${}^S\mathbf{n}_i$ expressed in satellite's body frame each.

One have to calculate the unit vector from the satellite's frame origin to the Sun. However, on the basis of the discussion in chapter 6.1, we can use the unit vector from Earth's center to the Sun and the resulting error is negligible.

In order to determine the solar radiation torque acting on the satellite, we have to calculate the solar radiation pressure at the position of the spacecraft:

$$P_{\odot} = \frac{\mathcal{F}_{\odot}}{c}$$

where $c = 299792458$ m/s is the speed of light and $\mathcal{F}_{\odot} = 1363$ W/m² is the solar constant at a distance of 1 AU from the Sun. The solar constant value changes during 11-year solar cycle activity. Rapid fluctuations as large as 5 W/m² can be accommodated in detailed analysis.

The solar radiation force expressed in satellite's body frame, acting on i -th plate is [1]:

$${}^S\mathbf{F}_{\text{SRP},i} = -P_{\odot}S_i \left[2 \left(\frac{R_{\text{diff},i}}{3} + R_{\text{spec},i} \cos\theta_{\text{SRP},i} \right) {}^S\mathbf{n}_i + (1 - R_{\text{spec},i}) {}^S\mathbf{e}_{\oplus\odot} \right] \max(\cos\theta_{\text{SRP},i}, 0)$$

$$\cos\theta_{\text{SRP},i} = {}^S\mathbf{n}_i \cdot {}^S\mathbf{e}_{\oplus\odot} \quad (7.8)$$

where ${}^S\mathbf{e}_{\oplus\odot}$ can be calculated transforming vector calculated in Eq. 6.6 to the satellite's body frame assuming the attitude of the satellite is known.

$R_{\text{diff},i}$, $R_{\text{spec},i}$ and $R_{\text{abs},i}$ denote diffuse reflection, specular reflection and absorption coefficients, respectively. The coefficients sum to unity, $R_{\text{diff},i} + R_{\text{spec},i} + R_{\text{abs},i} = 1$, thus $R_{\text{abs},i}$ does not appear explicitly in Eq. 7.8. For PW-Sat2 simulations, values of coefficients for MLI, aluminium and solar arrays have been obtained from [19, 20]. Approximate values for each face have been calculated using contribution proportional to the area which certain material covers on each face.



The solar radiation pressure torque can be calculated in the same way as aerodynamic torque, utilizing Eq. 7.7a:

$${}^S\mathbf{T}_{\text{SRP}} = \sum_{i=1}^N {}^S\mathbf{r}_i \times {}^S\mathbf{F}_{\text{SRP},i} \quad (7.7b)$$

where ${}^S\mathbf{r}_i$ is the vector from the satellite's center of mass to the center of pressure of the i -th plate. In the simulations, center of pressure of each plate is assumed to be in its geometrical center.

For 2-unit CubeSat on orbit with altitude 600 km, solar radiation pressure torque norm is around $0.5 \cdot 10^{-8}$ Nm.

7.1.4 MAGNETIC TORQUE

	PW-Sat2	Preliminary Design Review	
	2016-11-22	Attitude Determination and Control System	
	Phase B		

On-board electronics generate magnetic dipole which acts in the same way as electromagnetic coils for attitude control does. Torque is generated for magnetic dipole \mathbf{m}_{mag} in a magnetic field \mathbf{B} :

$${}^S\mathbf{T}_{\text{mag}} = {}^S\mathbf{m}_{\text{mag}} \times {}^S\mathbf{B} \quad (7.9)$$

where all vectors are expressed in satellite's body frame.

The magnitude of magnetic disturbance torque decreases with altitude, because the intensity of Earth's magnetic field is weaker for higher altitudes.

Based on the discussion in [3], uncompensated satellite with the average power of 110 W generates approximately 1 Am² magnetic dipole. Assuming linear change, average power of PW-Sat2 will be 10 W at worst case corresponding to 0.1 Am² magnetic dipole. However, the team will try to avoid placing wires in loops during the configuration, thus it is guesstimated that value ten times smaller can be assumed during the simulations, i.e. 0.01 Am². Nature of magnetic moment generated by onboard electronics is not known, thus in the simulations the random number with uniform distribution in the range from -0.01 Am² to +0.01 Am² on each axis has been assumed.

For above assumptions, for 2-unit CubeSat on orbit with altitude 600 km, the magnetic disturbance torque norm is around $0.5 \cdot 10^{-6}$ Nm, thus it is the dominant one.

7.1.5 CONCLUSIONS

In this subchapter, comparison of disturbance torques is presented on the figure. It was generated for altitude between 450 km and 800 km, because only in this range the team looks for possible orbits. Mathematical models and assumptions are described in above subsections.

The orbit was chosen SSO dawn/dusk so that the satellite is constantly illuminated by the Sun, thus solar radiation torque never equals 0. Set of simulations were run for altitude step equal 10 km. Initial angular rates were set to 0 and initial attitude of satellite's body frame with reference to ECI inertial frame was set to 10°, 40°, -25° Euler angles yaw, pitch and roll respectively. No control torque was applied. The vector norm of each disturbance torque was averaged along the orbit. The results are presented in the figure below.

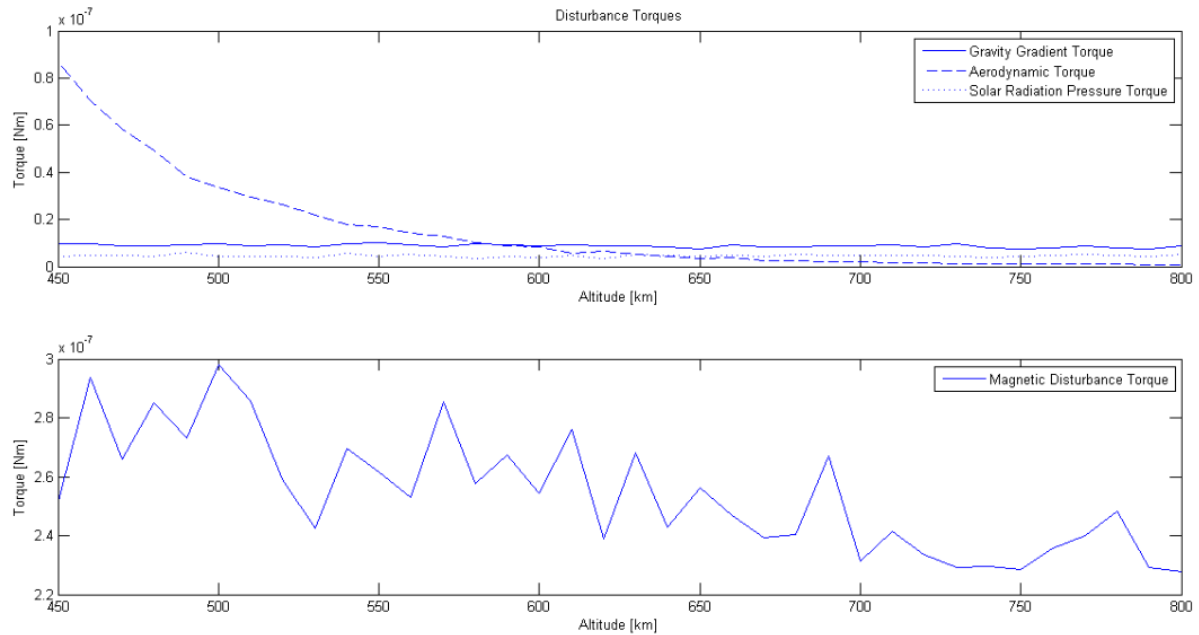




Figure 7-1 Disturbance torques dependency on orbit's altitude

It can be seen that the magnetic disturbance torque is the dominant one and the aerodynamic torque quite rapidly decreases with altitude. Magnetic disturbance torque also decreases with altitude due to the weaker Earth's magnetic field. The randomness of the magnetic disturbance torque can be explained, taking into account that magnetic dipole is generated as a uniformly distributed random number within predetermined range.

7.2 DYNAMICS & KINEMATICS

In this chapter attitude dynamics and kinematics equations are presented. Satellite's dynamics and kinematics can be modeled mathematically using the dynamic Euler equations for rigid body and derivative of the quaternion, respectively. Assumption of rigid body is sufficient for non-moving solar panels and non-vibrating deployed magnetometer if it is considered. The performance of ADCS after sail deployment is not considered. Thus the satellite can be modeled as a rigid body. In the following subsections general and linearized equations are derived. They are utilized in EKF formulation and in the simulations for integrating true angular acceleration twice in order to obtain true angular rate and attitude.

	PW-Sat2	Preliminary Design Review	
	2016-11-22	Attitude Determination and Control System	
	Phase B		

7.2.1 GENERAL FORMULATION

Dynamic attitude equations relate total torque applied to a satellite with the derivative of angular rate. In calculations, we are interested in derivative of angular rate vector expressed in satellite's body frame. In rotating frame, Newton's law of motion cannot be applied directly, therefore the general form of equation, relating the derivative of a vector \mathbf{x} in a fixed and a moving frame, is used:

$${}^m_f \underline{\mathbf{A}} \cdot {}^f \dot{\mathbf{x}} = {}^m \dot{\mathbf{x}} + {}^m \boldsymbol{\omega}_{m/f} \times {}^m \mathbf{x} \quad (7.10)$$

where subscripts m and f denote moving and fixed frame, respectively and ${}^m \boldsymbol{\omega}_{m/f}$ is the angular rate of the moving frame relative to the fixed frame expressed in the moving frame.

By substituting satellite's angular momentum vector for vector \mathbf{x} in Eq. 7.10 and using Newton's second law for rotational movement, one can obtain the dynamic Euler equation:

$${}^s \dot{\boldsymbol{\omega}}_{s/i} = \underline{\mathbf{I}}^{-1} \{ {}^s \mathbf{T}_{\text{dist}} + {}^s \mathbf{T}_{\text{ctrl}} - [{}^s \boldsymbol{\omega}_{s/i} \times] (\underline{\mathbf{I}} \cdot {}^s \boldsymbol{\omega}_{s/i}) \} \quad (7.11)$$

where skew-symmetric matrix multiplication is used instead of vector cross product. Inertia matrix is calculated in satellite's body frame which has its origin in the center of satellite's mass.

Kinematic attitude equations can be formulated using quaternion notation. In this document, the elements of a quaternion \mathbf{q} are:

$$\mathbf{q} = [\mathbf{q}_{1:3} \quad q_4]^T$$

where $\mathbf{q}_{1:3}$ and q_4 are quaternion's vector and scalar parts, respectively.

When current quaternion and angular rate are known, the derivative of the quaternion can be integrated, obtaining satellite's attitude in the next iteration. However, attention has to be paid to normalization of a quaternion. Runge-Kutta methods are based on an additive procedure, but when two quaternions are added, the norm constraint is violated. Therefore, after each Runge-Kutta iteration, quaternion has to be normalized.

On the basis of quaternion algebra, the derivative of a quaternion can be calculated as follows [2]:



$${}^s_i \dot{\mathbf{q}} = \frac{1}{2} {}^s \boldsymbol{\omega}_{s/i} \otimes {}^s_i \mathbf{q} \quad (7.12)$$

where \otimes denotes quaternion multiplication with the same order as attitude matrix multiplication.

Eq. 7.12 can be written in an explicit form:

$${}^s_i \dot{\mathbf{q}} = \frac{1}{2} [{}^s \boldsymbol{\omega}_{s/i} \otimes] {}^s_i \mathbf{q} \quad (7.13a)$$

where

	PW-Sat2	Preliminary Design Review	
	2016-11-22	Attitude Determination and Control System	
	Phase B		

$$[{}^s\omega_{s/i} \otimes] = \begin{bmatrix} -[{}^s\omega_{s/i} \times] & {}^s\omega_{s/i} \\ -{}^s\omega_{s/i}^T & 0 \end{bmatrix} \quad (7.13b)$$

7.2.2 LINEARIZED FORMULATION

In this subsection, the general attitude dynamics and kinematics equations are linearized. The linearized formulation is used in EKF derivation.

First, the dynamic equation is linearized using first order Taylor expansion. Eq. 7.11 is written below and subscripts and superscripts are removed for clarity. It is assumed that all vectors are expressed in satellite's body frame and angular rate vector represents angular rate of a satellite's body frame relative to ECI inertial frame.

$$\dot{\omega} = \mathbf{I}^{-1} \{ \mathbf{T}_{\text{dist}} + \mathbf{T}_{\text{ctrl}} - [\omega \times] (\mathbf{I} \cdot \omega) \} \quad (7.11)$$

Above equation is linearized around some nominal value $\bar{\omega}$ with small error $\tilde{\omega}$, so that:

$$\omega = \bar{\omega} + \tilde{\omega} \quad (7.14)$$

Eq. 7.11 is multivariable, therefore above notation is applied to \mathbf{T}_{dist} and \mathbf{T}_{ctrl} as well.

$$\begin{aligned} \dot{\omega} \approx & \mathbf{I}^{-1} \{ \bar{\mathbf{T}}_{\text{dist}} + \bar{\mathbf{T}}_{\text{ctrl}} - [\bar{\omega} \times] (\mathbf{I} \cdot \bar{\omega}) \} - \mathbf{I}^{-1} \left(\frac{d}{d\omega} \{ [\omega \times] (\mathbf{I} \cdot \omega) \} \right) \tilde{\omega} + \mathbf{I}^{-1} \left(\frac{d}{dT_{\text{dist}}} \mathbf{T}_{\text{dist}} \right) \cdot \tilde{\mathbf{T}}_{\text{dist}} \\ & + \mathbf{I}^{-1} \left(\frac{d}{dT_{\text{ctrl}}} \mathbf{T}_{\text{ctrl}} \right) \cdot \tilde{\mathbf{T}}_{\text{ctrl}} \end{aligned} \quad (7.15)$$

where the derivatives are calculated at nominal values. Therefore, Eq. 7.15 can be written:

$$\begin{aligned} \dot{\omega} \approx & \mathbf{I}^{-1} \{ \bar{\mathbf{T}}_{\text{dist}} + \bar{\mathbf{T}}_{\text{ctrl}} - [\bar{\omega} \times] (\mathbf{I} \cdot \bar{\omega}) \} - \mathbf{I}^{-1} \{ [\mathbf{1}_{3 \times 3} \times] (\mathbf{I} \cdot \bar{\omega}) + [\bar{\omega} \times] \mathbf{I} \} \tilde{\omega} + \mathbf{I}^{-1} \cdot (\tilde{\mathbf{T}}_{\text{dist}} + \tilde{\mathbf{T}}_{\text{ctrl}}) \\ = & \mathbf{I}^{-1} \{ \bar{\mathbf{T}}_{\text{dist}} + \bar{\mathbf{T}}_{\text{ctrl}} - [\bar{\omega} \times] (\mathbf{I} \cdot \bar{\omega}) \} + \mathbf{I}^{-1} \{ [\mathbf{I} \cdot \bar{\omega} \times] - [\bar{\omega} \times] \mathbf{I} \} \tilde{\omega} + \mathbf{I}^{-1} \cdot (\tilde{\mathbf{T}}_{\text{dist}} + \tilde{\mathbf{T}}_{\text{ctrl}}) \end{aligned} \quad (7.16)$$

Differentiating Eq. 7.14 and substituting to Eq. 7.16:



$$\tilde{\dot{\omega}} = \mathbf{I}^{-1} \{ [\mathbf{I} \cdot \bar{\omega} \times] - [\bar{\omega} \times] \mathbf{I} \} \tilde{\omega} + \mathbf{I}^{-1} \cdot (\tilde{\mathbf{T}}_{\text{dist}} + \tilde{\mathbf{T}}_{\text{ctrl}}) \quad (7.17)$$

Next, kinematic equation Eq. 7.12 is linearized. Subscripts and superscripts are omitted for clarity. It is assumed that quaternion \mathbf{q} describes the attitude of satellite's body frame with reference to ECI inertial frame and angular rate vector ω represents the satellite's body frame angular rate relative to ECI inertial frame and is expressed in satellite's body frame.

$$\dot{\mathbf{q}} = \frac{1}{2} \omega \otimes \mathbf{q} \quad (7.12)$$

Above equation is linearized around some nominal value $\bar{\mathbf{q}}$ with small attitude error $\tilde{\mathbf{q}}$, so that:

$$\mathbf{q} = \tilde{\mathbf{q}} \otimes \bar{\mathbf{q}} \quad (7.18)$$

	PW-Sat2	Preliminary Design Review	
	2016-11-22	Attitude Determination and Control System	
	Phase B		

Extracting small attitude error $\tilde{\mathbf{q}}$ we can write:

$$\tilde{\mathbf{q}} = \mathbf{q} \otimes \bar{\mathbf{q}}^* \quad (7.19)$$

where $\bar{\mathbf{q}}^*$ denotes conjugate of nominal quaternion $\bar{\mathbf{q}}$ defined as $\bar{\mathbf{q}}^* = [-\bar{\mathbf{q}}_{1:3} \quad \bar{q}_4]^T$. Differentiating Eq. 7.19 and substituting Eq. 7.12 gives:

$$\begin{aligned} \dot{\tilde{\mathbf{q}}} &= \dot{\mathbf{q}} \otimes \bar{\mathbf{q}}^* + \mathbf{q} \otimes \dot{\bar{\mathbf{q}}}^* \\ &= \frac{1}{2} \boldsymbol{\omega} \otimes \mathbf{q} \otimes \bar{\mathbf{q}}^* + \mathbf{q} \otimes \dot{\bar{\mathbf{q}}}^* \end{aligned} \quad (7.20)$$

Nominal values satisfy Eq. 7.12, therefore:

$$\dot{\bar{\mathbf{q}}} = \frac{1}{2} \bar{\boldsymbol{\omega}} \otimes \bar{\mathbf{q}} \quad (7.21)$$

Substituting Eq. 7.21 into Eq. 7.20 gives:

$$\begin{aligned} \dot{\tilde{\mathbf{q}}} &= \frac{1}{2} \boldsymbol{\omega} \otimes \mathbf{q} \otimes \bar{\mathbf{q}}^* + \mathbf{q} \otimes \left[\frac{1}{2} \bar{\boldsymbol{\omega}} \otimes \bar{\mathbf{q}} \right]^* \\ &= \frac{1}{2} \boldsymbol{\omega} \otimes \mathbf{q} \otimes \bar{\mathbf{q}}^* + \frac{1}{2} \mathbf{q} \otimes \bar{\mathbf{q}}^* \otimes \bar{\boldsymbol{\omega}} \end{aligned} \quad (7.22)$$

where identities for conjugate of quaternion multiplication was used.

Taking into account that $\bar{\boldsymbol{\omega}}^* = -\bar{\boldsymbol{\omega}}$ we can write Eq. 7.22:

$$\dot{\tilde{\mathbf{q}}} = \frac{1}{2} \boldsymbol{\omega} \otimes \mathbf{q} \otimes \bar{\mathbf{q}}^* - \frac{1}{2} \mathbf{q} \otimes \bar{\mathbf{q}}^* \otimes \bar{\boldsymbol{\omega}} \quad (7.23)$$

Substituting Eqs. 7.18 and 7.19 for \mathbf{q} and $\tilde{\mathbf{q}}$ respectively and rearranging terms:



$$\begin{aligned} \dot{\tilde{\mathbf{q}}} &= \frac{1}{2} \boldsymbol{\omega} \otimes \tilde{\mathbf{q}} - \frac{1}{2} \tilde{\mathbf{q}} \otimes \bar{\mathbf{q}} \otimes \bar{\mathbf{q}}^* \otimes \bar{\boldsymbol{\omega}} \\ &= \frac{1}{2} [\boldsymbol{\omega} \otimes \tilde{\mathbf{q}} - \tilde{\mathbf{q}} \otimes \bar{\boldsymbol{\omega}}] \end{aligned} \quad (7.24)$$

Substituting $\boldsymbol{\omega} = \bar{\boldsymbol{\omega}} + \tilde{\boldsymbol{\omega}}$ into Eq. 7.24:

$$\begin{aligned} \dot{\tilde{\mathbf{q}}} &= \frac{1}{2} [(\bar{\boldsymbol{\omega}} + \tilde{\boldsymbol{\omega}}) \otimes \tilde{\mathbf{q}} - \tilde{\mathbf{q}} \otimes \bar{\boldsymbol{\omega}}] \\ &= \frac{1}{2} (\bar{\boldsymbol{\omega}} \otimes \tilde{\mathbf{q}} - \tilde{\mathbf{q}} \otimes \bar{\boldsymbol{\omega}}) + \frac{1}{2} \tilde{\boldsymbol{\omega}} \otimes \tilde{\mathbf{q}} \end{aligned} \quad (7.25)$$

Last factor on the right-hand side of Eq. 7.25 can be written as:

$$\frac{1}{2} \tilde{\boldsymbol{\omega}} \otimes \tilde{\mathbf{q}} = \frac{1}{2} \tilde{\boldsymbol{\omega}} \otimes (\tilde{\mathbf{q}} - \mathbf{I}_q + \mathbf{I}_q) \quad (7.26)$$

	PW-Sat2	Preliminary Design Review	
	2016-11-22	Attitude Determination and Control System	
	Phase B		

where $\mathbf{I}_q = [\mathbf{0}_{1 \times 3} \quad 1]^T$ is an identity quaternion. Both $\tilde{\mathbf{w}}$ and $\tilde{\mathbf{q}} - \mathbf{I}_q$ are small, therefore their product can be neglected.

$$\frac{1}{2} \tilde{\mathbf{w}} \otimes \tilde{\mathbf{q}} \approx \frac{1}{2} \tilde{\mathbf{w}} \otimes \mathbf{I}_q = \frac{1}{2} \tilde{\mathbf{w}} \quad (7.27)$$

Substituting Eq. 7.27 into Eq. 7.25 and using quaternion multiplication \odot with the opposite order of multiplication than \otimes we obtain:

$$\tilde{\mathbf{q}} = \frac{1}{2} \left\{ \begin{bmatrix} \tilde{\mathbf{w}} \\ 0 \end{bmatrix} \otimes \tilde{\mathbf{q}} - \begin{bmatrix} \tilde{\mathbf{w}} \\ 0 \end{bmatrix} \odot \tilde{\mathbf{q}} \right\} + \frac{1}{2} \tilde{\mathbf{w}} \quad (7.28)$$

where

$$\begin{bmatrix} \tilde{\mathbf{w}} \\ 0 \end{bmatrix} \otimes = \begin{bmatrix} -[\tilde{\mathbf{w}} \times] & \tilde{\mathbf{w}} \\ -\tilde{\mathbf{w}}^T & 0 \end{bmatrix} \quad (7.29a)$$

$$\begin{bmatrix} \tilde{\mathbf{w}} \\ 0 \end{bmatrix} \odot = \begin{bmatrix} [\tilde{\mathbf{w}} \times] & \tilde{\mathbf{w}} \\ -\tilde{\mathbf{w}}^T & 0 \end{bmatrix} \quad (7.29b)$$

Rearranging terms and multiplying gives:

$$\tilde{\mathbf{q}} = - \begin{bmatrix} \tilde{\mathbf{w}} \times \tilde{\mathbf{q}}_{1:3} \\ 0 \end{bmatrix} + \frac{1}{2} \begin{bmatrix} \tilde{\mathbf{w}} \\ 0 \end{bmatrix} \quad (7.30)$$



7.3 ATTITUDE DETERMINATION AND ESTIMATION

In this chapter algorithms for attitude determination and estimation are presented. Wahba's Problem is discussed and two simplest algorithms are presented. Besides static attitude determination methods, estimation techniques are investigated. Simplest form of Multiplicative Extended Kalman Filter (MEKF) with no sensors' bias estimation is discussed. The algorithm of MEKF is presented step by step.

7.3.1 WAHBA'S PROBLEM

When the attitude of a body is considered, at least three parameters are needed. The common approach is to use unit vector observations. However, one vector observation is not sufficient because it provides 2-angle information. Therefore, at least two unit vector observations are required, providing 4 parameters in total. Thus the attitude is *overdetermined*. However, one additional parameter can be used when one vector observation is more accurate than the other one. Weights can be determined in order to put more 'trust' in more accurate observation.

If two or more unit vector observations are known in different coordinate frames, i.e. body and reference, the orthogonal attitude matrix ${}^b_r\mathbf{A}$ can be computed. Subscript r denotes reference frame and superscript b denotes body frame. In general, when unit vectors observations are measured with some errors, matrix ${}^b_r\mathbf{A}$ can be computed optimally. Grace Wahba formulated the problem mathematically. The goal is to find the orthogonal attitude matrix with the determinant +1 which minimizes the loss function [1]:

	PW-Sat2	Preliminary Design Review	
	2016-11-22	Attitude Determination and Control System	
	Phase B		

$$L(\underline{\mathbf{A}}) \equiv \frac{1}{2} \sum_{i=1}^N a_i \|\mathbf{b}_i - \underline{\mathbf{A}} \mathbf{r}_i\|^2 \quad (7.31)$$

where \mathbf{b}_i is i-th unit vector observation in body frame, \mathbf{r}_i is the corresponding unit vector in reference frame and a_i is non-negative weight for i-th unit vector.

The problem can be expressed in a more convenient way:

$$L(\underline{\mathbf{A}}) = \lambda_0 - \text{tr}(\underline{\mathbf{A}} \cdot \underline{\mathbf{B}}^T) \quad (7.32)$$

where

$$\lambda_0 \equiv \sum_{i=1}^N a_i \quad (7.33)$$

and the “attitude profile matrix” $\underline{\mathbf{B}}$ is defined as

$$\underline{\mathbf{B}} \equiv \sum_{i=1}^N a_i \mathbf{b}_i \mathbf{r}_i^T \quad (7.34)$$

There are many algorithms for solving Wahba’s problem. Theoretically, they provide the same optimal solution. However, the solution may slightly differ due to the computational errors. Most widely used algorithms are TRIAD, Davenport’s q, QUEST, ESOQ, ESOQ2, Singular Value Decomposition (SVD) and FOAM. The team has decided to use general TRIAD algorithm with two observations weighted. It proved to be a bit faster than QUEST and it is simpler. In next two chapters simple and general forms of TRIAD algorithm are presented.

7.3.2 THE TRIAD ALGORITHM

The TRIAD algorithm is based on two unit vector observations in body and reference frames.

Let \mathbf{b}_1 and \mathbf{b}_2 denote two unit vector observations in body frame and \mathbf{r}_1 and \mathbf{r}_2 corresponding unit vectors in reference frame. Then, the attitude matrix transforming vector from reference frame to body frame is:

$$\underline{\mathbf{A}} \mathbf{r}_i = \mathbf{b}_i, \quad \text{for } i = 1, 2 \quad (7.35)$$

The simplest form of TRIAD algorithm doesn’t account for errors in observations, thus it is assumed that the attitude matrix $\underline{\mathbf{A}}$ satisfies Eq. 7.35 for both $i = 1, 2$. Then, the attitude matrix equals:



$$\underline{\mathbf{A}}_{\text{TRIAD}} = \mathbf{b}_1 \mathbf{r}_1^T + (\mathbf{b}_1 \times \mathbf{b}_2)(\mathbf{r}_1 \times \mathbf{r}_2)^T + \mathbf{b}_2 \mathbf{r}_2^T \quad (7.36)$$

where

$$\mathbf{b}_\times = \frac{\mathbf{b}_1 \times \mathbf{b}_2}{\|\mathbf{b}_1 \times \mathbf{b}_2\|} \quad (7.37a)$$

$$\mathbf{r}_\times = \frac{\mathbf{r}_1 \times \mathbf{r}_2}{\|\mathbf{r}_1 \times \mathbf{r}_2\|} \quad (7.37b)$$

7.3.3 THE GENERAL FORM OF TRIAD ALGORITHM

	PW-Sat2	Preliminary Design Review	
	2016-11-22	Attitude Determination and Control System	
	Phase B		

The general form of TRIAD algorithm requires two unit vector observations in body and reference frames. Also measurement's weights are included.

The attitude matrix transforming vector from reference frame to the body frame can be computed as an optimal solution of Wahba's Problem with two observations [1]:

$$\underline{\mathbf{A}} = (a_1/\lambda_{\max})[\mathbf{b}_1\mathbf{r}_1^T + (\mathbf{b}_1 \times \mathbf{b}_x)(\mathbf{r}_1 \times \mathbf{r}_x)^T] + (a_2/\lambda_{\max})[\mathbf{b}_2\mathbf{r}_2^T + (\mathbf{b}_2 \times \mathbf{b}_x)(\mathbf{r}_2 \times \mathbf{r}_x)^T] + \mathbf{b}_x\mathbf{r}_x^T \quad (7.38)$$

where

$$\lambda_{\max} = \{a_1^2 + a_2^2 + 2a_1a_2[(\mathbf{b}_1 \cdot \mathbf{b}_2)(\mathbf{r}_1 \cdot \mathbf{r}_2) + \|\mathbf{b}_1 \times \mathbf{b}_2\| \|\mathbf{r}_1 \times \mathbf{r}_2\|]\}^{1/2} \quad (7.39)$$

Weights a_1 and a_2 are inversely proportional to the measurement variances, thus:

$$a_i = c/\sigma_i^2 \quad (7.40)$$

where σ_i^2 is the overall measurement variance and is defined as the sum of error variances of body and reference frame vectors:

$$\sigma_i^2 \equiv \sigma_{b,i}^2 + \sigma_{r,i}^2 \quad (7.41)$$

Constant c in Eq. 7.40 can be selected so that weights a_1 and a_2 sum to unity:

$$c = (\sum_{i=1}^2 \sigma_i^{-2})^{-1} \quad (7.42)$$



By inspecting Eq. 7.38, it can be seen that weighted general formulation of TRIAD approaches simple formulation in Eq. 7.36 if $a_2 = 0$ for $\sigma_2^2 \rightarrow \infty$, i.e. when 2nd observation is highly inaccurate. If $a_1 = 0$, the roles of unit vectors are interchanged and instead of subscript 1 in Eq. 7.36, subscript 2 should be used. However, if observations are known precisely with no errors, changing subscript 1 for 2 in Eq. 7.36, gives the same solution. For general weights with errors present, Eq. 7.38 is sort of averaged solution of these two TRIAD's limits.

7.3.4 MULTIPLICATIVE EXTENDED KALMAN FILTER (MEKF)

Static attitude determination methods described in the previous chapter can be employed when sufficient number of unit vectors observations is available. However, the result is usually noisy and inaccurate due to the sensors' errors. The attitude estimation techniques utilizes process's and observation's equations which are closely related to dynamics and kinematics equations when angular rate and attitude are estimated. Additionally, process's and observations' noise are modeled.

In this chapter, brief description of general EKF equations is presented. State transition and observation Jacobians are derived. Algorithm of MEKF for attitude and angular rate is presented.

7.3.4.1 Introduction to EKF

	PW-Sat2	Preliminary Design Review	
	2016-11-22	Attitude Determination and Control System	
	Phase B		

Extended Kalman Filter is an iterative procedure and can be divided into two major steps: *prediction* and *update*.

In *prediction* step, current state estimate $\mathbf{x}_{k|k}$ and current covariance $\mathbf{P}_{k|k}$ in k-th step are propagated using process's equations, obtaining a priori predicted state $\mathbf{x}_{k+1|k}$ and covariance $\mathbf{P}_{k+1|k}$ for next k+1 step.

In *update* step, a priori state and covariance are corrected using linear weighted combination of a predicted a priori values and measurement \mathbf{z}_{k+1} in k+1 step, obtaining a posteriori state estimate $\mathbf{x}_{k+1|k+1}$ and covariance $\mathbf{P}_{k+1|k+1}$ for the next step. Weight is given by the Kalman gain matrix \mathbf{K}_{k+1} .

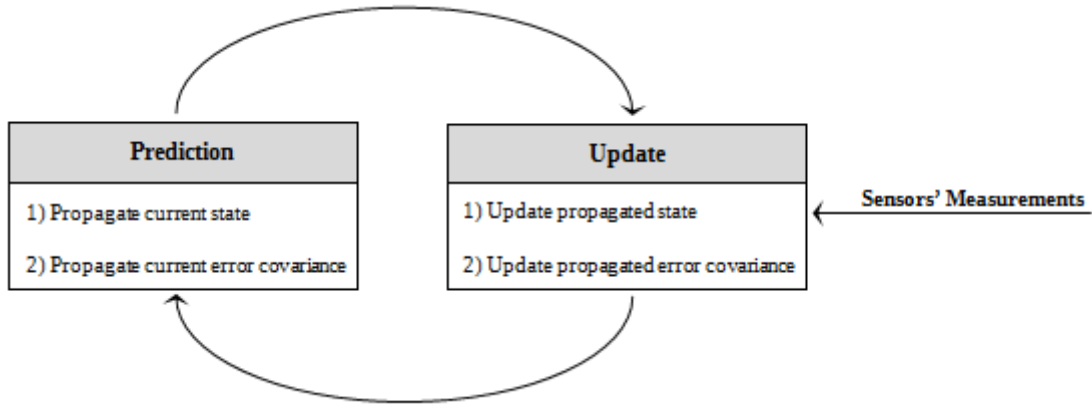


Figure 7-2 Kalman filter cycle

The equations for general Extended Kalman Filter formulation are presented below.

Extended Kalman Filter consists of two equations representing the process and observation:

$$\mathbf{x}_k = f(\mathbf{x}_{k-1}, \mathbf{u}_{k-1}) + \mathbf{w}_{k-1} \quad (7.43a)$$

$$\mathbf{z}_k = h(\mathbf{x}_k) + \mathbf{v}_k \quad (7.43b)$$

where

\mathbf{x}_k state estimate vector at time k

f nonlinear process model



h nonlinear observation model

\mathbf{u}_{k-1} exogenous inputs at time $k-1$

\mathbf{z}_k measurement vector at time k

\mathbf{w}_{k-1} process noise

\mathbf{v}_k observation noise

	PW-Sat2	Preliminary Design Review	
	2016-11-22	Attitude Determination and Control System	
	Phase B		

In Kalman filter derivation it is assumed that process's noise \mathbf{w} and observation's noise \mathbf{v} are zero-mean Gaussian. They are uncorrelated, therefore process's covariance matrix $\underline{\mathbf{Q}}$ and observation's covariance matrix $\underline{\mathbf{R}}$ are diagonal.

Prediction

The a priori state estimate $\mathbf{x}_{k|k-1}$ is calculated using nonlinear model in Eq. 7.43a, a posteriori previous estimate $\mathbf{x}_{k-1|k-1}$ and exogenous inputs \mathbf{u}_{k-1} :

$$\mathbf{x}_{k|k-1} = f(\mathbf{x}_{k-1|k-1}, \mathbf{u}_{k-1}) \quad (7.44)$$

This can be calculated using Eq. 7.43a for \mathbf{w} equal 0.

A priori covariance prediction can be computed:

$$\underline{\mathbf{P}}_{k|k-1} = \underline{\Phi}_{k-1|k-1} \underline{\mathbf{P}}_{k-1|k-1} \underline{\Phi}_{k-1|k-1}^T + \underline{\mathbf{Q}} \quad (7.45)$$

where $\underline{\Phi}_{k-1|k-1}$ is Jacobian matrix of discrete process's nonlinear model, defined as:

$$\underline{\Phi}_{k-1|k-1} = \left. \frac{\partial f}{\partial \mathbf{x}} \right|_{\mathbf{x}=\mathbf{x}_{k-1|k-1}} \quad (7.46)$$

Update

The a priori state is corrected with measurement \mathbf{z}_k . Before that, prediction of a measurement is calculated based on observation model in Eq. 7.43b:

$$\mathbf{z}_{k|k-1} = h(\mathbf{x}_{k|k-1}) \quad (7.47)$$

The a posteriori state $\mathbf{x}_{k|k}$ is computed using linear combination of a priori state and current measurement \mathbf{z}_k :

$$\mathbf{x}_{k|k} = \mathbf{x}_{k|k-1} + \underline{\mathbf{K}}_k (\mathbf{z}_k - \mathbf{z}_{k|k-1}) \quad (7.48)$$

where Kalman gain $\underline{\mathbf{K}}_k$ is calculated so that the error between predicted and measured value is minimized:



$$\underline{\mathbf{K}}_k = \underline{\mathbf{P}}_{k|k-1} \underline{\mathbf{H}}_k^T (\underline{\mathbf{H}}_k \underline{\mathbf{P}}_{k|k-1} \underline{\mathbf{H}}_k^T + \underline{\mathbf{R}})^{-1} \quad (7.49)$$



where $\underline{\mathbf{H}}_k$ is Jacobian matrix of observation nonlinear model, defined as:

$$\underline{\mathbf{H}}_k = \left. \frac{\partial h}{\partial \mathbf{x}} \right|_{\mathbf{x}=\mathbf{x}_{k|k-1}} \quad (7.50)$$

The predicted a priori covariance matrix $\underline{\mathbf{P}}_{k|k-1}$ is updated, obtaining a posteriori covariance matrix $\underline{\mathbf{P}}_{k|k}$:

$$\underline{\mathbf{P}}_{k|k} = (\underline{\mathbf{I}} - \underline{\mathbf{K}}_k \underline{\mathbf{H}}_k) \underline{\mathbf{P}}_{k|k-1} \quad (7.51)$$

	PW-Sat2	Preliminary Design Review	
	2016-11-22	Attitude Determination and Control System	
	Phase B		

	PW-Sat2	Preliminary Design Review	
	2016-11-22	Attitude Determination and Control System	
	Phase B		

7.3.4.2 MEKF for Attitude and Angular Rate Estimation

In this chapter equations for attitude and angular rate estimation based on EKF are presented. State and measurement vectors are described, associated with Jacobian matrices and process's equations derivation.

State vector is based on quaternion describing rotation from ECI inertial frame to satellite's body frame and angular rate of satellite's body frame relative to ECI inertial frame expressed in satellite's frame:

$$\mathbf{x} = [\mathbf{s}_i \mathbf{q}^T \quad \mathbf{s} \boldsymbol{\omega}_{s/i}^T]^T = [q_1 \quad q_2 \quad q_3 \quad q_4 \quad \omega_x \quad \omega_y \quad \omega_z]^T \quad (7.52)$$

The 6-element error state can be defined as:

$$\tilde{\mathbf{x}} = [\mathbf{s}_i \tilde{\mathbf{q}}^T \quad \mathbf{s} \tilde{\boldsymbol{\omega}}_{s/i}^T]^T = [\tilde{q}_1 \quad \tilde{q}_2 \quad \tilde{q}_3 \quad \tilde{\omega}_x \quad \tilde{\omega}_y \quad \tilde{\omega}_z]^T \quad (7.53)$$

When the object's attitude is described by a quaternion, one have to use quaternion multiplication equations. Kalman update is based on linear additive process, however, adding two quaternions does not have mathematical sense in terms of the attitude calculation. To obey the quaternion unit norm, quaternion update is multiplied based on the quaternion algebra rules.

In MEKF formulation, the calculations are performed on error state $\tilde{\mathbf{x}}$ which is expanded to full state \mathbf{x} after the a posteriori error state is computed. MEKF uses a continuous process's prediction model with discrete measurements update. Therefore, the full state \mathbf{x} is propagated using continuous dynamics and kinematics equations. The covariance matrix is propagated using discrete model with discrete state transition matrix, Φ . The sequence of computations is presented below.

Propagation of full state \mathbf{x} in the next step is computed on the basis of dynamics and kinematics equations derived in chapter 7.2.1. For clarity, subscripts and superscripts are omitted.



$$\begin{bmatrix} \dot{\mathbf{q}} \\ \dot{\boldsymbol{\omega}} \end{bmatrix} = \begin{bmatrix} \frac{1}{2} \boldsymbol{\omega} \otimes \mathbf{q} \\ \mathbf{I}^{-1} \{ \mathbf{T}_{ctrl} - [\boldsymbol{\omega} \times] (\mathbf{I} \cdot \boldsymbol{\omega}) \} \end{bmatrix} \quad (7.54)$$

Runge-Kutta 4th order procedure is used and quaternion is normalized after propagation. Disturbance torque has been omitted since its value is not known.

The Jacobian \mathbf{F} for continuous time nonlinear error state process's model can be found by linearizing dynamics and kinematics equations which has been done in chapter 7.2.2. The result is presented below.

$$\begin{bmatrix} \dot{\tilde{\mathbf{q}}}_{1:3} \\ \dot{\tilde{\boldsymbol{\omega}}} \end{bmatrix} = \begin{bmatrix} -[\tilde{\boldsymbol{\omega}} \times] & \frac{1}{2} \mathbf{1}_{3 \times 3} \\ \mathbf{0}_{3 \times 3} & \mathbf{I}^{-1} \{ [\mathbf{I} \cdot \tilde{\boldsymbol{\omega}} \times] - [\tilde{\boldsymbol{\omega}} \times] \mathbf{I} \} \end{bmatrix} \begin{bmatrix} \tilde{\mathbf{q}}_{1:3} \\ \tilde{\boldsymbol{\omega}} \end{bmatrix} + \begin{bmatrix} \mathbf{0}_{3 \times 3} \\ \mathbf{I}^{-1} \end{bmatrix} (\tilde{\mathbf{T}}_{dist} + \tilde{\mathbf{T}}_{ctrl}) \quad (7.55)$$

Above equation can be identified with general definition of the state transition matrix for continuous error state model:

	PW-Sat2	Preliminary Design Review	
	2016-11-22	Attitude Determination and Control System	
	Phase B		

$$\dot{\tilde{\mathbf{x}}} = \underline{\mathbf{F}} \tilde{\mathbf{x}}$$

Therefore:

$$\underline{\mathbf{F}} = \begin{bmatrix} -[\underline{\boldsymbol{\omega}} \times] & \frac{1}{2} \underline{\mathbf{1}}_{3 \times 3} \\ \underline{\mathbf{0}}_{3 \times 3} & \underline{\mathbf{I}}^{-1} \{ [\underline{\mathbf{I}} \cdot \underline{\boldsymbol{\omega}} \times] - [\underline{\boldsymbol{\omega}} \times] \underline{\mathbf{I}} \} \end{bmatrix} \quad (7.56)$$

Discrete Jacobian state transition matrix can be computed as:

$$\underline{\Phi} = e^{\underline{\mathbf{F}} \cdot \Delta t} \approx \underline{\mathbf{1}} + \underline{\mathbf{F}} \cdot \Delta t \quad (7.57)$$

where above approximation is valid for small time steps.

The 9-element measurement vector \mathbf{z}_k at k step is:

$$\mathbf{z}_k = [\mathbf{s} \mathbf{b}_{\text{mag}}^T \quad \mathbf{s} \mathbf{b}_{\text{sun}}^T \quad \mathbf{s} \boldsymbol{\omega}_{\text{s/i}}^T]^T \quad (7.58)$$

where subscripts *mag* and *sun* denote magnetic field vector measurement and sun vector measurement, respectively. Magnetic field vectors and sun vectors are unit vectors. Therefore, measurements have to be normalized.

A priori measurement prediction $\mathbf{z}_{k|k-1}$ can be computed with a priori full quaternion $\mathbf{q}_{k|k-1}$ and angular rate $\boldsymbol{\omega}_{k|k-1}$ prediction:

$$\mathbf{z}_{k|k-1} = \begin{bmatrix} {}^{\text{s}}\underline{\mathbf{A}}(\mathbf{q}_{k|k-1})^{\text{i}} \mathbf{r}_{\text{mag}} \\ {}^{\text{s}}\underline{\mathbf{A}}(\mathbf{q}_{k|k-1})^{\text{i}} \mathbf{r}_{\text{sun}} \\ \boldsymbol{\omega}_{k|k-1} \end{bmatrix} \quad (7.59)$$

where reference vectors denoted by \mathbf{r} are expressed in ECI inertial frame and are calculated based on reference IGRF and Sun Position models with the satellite's position on orbit known. In Eq. 7.59 calculations are performed on unit reference vectors, therefore reference vectors have to be normalized.

In order to calculate Jacobian matrix of observation nonlinear model $\underline{\mathbf{H}}_k$ we have to relate $\mathbf{z}_k - \mathbf{z}_{k|k-1}$ with error state $\tilde{\mathbf{x}}$ (compare with Eq. 7.50). The derivation for angular rate is rather straightforward, therefore we will focus on unit vector observations. The derivation follows as [3].



Rotation matrix can be expressed in terms of a quaternion [1]:

$$\underline{\mathbf{A}}(\mathbf{q}) = (q_4^2 - \|\mathbf{q}_{1:3}\|^2) \underline{\mathbf{1}}_{3 \times 3} - 2q_4 [\mathbf{q}_{1:3} \times] + 2\mathbf{q}_{1:3} \mathbf{q}_{1:3}^T \quad (7.60)$$

Using small rotation approximation, $q_4 \approx 1$ and powers of $\mathbf{q}_{1:3}$ higher than 1 can be neglected.

$$\underline{\mathbf{A}}(\tilde{\mathbf{q}}) \approx \underline{\mathbf{1}}_{3 \times 3} - 2[\tilde{\mathbf{q}}_{1:3} \times] \quad (7.61)$$

Taking into account, that $\underline{\mathbf{A}}(\mathbf{q}) = \underline{\mathbf{A}}(\tilde{\mathbf{q}}) \underline{\mathbf{A}}(\bar{\mathbf{q}})$ we can write:

	PW-Sat2	Preliminary Design Review	
	2016-11-22	Attitude Determination and Control System	
	Phase B		

$$\underline{\mathbf{A}}(\mathbf{q}) \approx \{\underline{\mathbf{1}}_{3 \times 3} - 2[\tilde{\mathbf{q}}_{1:3} \times]\} \underline{\mathbf{A}}(\bar{\mathbf{q}}) \quad (7.62)$$

Let consider an observation unit vector in ECI inertial frame and satellite's body frame at k step:

$${}^s\mathbf{b}_k = {}^s_i \underline{\mathbf{A}}(\mathbf{q}_k) {}^i\mathbf{r}_k \quad (7.63)$$

Substituting Eq. 7.62 into Eq. 7.63:

$$\begin{aligned} {}^s\mathbf{b}_k &\approx \{\underline{\mathbf{1}}_{3 \times 3} - 2[\tilde{\mathbf{q}}_{1:3,k} \times]\} {}^s_i \underline{\mathbf{A}}(\mathbf{q}_{k|k-1}) {}^i\mathbf{r}_k \\ &\approx \{\underline{\mathbf{1}}_{3 \times 3} - 2[\tilde{\mathbf{q}}_{1:3,k} \times]\} {}^s\mathbf{b}_{k|k-1} \end{aligned} \quad (7.64)$$

By multiplying and rearranging terms:

$${}^s\mathbf{b}_k - {}^s\mathbf{b}_{k|k-1} \approx -2[\tilde{\mathbf{q}}_{1:3,k} \times] {}^s\mathbf{b}_{k|k-1} \quad (7.65)$$

Reversing the order of skew-symmetric multiplication:

$${}^s\mathbf{b}_k - {}^s\mathbf{b}_{k|k-1} \approx 2[{}^s\mathbf{b}_{k|k-1} \times] \tilde{\mathbf{q}}_{1:3,k} \quad (7.66)$$

With this formula derived, we can write:

$$\tilde{\mathbf{z}}_k = \mathbf{z}_k - \mathbf{z}_{k|k-1} = \underline{\mathbf{H}}_k \begin{bmatrix} \tilde{\mathbf{q}}_{1:3,k} \\ \tilde{\boldsymbol{\omega}}_k \end{bmatrix} \quad (7.67)$$

Jacobian matrix of nonlinear observation model can be written as:

$$\underline{\mathbf{H}}_k = \begin{bmatrix} 2[{}^s\mathbf{b}_{\text{mag},k|k-1} \times] & \underline{\mathbf{0}}_{3 \times 3} \\ 2[{}^s\mathbf{b}_{\text{sun},k|k-1} \times] & \underline{\mathbf{0}}_{3 \times 3} \\ \underline{\mathbf{0}}_{3 \times 3} & \underline{\mathbf{1}}_{3 \times 3} \end{bmatrix} \quad (7.68)$$



where ${}^s\mathbf{b}_{\text{mag},k|k-1}$ is predicted measurement of magnetic field unit vector based on Eq. 7.59. Similarly for measurement of sun sensor unit vector.

When a posteriori error quaternion $\tilde{\mathbf{q}}_{1:3,k|k}$ is computed, it have to be expanded to full quaternion $\mathbf{q}_{k|k}$. Error quaternion can be expressed in a following way:

$$\tilde{\mathbf{q}}_{k|k} = \mathbf{I}_q + \begin{bmatrix} \tilde{\mathbf{q}}_{1:3,k|k} \\ 0 \end{bmatrix} \quad (7.69)$$

It can be expanded to full quaternion $\mathbf{q}_{k|k}$ using the predicted a priori quaternion $\mathbf{q}_{k|k-1}$:

$$\begin{aligned} \mathbf{q}_{k|k} &= \tilde{\mathbf{q}}_{k|k} \otimes \mathbf{q}_{k|k-1} = \left(\mathbf{I}_q + \begin{bmatrix} \tilde{\mathbf{q}}_{1:3,k|k} \\ 0 \end{bmatrix} \right) \otimes \mathbf{q}_{k|k-1} \\ &= \mathbf{q}_{k|k-1} + [\mathbf{q}_{k|k-1} \odot] \tilde{\mathbf{q}}_{1:3,k|k} \end{aligned} \quad (7.70)$$

	PW-Sat2	Preliminary Design Review	
	2016-11-22	Attitude Determination and Control System	
	Phase B		

where

$$[\mathbf{q} \odot] = \begin{bmatrix} q_4 \mathbf{1}_{3 \times 3} + [\mathbf{q}_{1:3} \times] & \mathbf{q}_{1:3} \\ -\mathbf{q}_{1:3}^T & q_4 \end{bmatrix} = [\Xi(\mathbf{q}) \quad \mathbf{q}] \quad (7.71)$$

By multiplying terms in Eq. 7.70:

$$\mathbf{q}_{k|k} = \mathbf{q}_{k|k-1} + \Xi(\mathbf{q}_{k|k-1}) \tilde{\mathbf{q}}_{1:3,k|k} \quad (7.72)$$

Quaternion $\mathbf{q}_{k|k}$ is then normalized.

Based on the set of simulations, process's, measurement and initial covariance matrices was set to:

$$\underline{\mathbf{Q}} = \text{diag}(1 \quad 1 \quad 1 \quad 10 \quad 10 \quad 10) 10^{-8}$$

$$\underline{\mathbf{R}} = \text{diag}(2.5 \quad 2.5 \quad 2.5 \quad 10 \quad 10 \quad 10 \quad 0.07 \quad 0.07 \quad 0.07) 10^{-3}$$

$$\underline{\mathbf{P}}_0 = \text{diag}(1 \quad 1 \quad 1 \quad 10 \quad 10 \quad 10) 10^{-4}$$





	PW-Sat2	Preliminary Design Review	
	2016-11-22	Attitude Determination and Control System	
	Phase B		

Table 7-2 MEKF Attitude and Angular Rate Estimation Algorithm

Initialization outside eclipse		
0.1	Get measurements	${}^s\mathbf{b}_{\text{mag},0}, {}^s\mathbf{b}_{\text{sun},0}, {}^s\boldsymbol{\omega}_{s/i,0}$
0.2	Solve Wahba (general TRIAD)	${}^i\mathbf{A}$ according to Eq. 7.38
0.3	Calculate ${}^i\mathbf{q}_0$	${}^i\mathbf{A}$ to ${}^i\mathbf{q}_0$ conversion
0.4	Initialize MEKF	$\mathbf{x}_{k-1 k-1} = [{}^i\mathbf{q}_0^T \quad {}^s\boldsymbol{\omega}_{s/i,0}^T]^T, \mathbf{P}_{k-1 k-1} = \mathbf{P}_0, {}^s\mathbf{T}_{\text{ctrl},k-1} = \mathbf{0}$
Prediction		
1.1	Propagate state	$\mathbf{x}_{k k-1} = \text{RK4}(\mathbf{x}_{k-1 k-1}, {}^s\mathbf{T}_{\text{ctrl},k-1}, \Delta t)$
1.2	Normalize a priori quaternion	${}^i\mathbf{q}_{k k-1} / \ {}^i\mathbf{q}_{k k-1}\ \rightarrow {}^i\mathbf{q}_{k k-1}$
1.3	Calculate continuous process Jacobian	$\mathbf{F}_{k-1 k-1}$ according to Eq. 7.56
1.4	Calculate discrete process Jacobian	$\Phi_{k-1 k-1} = \mathbf{I}_{6 \times 6} + \mathbf{F} \cdot \Delta t$
1.5	A priori covariance	$\mathbf{P}_{k k-1} = \Phi_{k-1 k-1} \mathbf{P}_{k-1 k-1} \Phi_{k-1 k-1}^T + \mathbf{Q}$
Update		
2.1	Calculate predicted rotation matrix	$\mathbf{q}_{k k-1}$ to ${}^i\mathbf{A}(\mathbf{q}_{k k-1})$ conversion
2.2	Check if eclipse	if in eclipse go to 2.6, else go to 2.3
2.3	Get new measurement	get Sun Sensor measurement ${}^s\mathbf{z}_{\text{sun},k}$
2.4	Normalize measurement	${}^s\mathbf{b}_{\text{sun},k} = {}^s\mathbf{z}_{\text{sun},k} / \ {}^s\mathbf{z}_{\text{sun},k}\ $
2.5	Predict measurement	${}^s\mathbf{b}_{\text{sun},k k-1} = {}^i\mathbf{A}(\mathbf{q}_{k k-1})^T \mathbf{r}_{\text{sun},k}$, go to 2.7
2.6	Set Sun Sensor measurement	${}^s\mathbf{b}_{\text{sun},k} = {}^s\mathbf{b}_{\text{sun},k k-1} = [0 \quad 0 \quad 0]^T$
2.7	Repeat steps	repeat 2.3-2.5 for magnetic field measurement repeat 2.3, 2.5 for angular rate measurement
2.8	Calculate observation Jacobian	$\mathbf{H}_k = \begin{bmatrix} 2[{}^s\mathbf{b}_{\text{mag},k k-1} \times] & \mathbf{0}_{3 \times 3} \\ 2[{}^s\mathbf{b}_{\text{sun},k k-1} \times] & \mathbf{0}_{3 \times 3} \\ \mathbf{0}_{3 \times 3} & \mathbf{I}_{3 \times 3} \end{bmatrix}$
2.9	Calculate Kalman gain	$\mathbf{K}_k = \mathbf{P}_{k k-1} \mathbf{H}_k^T (\mathbf{H}_k \mathbf{P}_{k k-1} \mathbf{H}_k^T + \mathbf{R})^{-1}$
2.10	Calculate error state	$\tilde{\mathbf{x}}_{k k} = \mathbf{K}_k (\mathbf{z}_k - \mathbf{z}_{k k-1})$
2.11	Expand quaternion	${}^i\mathbf{q}_{k k} = {}^i\mathbf{q}_{k k-1} + \Xi({}^i\mathbf{q}_{k k-1}) {}^i\tilde{\mathbf{q}}_{1:3,k k}$
2.12	Normalize quaternion	${}^i\mathbf{q}_{k k} / \ {}^i\mathbf{q}_{k k}\ \rightarrow {}^i\mathbf{q}_{k k}$
2.13	Calculate a posteriori angular rate	${}^s\boldsymbol{\omega}_{s/i,k k} = {}^s\boldsymbol{\omega}_{s/i,k k-1} + {}^s\tilde{\boldsymbol{\omega}}_{s/i,k k}$
2.14	Calculate a posteriori state vector	$\mathbf{x}_{k k} = [{}^i\mathbf{q}_{k k}^T \quad {}^s\boldsymbol{\omega}_{s/i,k k}^T]^T$
2.15	Calculate a posteriori covariance	$\mathbf{P}_{k k} = (\mathbf{I} - \mathbf{K}_k \mathbf{H}_k) \mathbf{P}_{k k-1}$
2.16	Repeat calculations	Go to 1.1 and iterate filter every Δt time step

	PW-Sat2	Preliminary Design Review	
	2016-11-22	Attitude Determination and Control System	
	Phase B		

7.4 ATTITUDE CONTROL

In this chapter mathematical model of magnetorquers for actuation is presented. The B-Dot algorithm with high-pass filter for Detumbling mode is investigated. The control law for spin-stabilization in Sun Pointing mode is discussed. Time cycles for each control mode are presented.

7.4.1 MAGNETORQUERS

In this section, the concept of the magnetorquers for attitude control is presented. The underactuation of the system and scaling of the generated magnetic dipole are discussed.

7.4.1.1 Concept

The iMTQ board consists of 3 perpendicular electromagnetic coils, one along each satellite's body axis. When current is applied to one of them, the magnetic dipole is generated along the coil's axis:

$$^s\mathbf{m}_i = N I S \quad (7.73)$$

where N is the number of windings, I is applied current [A] and S is the cross section area of the coil [m^2]. Above equation refers to the ideal, infinitely long coil. However, the error for real applications is not significant, therefore Eq. 7.73 is commonly used in analysis.

The concept for single loop is presented in the figure below.

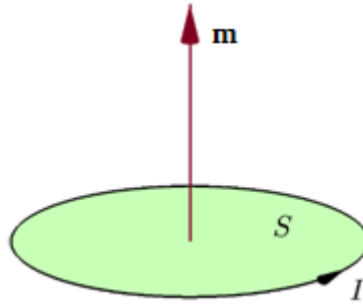




Figure 7-3 Magnetic dipole generated by a single current loop

When current is applied to each perpendicular coil, the 3 dimensional magnetic dipole is generated in space. When magnetic dipole \mathbf{m}_{ctrl} is in magnetic field \mathbf{B} , the torque is generated according to Eq. 7.9:

$$^s\mathbf{T}_{ctrl} = ^s\mathbf{m}_{ctrl} \times ^s\mathbf{B} \quad (7.74)$$

where all vectors are expressed in satellite's body frame and subscript *ctrl* denotes control.

Therefore, when Earth's magnetic field is known in current position, one can calculate the required current in each coil in order to achieve the desired torque based on control law output.

	PW-Sat2	Preliminary Design Review	
	2016-11-22	Attitude Determination and Control System	
	Phase B		

7.4.1.2 Underactuation of the system

The system is *underactuated*, i.e. the arbitrary torque cannot be generated at any time. This is due to the properties of the cross product in Eq. 7.74. Generated torque will be always perpendicular to the current Earth's magnetic field vector. By inspecting the Earth's magnetic field lines, it is possible to predict along which direction the torque cannot be generated for arbitrary part of the orbit. However, the system is fully controllable along whole orbit.

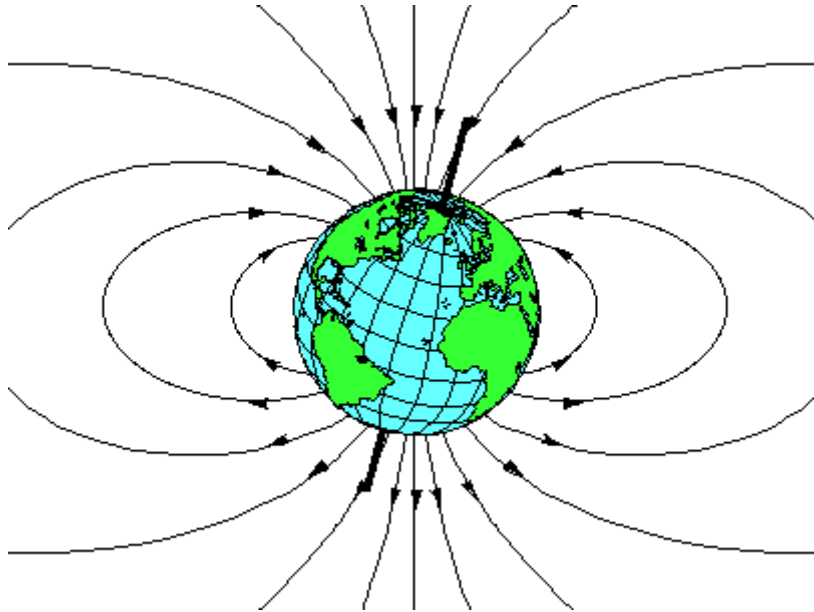


Figure 7-4 Earth's magnetic field

Only the component of commanded torque perpendicular to the Earth's magnetic field vector will be generated. This is presented in the figure below.

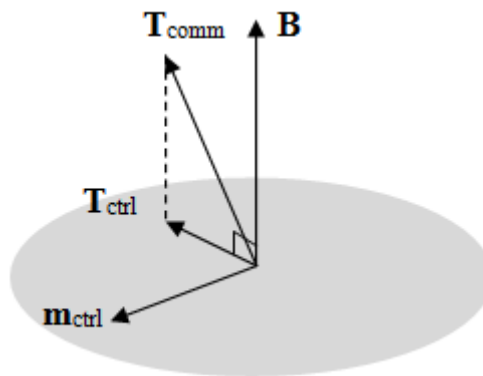




Figure 7-5 Underactuation of the magnetic control system

Given the commanded control torque ${}^S\mathbf{T}_{\text{comm}}$ and Earth's magnetic field ${}^S\mathbf{B}$, the dipole ${}^S\mathbf{m}_{\text{ctrl}}$ which has to be generated in order to create control torque ${}^S\mathbf{T}_{\text{ctrl}}$, can be derived on the basis of Figure 7-5:

	PW-Sat2	Preliminary Design Review	
	2016-11-22	Attitude Determination and Control System	
	Phase B		

$${}^s\mathbf{m}_{ctrl} = \frac{{}^s\mathbf{B} \times {}^s\mathbf{T}_{comm}}{\|{}^s\mathbf{B}\|^2} \quad (7.75)$$

7.4.1.3 Scaling of the dipole

When at least one component of the control dipole ${}^s\mathbf{m}_{ctrl}$ exceeds the nominal value of the magnetic dipole at 5V (see Table 4-1), scaling of the dipole ${}^s\mathbf{m}_{ctrl}$ should take place, so that the direction of the vector is maintained, but the norm of the ${}^s\mathbf{m}_{ctrl}$ vector is reduced. When nominal values of magnetic dipole for X, Y, Z coils are the same and equal $m_{ctrl,@5V}$, then simple algorithm is used (superscripts are omitted for clarity):



1. Find the greatest norm of the components of \mathbf{m}_{ctrl} , $\|\mathbf{m}_{ctrl,max}\|$
2. Check if $\|\mathbf{m}_{ctrl,max}\| > m_{ctrl,@5V}$
3. *If true:* $\mathbf{m}_{ctrl} \cdot m_{ctrl,@5V} / \|\mathbf{m}_{ctrl,max}\| \rightarrow \mathbf{m}_{ctrl}$
If false: don't scale & end

Purchased iMTQ for PW-Sat2, have nominal values of magnetic dipoles for X and Y rods the same and equal $m_{ctrl,XY@5V} = 0.2 \text{ Am}^2$, but nominal value of magnetic dipole for Z aircore is greater and equal $m_{ctrl,Z@5V} = 0.24 \text{ Am}^2$ (see Table 4-1). In this case, the scaling algorithm will be a bit more complex:

1. Find the greatest norm of the components of \mathbf{m}_{ctrl} , $\|\mathbf{m}_{ctrl,max}\|$
2. Check if $\|\mathbf{m}_{ctrl,max}\| > m_{ctrl,XY@5V}$
3. *If false:* don't scale & end
If true: go to 4.
4. Check if $(\|\mathbf{m}_{ctrl,X}\| = \|\mathbf{m}_{ctrl,max}\|) \vee (\|\mathbf{m}_{ctrl,Y}\| = \|\mathbf{m}_{ctrl,max}\|) \vee \{(\|\mathbf{m}_{ctrl,Z}\| \leq m_{ctrl,Z@5V}) \wedge [(\|\mathbf{m}_{ctrl,X}\| > m_{ctrl,XY@5V}) \vee (\|\mathbf{m}_{ctrl,Y}\| > m_{ctrl,XY@5V})]\}$
5. *If true:* find greater value: $\max_{XY} = \max(\|\mathbf{m}_{ctrl,X}\|, \|\mathbf{m}_{ctrl,Y}\|)$
scale: $\mathbf{m}_{ctrl} \cdot m_{ctrl,XY@5V} / \max_{XY} \rightarrow \mathbf{m}_{ctrl}$
If false: $\mathbf{m}_{ctrl} \cdot m_{ctrl,Z@5V} / \|\mathbf{m}_{ctrl,max}\| \rightarrow \mathbf{m}_{ctrl}$
6. Check if $(\|\mathbf{m}_{ctrl,X}\| > m_{ctrl,XY@5V}) \vee (\|\mathbf{m}_{ctrl,Y}\| > m_{ctrl,XY@5V})$
If true: find greater value: $\max_{XY} = \max(\|\mathbf{m}_{ctrl,X}\|, \|\mathbf{m}_{ctrl,Y}\|)$
scale & end: $\mathbf{m}_{ctrl} \cdot m_{ctrl,XY@5V} / \max_{XY} \rightarrow \mathbf{m}_{ctrl}$
If false: don't scale & end

Scaling of the dipole should take place when actuators are working, i.e. both in Detumbling and Sun Pointing modes. PWM will be used to control the input voltage. Magnetorquers work at nominal 5V, therefore in order to generate determined magnetic dipole, the duty cycle of the PWM has to be adjusted. In terms of dynamics of the satellite, the average value of the dipole is considered, therefore this method is sufficient.

Nevertheless, simulations show that commanded magnetic dipole exceeds nominal values only in the initial phases of Detumbling and Sun Pointing modes, when initial errors between current state and commanded state are relatively big. Results are comparable with magnetic dipole being scaled and not, i.e. when commanded

	PW-Sat2	Preliminary Design Review	
	2016-11-22	Attitude Determination and Control System	
	Phase B		

value exceeds the nominal one, coils are saturated and the PWM duty cycle is 100%. Several *if* instructions in scaling algorithm result in much computational load. Therefore, analysis is required in order to determine whether scaling is absolutely necessary. The influence on time of detumbling, Sun pointing error and power consumption should be investigated.

7.4.2 DETUMBLING CONTROL MODE

In Detumbling mode, the B-Dot algorithm is used. In this section, the algorithm is derived and the high-pass filter is presented. Possible time cycles for control sequence are described.

7.4.2.1 The B-Dot Algorithm

The B-Dot is the simplest algorithm used for decelerating the satellite's rotational motion. It is commonly used for detumbling after the P-POD deployment.

In order to reduce the satellite's angular rate ${}^S\omega_{s/i}$, the torque ${}^S\mathbf{T}_{\text{comm}}$ has to be applied:

$${}^S\mathbf{T}_{\text{comm}} = -k \cdot {}^S\omega_{s/i} \quad (7.76)$$

for some positive scalar gain k .

Substituting Eq. 7.76 to Eq. 7.75 for desired magnetic dipole computation:

$${}^S\mathbf{m}_{\text{ctrl}} = k \frac{{}^S\omega_{s/i} \times {}^S\mathbf{B}}{\|{}^S\mathbf{B}\|^2} \quad (7.77)$$

where cross product properties are utilized.

Using general form of Eq. 7.10 for relating the derivative of Earth's magnetic field vector in satellite's body and reference frames, we can write:

$${}^S\mathbf{A} \, {}^i\dot{\mathbf{B}} = {}^S\dot{\mathbf{B}} + {}^S\omega_{s/i} \times {}^S\mathbf{B} \quad (7.78)$$



where ${}^i\dot{\mathbf{B}}$ and ${}^S\dot{\mathbf{B}}$ denote derivatives of the Earth's magnetic field vector calculated in reference and satellite's body frames, respectively. Assuming that the derivative ${}^S\dot{\mathbf{B}}$ is mostly due to the rotational movement, i.e. ${}^i\dot{\mathbf{B}} \ll {}^S\dot{\mathbf{B}}$, we can write ${}^i\dot{\mathbf{B}} \approx 0$. This approximation is valid in initial phase of detumbling. Therefore, Eq. 7.78 can be written:

$${}^S\dot{\mathbf{B}} \approx -{}^S\omega_{s/i} \times {}^S\mathbf{B} \quad (7.79)$$

Substituting Eq. 7.79 into Eq. 7.77:

$${}^S\mathbf{m}_{\text{ctrl}} = -k \frac{{}^S\mathbf{B}}{\|{}^S\mathbf{B}\|^2} \quad (7.80)$$

Control gain k can be expressed as [1]:

	PW-Sat2	Preliminary Design Review	
	2016-11-22	Attitude Determination and Control System	
	Phase B		

$$k = \frac{4\pi}{T_{orb}} (1 + \sin\xi) I_{min} \quad (7.81)$$

where T_{orb} is the orbital period [s], I_{min} is the minimum principal moment of inertia and ξ is the inclination of satellite's orbit relative to the geomagnetic equatorial plane.

In the simulations, the inclination of the geomagnetic equatorial plane relative to the Earth's equatorial plane was assumed 10° . After performing some simulations, Eq. 7.81 for control gain k was optimized empirically:

$$k_{opt} = \frac{6\pi}{T_{orb}} [1 + \sin(i - 10^\circ)] I_{min} \quad (7.82)$$

where i denotes orbit's inclination in [deg].

The B-Dot gain k can be optimized in real time based on different formulation. However, constant gain in Eq. 7.82 gives satisfactory results, therefore, its adaptation is not considered.

7.4.2.2 High-pass Filter for B-Dot computation

In B-Dot algorithm, the derivative of Earth's magnetic field is computed (see Eq. 7.80). The discrete derivative in i -th time step can be computed as:

$$s\dot{\mathbf{B}}_i = \frac{s\mathbf{B}_i - s\mathbf{B}_{i-1}}{\Delta t} \quad (7.83)$$

where $s\mathbf{B}_i$ and $s\mathbf{B}_{i-1}$ are two subsequent magnetometer's measurements and Δt is sampling time.

Due to the satellite's rotational motion, vectors $s\mathbf{B}_i$ and $s\mathbf{B}_{i-1}$ are expressed in different coordinate frames –the satellite's body frame in i -th time step is rotated relatively to the satellite's body frame in $i-1$ –th time step. However, when sampling time Δt is small, this difference can be neglected.

In general, calculating the derivative of noisy data according to Eq. 7.83 is not accurate. The high-pass filter concept is proposed according to [3].

Continuous filter estimates the derivative of Earth's magnetic field at time t based on the Earth's magnetic field measurement taken at the same time instant t . The continuous filter can be described as:

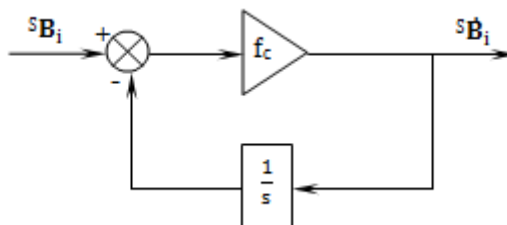




Figure 7-6 Continous filter for input's derivative estimation

where f_c is cut-off frequency.

	PW-Sat2	Preliminary Design Review	
	2016-11-22	Attitude Determination and Control System	
	Phase B		

The transfer function for above diagram block is:

$$\frac{Y(s)}{X(s)} = \frac{f_c}{1 + f_c s^{-1}} \quad (7.84)$$

where Y and X denote system's output and input, respectively.

Discrete equivalent of Eq. 7.84 is calculated by taking the Z-transform of Eq. 7.84 or using `c2d` Matlab function:

$$\frac{Y(z)}{X(z)} = \frac{f_c - f_c z^{-1}}{1 - e^{-f_c \Delta t} z^{-1}} \quad (7.85)$$

Multiplying and rearranging terms of Eq. 7.85:

$$Y(z) = e^{-f_c \Delta t} Y(z) z^{-1} + f_c [X(z) - X(z) z^{-1}] \quad (7.86)$$

According to the time-shift property of the Z-transform:

$$x[n - k] = X(z) z^{-k} \quad (7.87)$$

Substituting $k=1$ in Eq. 7.87 and calculating the inverse Z-transform of Eq. 7.86:

$$s\dot{\mathbf{B}}_i = e^{-f_c \Delta t} s\dot{\mathbf{B}}_{i-1} + f_c (s\mathbf{B}_i - s\mathbf{B}_{i-1}) \quad (7.88)$$

Eq. 7.88 can be identified with the general formulation of the high-pass filter. With decreasing the value of f_c , current output is more dependent on the previous output. Therefore, the influence of the measurement's noise is reduced.



The sample time Δt for Detumbling mode is determined to be equal 0.2 s. Cut-off frequency f_c has been established empirically to be equal 0.2 [Hz] according to the set of simulations.

Utilizing the high-pass filter in derivative of Earth's magnetic field computation decreases noise in the output especially in the initial phases of detumbling. This is due to the passing of higher frequencies by the filter, i.e. when the changes of inputs are greater. Changes of inputs are greater for higher angular rates which takes place in initial phase of detumbling. The B-Dot algorithm is robust for noise and even without filtration of inputs, the time of detumbling is approximately 1 orbit and is the same as for high-pass filter included. However, with turning the high-pass filter on, power consumption is reduced approximately 10 times. Therefore, it has to be used in B-dot algorithm onboard.

Simulation results of B-Dot algorithm with and without high-pass filter are presented in chapter 8.3.2.

7.4.2.3 Time cycle for Detumbling mode

In the figure below, the possible time cycle for Detumbling mode is presented. It is assumed that the constant magnetic dipole is generated for 80% of the cycle's period. Some of these values may change in the future.

	PW-Sat2	Preliminary Design Review	
	2016-11-22	Attitude Determination and Control System	
	Phase B		

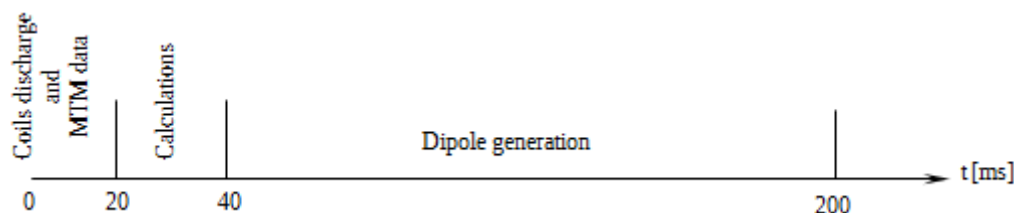


Figure 7-7 Time cycle for Detumbling mode



It can be seen that in real time applications, the dipole is generated on the basis of the measurements from the past, therefore not precisely valid at the moment of dipole generation. However, the delay of approximately 40 ms should not influence the time of detumbling. The error depends on the satellite's angular rate, however, rotation greater than 20°/s on each axis is not expected after P-POD deployment. After 40 ms, the satellite will be rotated at 0.8° around each axis for this angular rate. Thus the delay error is neglectable.

7.4.3 SUN POINTING CONTROL MODE

In Sun Pointing mode, spin stabilization is used in order to make the direction of rotation axis less sensitive to disturbance torques. In this section, the control law and the time cycle for Sun Pointing mode are presented.

7.4.3.1 Sun Pointing Algorithm

As previously stated, the PD controller with the magnetorquers is not able to stabilize the attitude of the satellite in ECI inertial frame, i.e. keeping it fixed. Due to the disturbance torques, the Sun pointing errors in some cases are as great as 50°. With utilizing the gyroscopic effect, the Sun pointing error can be reduced to 2° according to the simulations results. By spinning the satellite's around its X axis and controlling its direction so that it points towards the Sun, the deployed solar panels' plane is perpendicular to the Sun direction. The concept is presented in the figure below.

	PW-Sat2	Preliminary Design Review	
	2016-11-22	Attitude Determination and Control System	
	Phase B		

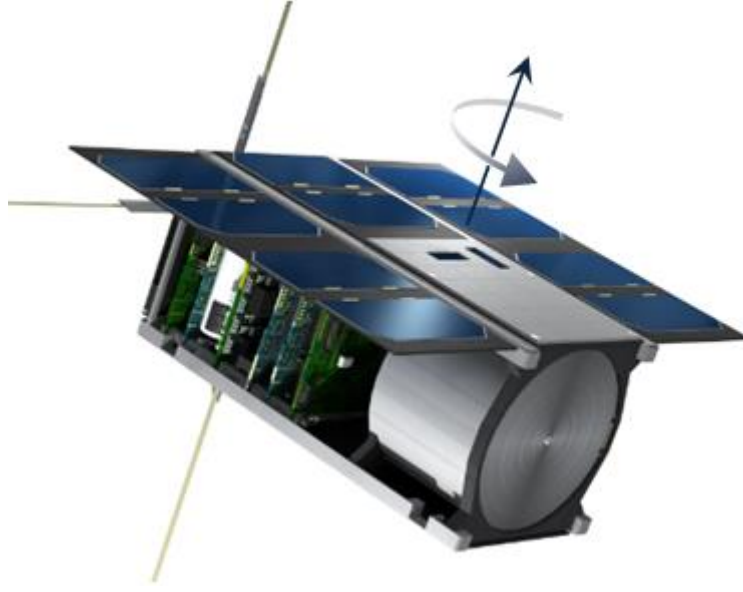


Figure 7-8 Spin stabilization around the satellite's X axis

The control law for spin stabilization in [4] was modified in order to account for Sun Pointing:

$${}^s\mathbf{T}_{\text{comm}} = k_K {}^s\tilde{\mathbf{h}} + k_p e_{h,x} \begin{bmatrix} 1 \\ 0 \\ 0 \end{bmatrix} + k_n \underline{\mathbf{D}} {}^s\boldsymbol{\omega}_{s/i} \quad (7.89)$$



where

$${}^s\tilde{\mathbf{h}} = {}^s\mathbf{h}_{\text{comm}} - {}^s\mathbf{h} = \underline{\mathbf{I}} ({}^s\underline{\mathbf{A}} {}^i\mathbf{e}_{\oplus\odot} \| {}^s\boldsymbol{\omega}_{s/i,\text{comm}} \| - {}^s\boldsymbol{\omega}_{s/i}) \quad (7.90a)$$

$$e_{h,x} = {}^s\mathbf{h}_{\text{comm}} - {}^s\mathbf{h}_x = I_{xx} \| {}^s\boldsymbol{\omega}_{s/i,\text{comm}} \| - I_{xx} {}^s\omega_{s/i,x} \quad (7.90b)$$

Below the description of each term in Eqs. 7.89 and 7.90 is presented.

${}^s\tilde{\mathbf{h}}$	error between satellite's commanded and current angular momentum vector expressed in satellite's body frame
${}^s\mathbf{h}_{\text{comm}}$	commanded satellite's angular momentum vector expressed in satellite's body frame
${}^s\mathbf{h}$	current satellite's angular momentum vector expressed in satellite's body frame
$\underline{\mathbf{I}}$	inertia matrix calculated in satellite's body frame
${}^s\underline{\mathbf{A}}$	transformation matrix from ECI inertial frame to satellite's body frame
${}^i\mathbf{e}_{\oplus\odot}$	Sun vector expressed in ECI inertial frame according to Eq. 6.6
${}^s\boldsymbol{\omega}_{s/i,\text{comm}}$	commanded satellite's angular rate relative to ECI inertial frame expressed in satellite's body frame
${}^s\boldsymbol{\omega}_{s/i}$	current satellite's angular rate expressed in satellite's body frame

	PW-Sat2	Preliminary Design Review	
	2016-11-22	Attitude Determination and Control System	
	Phase B		

$e_{h,x}$ error between satellite's commanded and current angular momentum component along satellite's X axis expressed in satellite's body frame

$^s h_{comm}$ norm of commanded satellite's angular momentum vector; it is the norm of vector $^s \mathbf{h}_{comm}$

$^s h_x$ X component of current satellite's angular momentum vector expressed in satellite's body frame, assuming products of inertia equal 0

$^s \omega_{s/i,x}$ X component of current satellite's angular rate expressed in satellite's body frame

$\underline{\mathbf{D}}$ selection matrix, $\underline{\mathbf{D}} = \text{diag}(0,1,1)$

k_K angular momentum gain

k_p precession damping gain

k_n nutation damping gain

Based on set of simulations, control gains was chosen empirically, so that:

$$k_K = 4 \cdot 10^{-3}, k_p = 4 \cdot 10^{-3}, k_n = -10^{-4}$$

Satellite's commanded angular rate is defined in the satellite's body frame:

$$^s \omega_{s/i,comm} = [5 \quad 0 \quad 0]^T \text{ } ^\circ/\text{s}$$



and was determined empirically, on the basis of simulations.

When the satellite reaches its commanded state, the direction of the angular rate vector will coincide with the Sun direction. Therefore, the commanded satellite's angular rate expressed in ECI inertial frame can be written as:

$$^i \omega_{s/i,comm} = ^i \mathbf{e}_{\odot} \| ^s \omega_{s/i,comm} \| \quad (7.91)$$

It is crucial that the moment of inertia around X axis in the satellite's body frame, I_{xx} , is the largest one. The rotational motion is stable only if the body spins around the largest or the smallest principal axis of inertia [1]. For PW-Sat2, the products of inertia are negligible, therefore, the satellite's body frame can be treated as the principal frame. If the body spins around its intermediate axis of inertia, the motion will be unstable. According to PW-Sat2 current CAD model, moments of inertia around satellite's X and Y axes are nearly equal (see the Preliminary Design Review of CONF team), even when the solar panels are deployed. However, the PW-Sat2 CAD model is not yet finished and not all elements are included.

Nevertheless, care must be taken when distributing elements inside the satellite, both in CAD software and in real satellite's configuration sequence. According to the simulation results presented in chapter 8.3 it is recommended, that the ratio between the moments of inertia around X and Y axes is not smaller than 1.1, giving the safety range for differences between modelled and real mass distribution:

	PW-Sat2	Preliminary Design Review	
	2016-11-22	Attitude Determination and Control System	
	Phase B		

$$I_{xx}/I_{yy} \geq 1.1$$

7.4.3.2 Time cycle for Sun Pointing mode

In the figure below, the possible time cycle for Sun Pointing mode is presented. It is assumed that the constant magnetic dipole is generated for 80% of the cycle's period. Some of these values may change in the future.

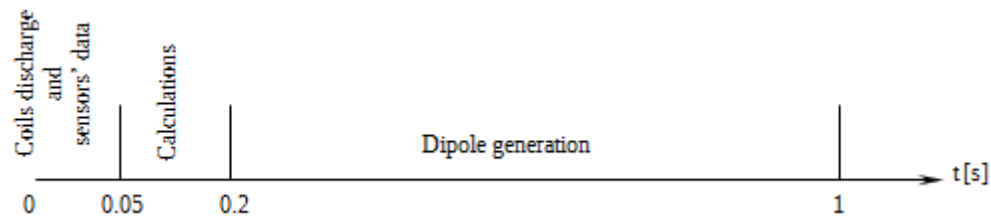




Figure 7-9 Time cycle for Sun Pointing mode

According to the discussion in chapter 7.4.2.3 about the measurements' delay, similar calculations are performed for Sun Pointing mode.

With the nominal angular rate about the satellite's X axis equal 5°/s, the satellite will be rotated at 1° after 0.2 s. Similarly to Detumbling mode, the delay error is negligible in Sun Pointing mode.

In eclipse, magnetorquers are off in Sun Pointing mode. The simulations have proven that the angular rate of 5°/s is sufficient enough to make the rotation axis passively stable with no actuation. However, in eclipse the Sun pointing error slowly grows with time, therefore after going out from eclipse, magnetorquers are turned on.

	PW-Sat2	Preliminary Design Review	
	2016-11-22	Attitude Determination and Control System	
	Phase B		

8 SIMULATION SOFTWARE

Simulation software was developed to verify the proposed ADCS algorithms. In this chapter the block diagram of the simulation is presented. Next, the mathematical models of the sensors are discussed. This is followed by input parameters description. Then, results for set of simulations both for Detumbling and Sun Pointing mode are presented. Many variations of input parameters are chosen to test the performance of the ADCS.

8.1 OVERVIEW

The software was developed in MatLab environment. For orbit propagation, simple J2 propagator was chosen. IGRF11 10th order is chosen for Earth's magnetic field simulation and IGRF11 9th order is chosen for reference Earth's magnetic field model. In real application, IGRF11 13th order will be loaded into the satellite's OBC memory. The accuracy of the 13th order is approximately 20nT not considering magnetic storms. Therefore, lower order is chosen for attitude determination in order to simulate the differences between the reference and "truth" model. The figure below presents the error between 10th and 9th IGRF11 order calculated in ECI inertial frame for 2 circular SSO orbits with altitude 600 km.

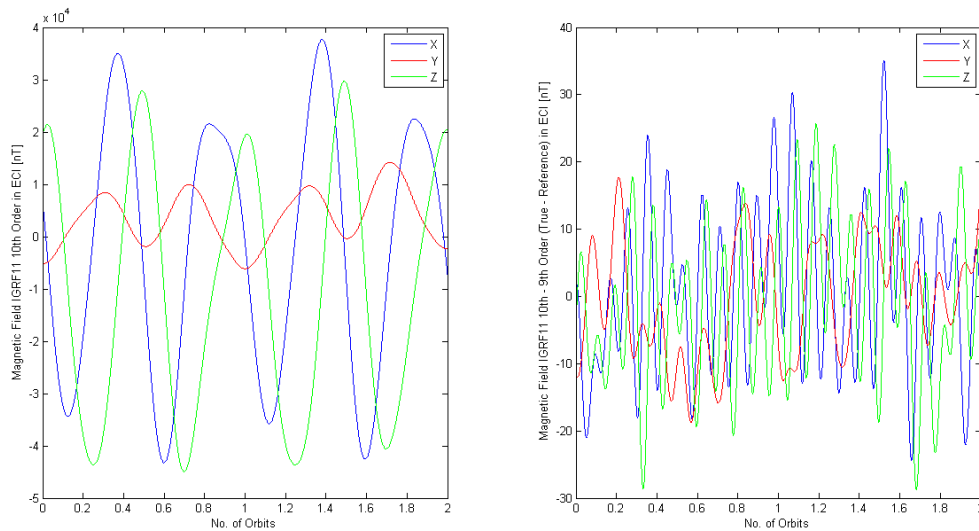




Figure 8-1 Earth's magnetic field in ECI (left), Error between IGRF11 10th and 9th order in ECI (right)

The maximum error between IGRF11 10th and 9th order is approximately 35 nT. It is a bit greater than the error between true and 13th order, nevertheless it is very similar and can be used in simulations.

The orbit is propagated using J2 orbital parameters perturbation equations [1]. This model only accounts for perturbation generated by the non-spherical shape of the Earth. However, only second order harmonic expansion

	PW-Sat2	Preliminary Design Review	
	2016-11-22	Attitude Determination and Control System	
	Phase B		

is used. In the figures below, satellite's position and velocity vectors in ECI inertial frame are presented. They were generated using J2 orbit propagator for SSO orbit with altitude 600 km.

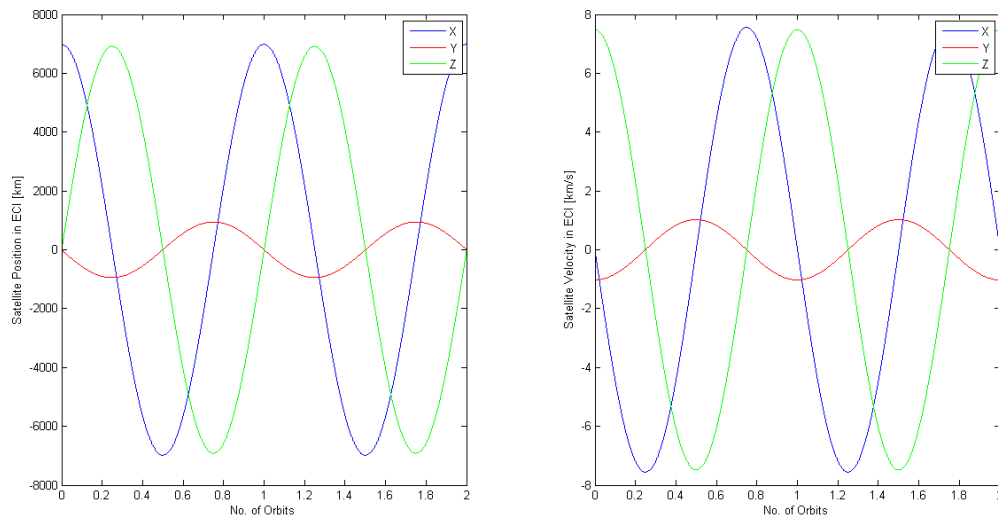


Figure 8-2 Satellite's position and velocity in ECI based on J2 orbit propagator

Satellite's attitude dynamics and kinematics is simulated using equations presented in chapter 7.2. True satellite's attitude and angular rate are integrated using Runge-Kutta 4th order integration with variable step. MatLab's `ode45` function is used. After each iteration, true attitude quaternion is normalized. Disturbance torques are calculated for "true" parameters using equations presented in chapter 7.1.

When the satellite is in eclipse, Sun Sensor outputs are equal 0. Magnetorquers are off and there is no solar radiation pressure torque. The condition for eclipse is calculated according to the cylindrical shade model. Generally it doesn't account for partial shading called *penumbra*. Therefore, the Earth's radius is extended for 20 km. The value was calculated based on simple geometrical model.

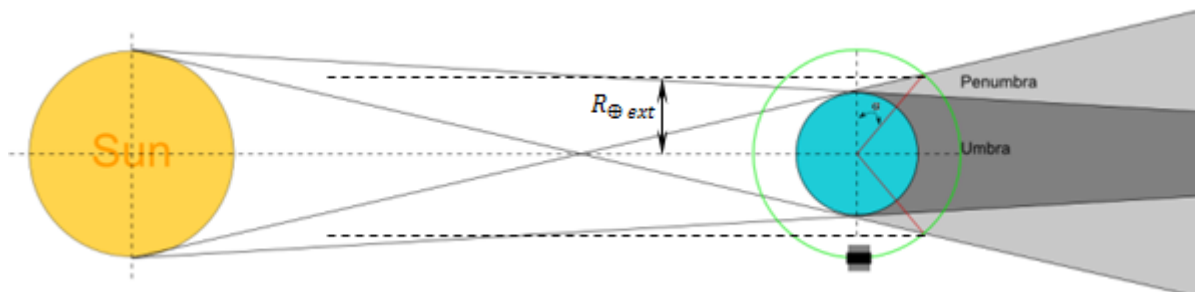




Figure 8-3 Eclipse condition

It can be seen from the figure above, that the satellite is in eclipse if and only if:

	PW-Sat2	Preliminary Design Review	
	2016-11-22	Attitude Determination and Control System	
	Phase B		

$$\mathbf{r} \circ \mathbf{e}_{\oplus\odot} < -\sqrt{\|\mathbf{r}\|^2 - R_{\oplus ext}^2} \quad (8.1)$$

where \mathbf{r} is the satellite's position vector and $\mathbf{e}_{\oplus\odot}$ is Earth to Sun unit vector calculated using Eq. 6.6. Both vectors are expressed in ECI inertial frame. The Earth's shape is a sphere.

On the next page, the block diagram of the simulation is presented.

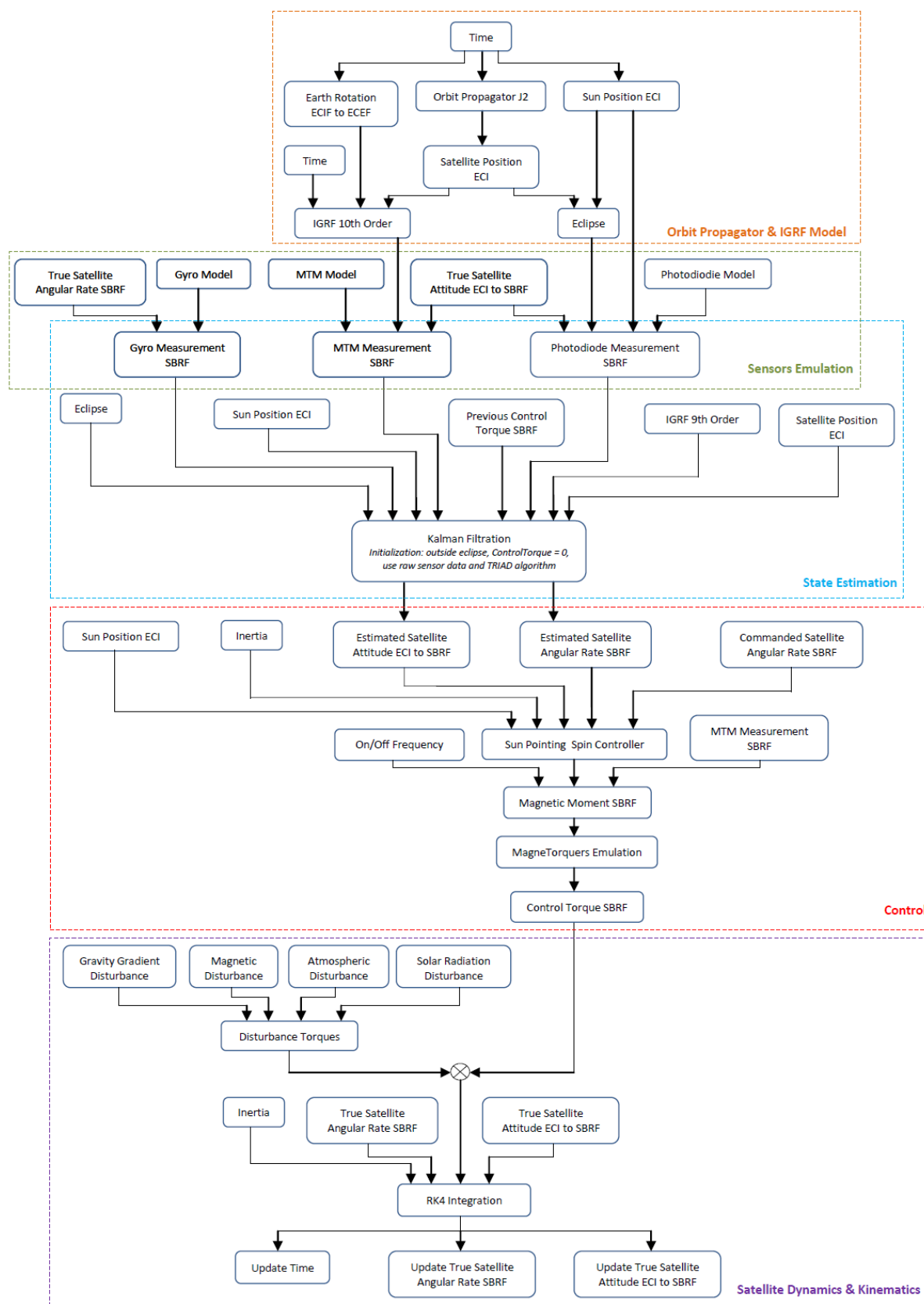




Figure 8-4 Simulation software block diagram for Sun Pointing mode

	PW-Sat2	Preliminary Design Review	
	2016-11-22	Attitude Determination and Control System	
	Phase B		

8.2 SENSORS' MODEL

Sensors' outputs are calculated using “true” values and the mathematical model of errors.

The general formulation for continuous 3 axial sensor's output model accounting for white noise, drift, scale factors and misalignments errors is [1]:

$$\mathbf{a}(t) = (\mathbf{1}_{3 \times 3} + \mathbf{S}^{\text{true}})\mathbf{a}^{\text{true}}(t) + \mathbf{b}^{\text{true}}(t) + \mathbf{w}_v(t) \quad (8.2a)$$

$$\dot{\mathbf{b}}^{\text{true}}(t) = \mathbf{w}_u(t) \quad (8.2b)$$

where \mathbf{a} is measured output, \mathbf{a}^{true} is the true value, \mathbf{b}^{true} is true bias, \mathbf{S}^{true} is the true matrix containing scale factors and misalignments errors, \mathbf{w}_v and \mathbf{w}_u are independent, uncorrelated zero-mean Gaussian white-noise processes with covariances:

$$\mathbb{E}\{\mathbf{w}_v(t)\mathbf{w}_v^T(\tau)\} = \sigma_v^2\delta(t - \tau)\mathbf{1}_{3 \times 3}$$

$$\mathbb{E}\{\mathbf{w}_u(t)\mathbf{w}_u^T(\tau)\} = \sigma_u^2\delta(t - \tau)\mathbf{1}_{3 \times 3}$$

where \mathbb{E} denotes expected value, and $\delta(t - \tau)$ is the Dirac delta function defined as [1]:

$$\delta(t - \tau) = 0 \text{ for } t \neq \tau$$

$$\int_{-\infty}^{\infty} \delta(t - \tau) d\tau = 1$$

The discrete model equivalent of Eq. 8.2 is [1]:



$$\mathbf{a}_{k+1} = (\mathbf{1}_{3 \times 3} + \mathbf{S}^{\text{true}})\mathbf{a}_{k+1}^{\text{true}} + \frac{1}{2}(\mathbf{b}_{k+1}^{\text{true}} + \mathbf{b}_k^{\text{true}}) + \left(\frac{\sigma_v^2}{\Delta t} + \frac{1}{12}\sigma_u^2\Delta t\right)^{1/2}\mathbf{N}_{v,k} \quad (8.3a)$$

$$\mathbf{b}_{k+1}^{\text{true}} = \mathbf{b}_k^{\text{true}} + \sigma_u\Delta t^{1/2}\mathbf{N}_{u,k} \quad (8.3b)$$

where Δt is the time step, k denotes the k -th time instant and $\mathbf{N}_{v,k}$ and $\mathbf{N}_{u,k}$ are zero-mean Gaussian white-noise processes with identity matrix covariances.

In the simulation software, the drift is included only in the gyroscope measurements. Therefore, for magnetometer and Sun sensor, $\sigma_u = 0$. For magnetometer and Sun sensor, constant biases are incorporated.

The zero-mean Gaussian process was simulated using MatLab's `randn` function.

	PW-Sat2	Preliminary Design Review	
	2016-11-22	Attitude Determination and Control System	
	Phase B		



8.3 SIMULATIONS RESULTS

Nine simulations were performed with various input parameters in order to test the performance and the robustness of the ADCS and to estimate the expected accuracy.

In the table below, input parameters constant for each simulation are presented.

Table 8-1 Simulation's constant input parameters

Parameter	Value	Unit
Time:		
GMT time: 15.02.2014, 12:00	-	-
iteration time for Sun Pointing mode	1	s
iteration time for Detumbling mode	0.2	s
Satellite		
satellite's center of mass wrt geometrical center: X, Y, Z	0.05, -0.04, 0.03	m
diagonal elements of inertia matrix: I_{xx} , I_{yy} , I_{zz}	12356, 11097, 4432	kgmm ²
off-diagonal elements of inertia matrix: I_{xy} , I_{xz} , I_{yz}	16, -16, 42	kgmm ²
Sun Synchronous Orbit:		
altitude	600	km
eccentricity	0	-
initial RAAN	0	deg
initial argument of perigee	0	deg
initial mean anomaly	0	deg
Initial Attitude & Angular Rate (SBRF wrt ECI):		
yaw, pitch, roll	75, 10, -25	deg
initial angular rate for Sun Pointing mode (X, Y, Z)	0.2, -0.1, 0.15	deg/s
initial angular rate for Detumbling mode (X, Y, Z)	10, 10, 10	deg/s
Magnetorquers:		
nominal magnetic dipole for X, Y rods	0.2	Am ²
nominal magnetic dipole for Z aircore	0.24	Am ²
power consumption for X, Y rods	1.1	W/Am ²
power consumption for Z aircore	2.9	W/Am ²
time on within the cycle	80	%
Environment:		
IGRF11 order for true model	10th	-
IGRF11 order for reference model	9th	-
atmospheric drag coefficient	2.2	-
solar constant	1363	W/m ²
Sensors:		
gyro noise (rms)	0.5	deg/ \sqrt{s}
gyro constant bias	0	deg/s
magnetometer noise (rms)	150	nT $\cdot\sqrt{s}$
Sun sensor noise (rms)	6	deg $\cdot\sqrt{s}$
scale factors & misalignments (rms)	0.02	-

	PW-Sat2	Preliminary Design Review	
	2016-11-22	Attitude Determination and Control System	
	Phase B		

8.3.1 SUN POINTING MODE

In the table below, parameters which are variable in 6 simulations for Sun Pointing mode are presented:

Table 8-2 Variable simulation's parameters for Sun Pointing mode

Condition	Sim. 1	Sim. 2	Sim. 3	Sim. 4	Sim. 5	Sim. 6
MTM bias (X, Y, Z) : 800, 700, -650 [nT]	-	+	-	-	-	+
Sun Sensor unit vector bias (X, Y, Z) : 0.02, -0.02, 0.03 [-]	-	+	-	-	-	+
Gyro drift, $\sigma_u = 0.005 \text{ [deg}/\sqrt{s^3}]$	-	-	+	-	-	+
Inertia error: each ref. Inertia matrix element is 20% smaller than “true”	-	-	-	+	-	+
Y magnetorquer rod off	-	-	-	-	+	+

When constant biases and drift are added on measurements, the Kalman filter formulation doesn't change. Therefore, simulations 2 & 3 show the influence of not modelled sensors' errors on the ADCS performance.



Satellite's inertia matrix will have to be loaded into OBC memory. It is used in MEKF state propagation and in Sun Pointing control law. However, it will be calculated on the basis of the satellite's CAD model. The masses of elements inside the satellite are calculated as point masses, thus the mass distribution is not accommodated accurately. Treating the objects like point masses results in lower inertia matrix. The influence of inertia matrix error is verified in Simulation 4.

Simulation 5 tests the Sun Pointing mode performance during one coil malfunction. It is assumed that the magnetorquer's malfunction can be detected and the failure coil can be turned off.

Simulation 1 is the best case scenario, with no biases and drift on measurements, assuming perfect knowledge of the satellite's inertia matrix and with all magnetorquers working.

Simulation 6 is the worst case scenario, with gyro drift, Sun sensor and magnetometer biases, inertia matrix error and one magnetorquer malfunction. Worst case scenario refers to the situation when ADCS is still able to track the Sun with predetermined accuracy. For instance, when 2 coils are not working, the 1 remaining coil is not able to stabilize the satellite towards the Sun. Therefore, this case is not shown.

On the figures below, the results for each simulation are presented.

	PW-Sat2	Preliminary Design Review	
	2016-11-22	Attitude Determination and Control System	
	Phase B		

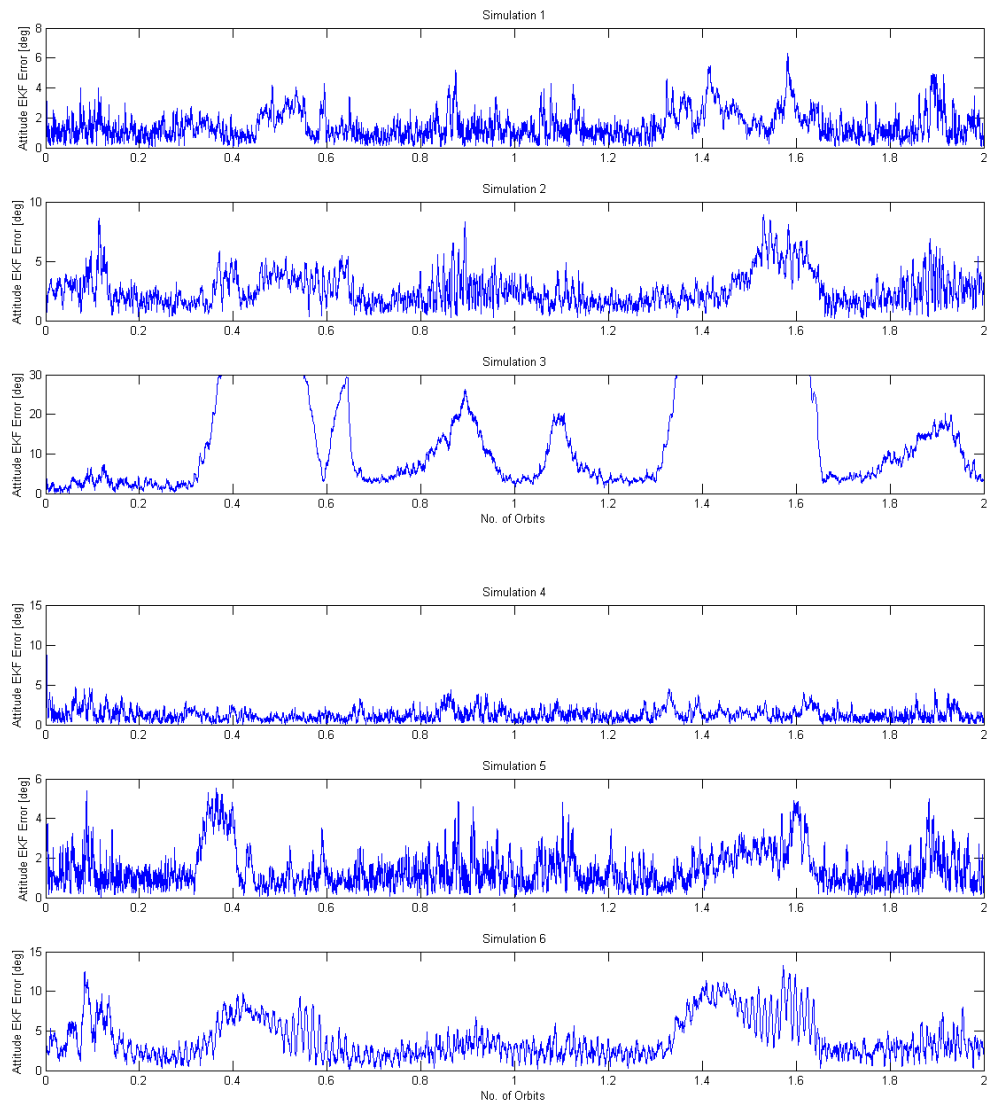




Figure 8-5 Satellite's attitude error between true and estimated (small rotation vector norm) in Sun Pointing mode

	PW-Sat2	Preliminary Design Review	
	2016-11-22	Attitude Determination and Control System	
	Phase B		

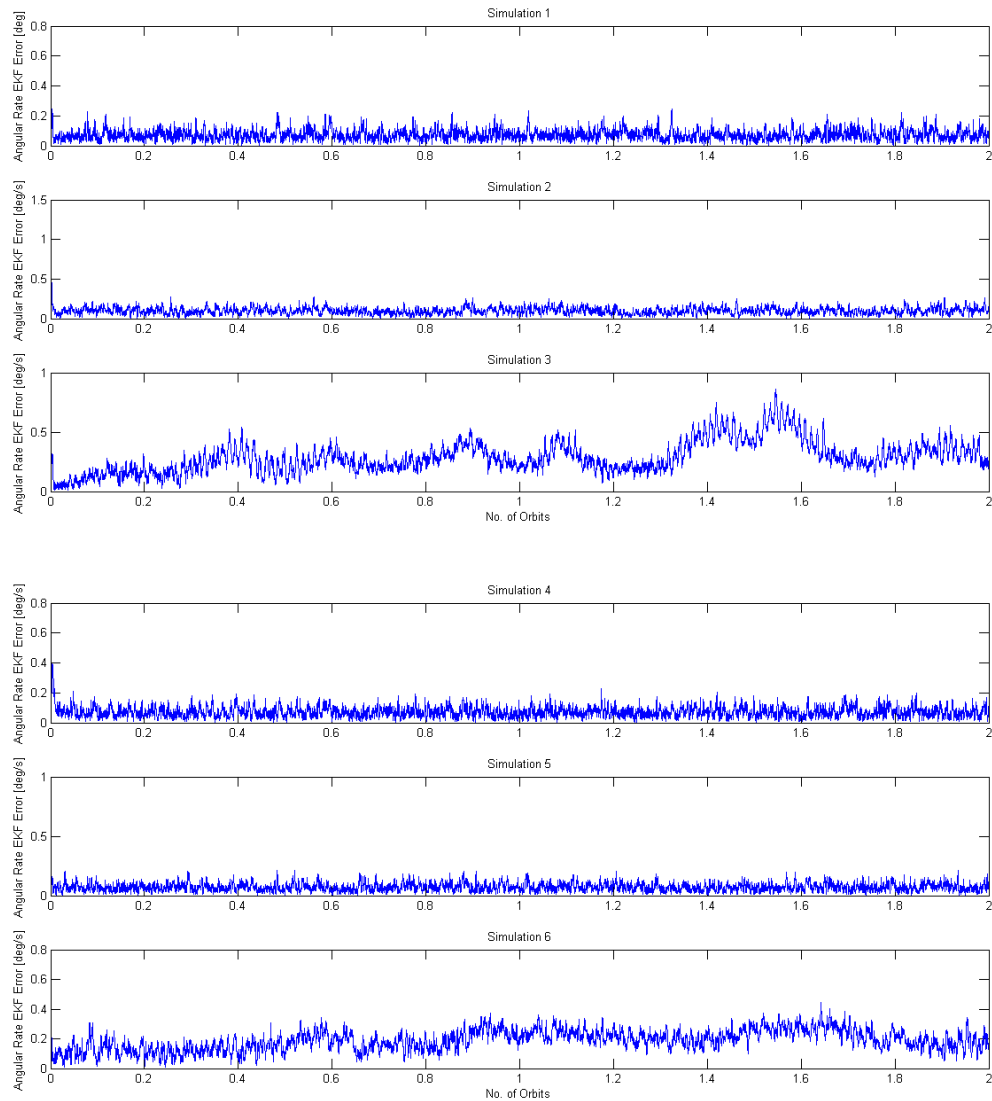


Figure 8-6 Satellite's angular rate error between true and estimated (vector norm) in Sun Pointing mode

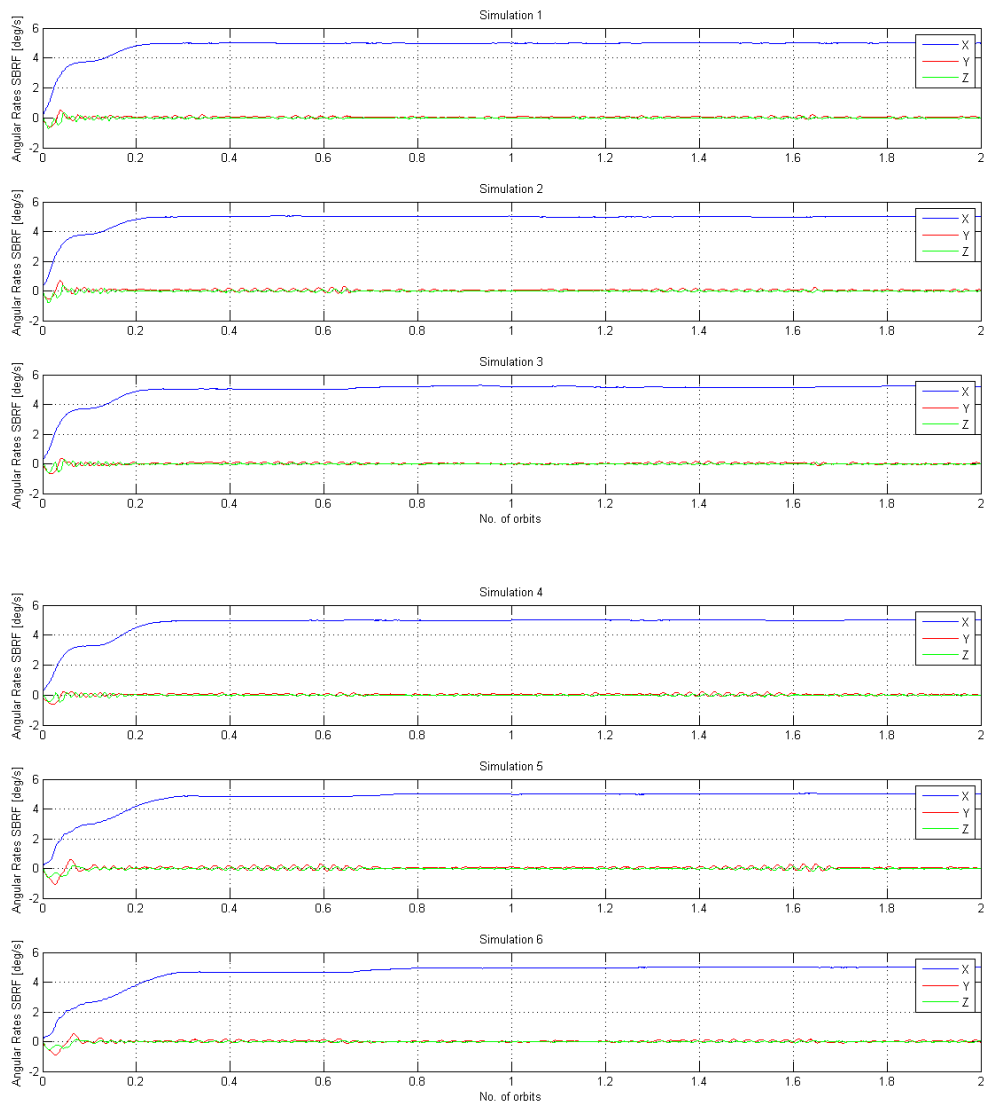




Figure 8-7 Satellite's angular rate in SBRF for control inputs based on EKF in Sun Pointing mode

	PW-Sat2	Preliminary Design Review	
	2016-11-22	Attitude Determination and Control System	
	Phase B		

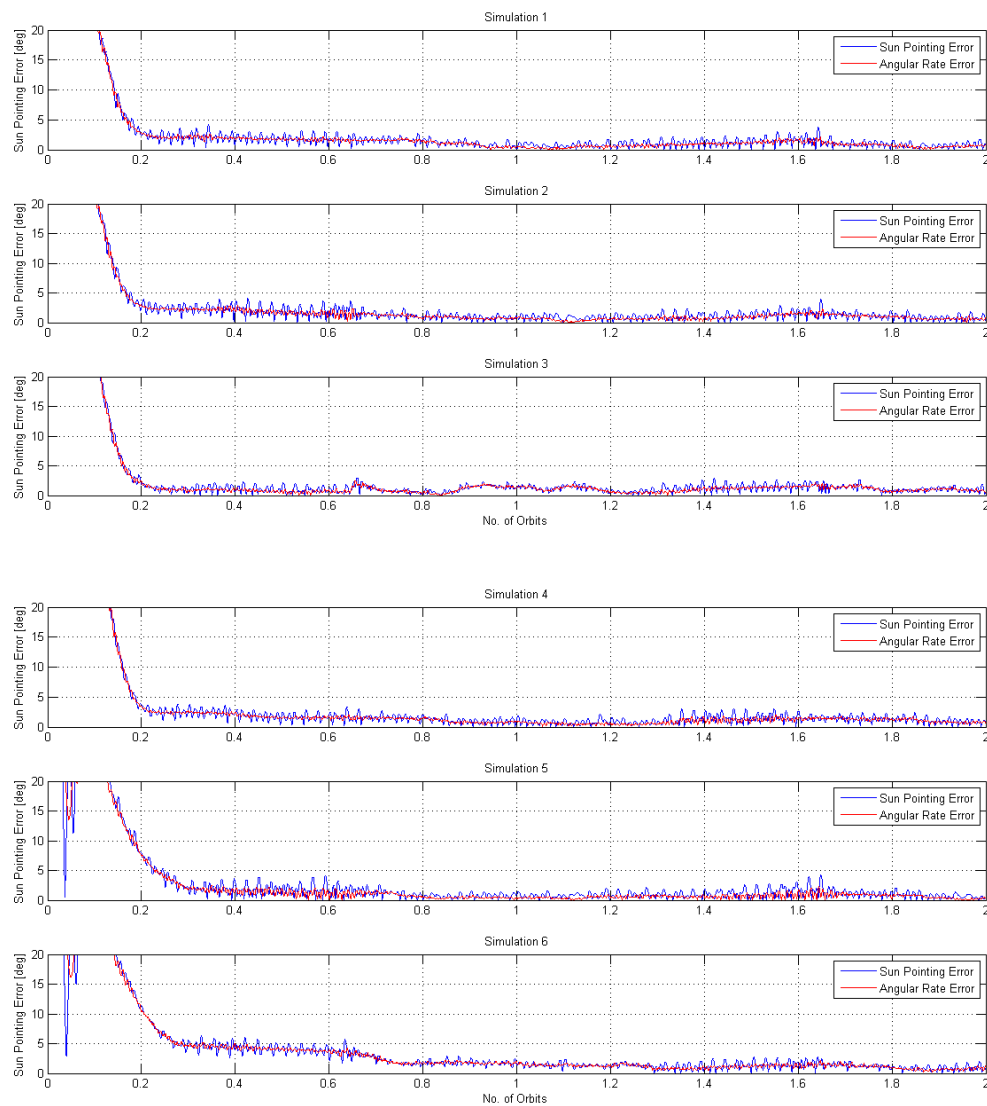




Figure 8-8 Error between satellite's X axis, angular rate vector and Sun direction in Sun Pointing mode

	PW-Sat2	Preliminary Design Review	
	2016-11-22	Attitude Determination and Control System	
	Phase B		

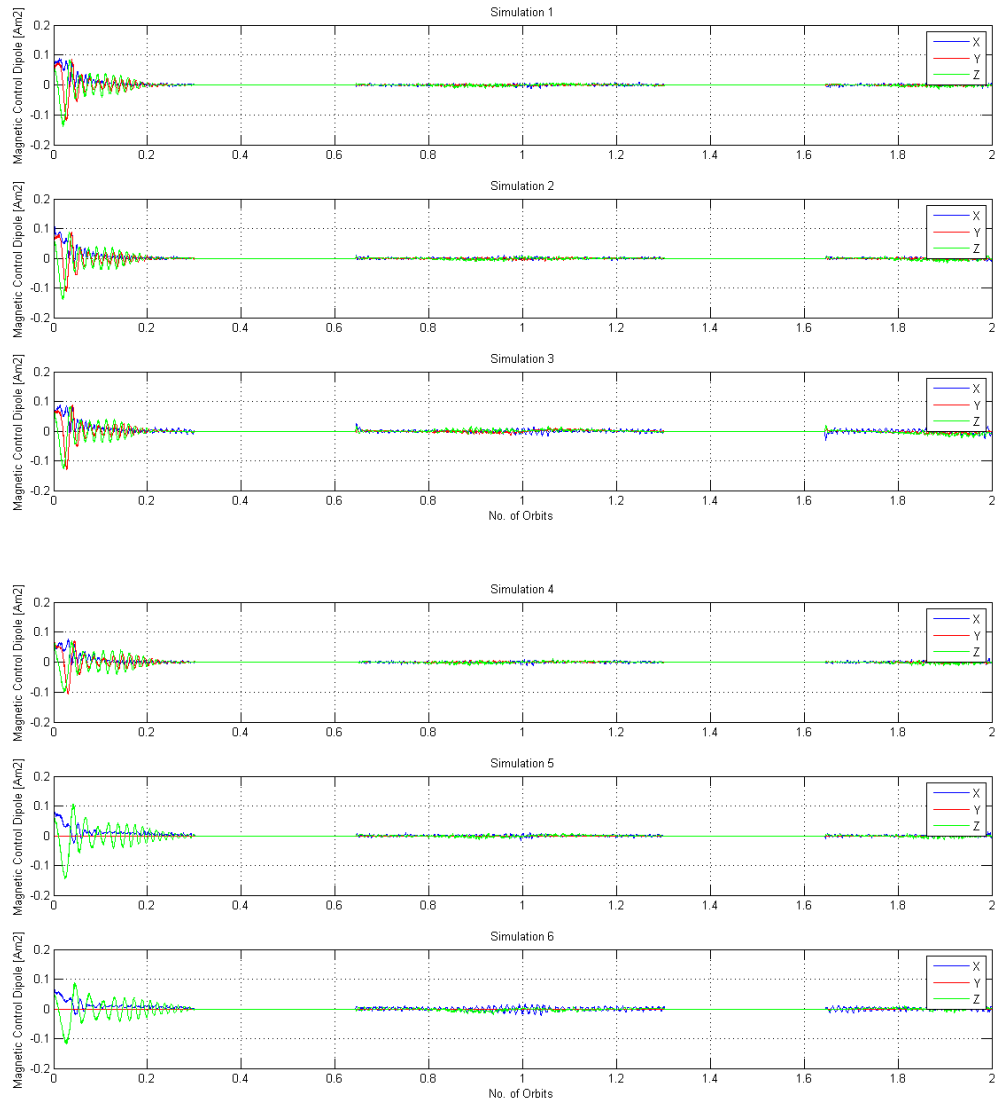




Figure 8-9 Magnetic control dipole (0 in eclipse) in Sun Pointing mode

	PW-Sat2	Preliminary Design Review	
	2016-11-22	Attitude Determination and Control System	
	Phase B		

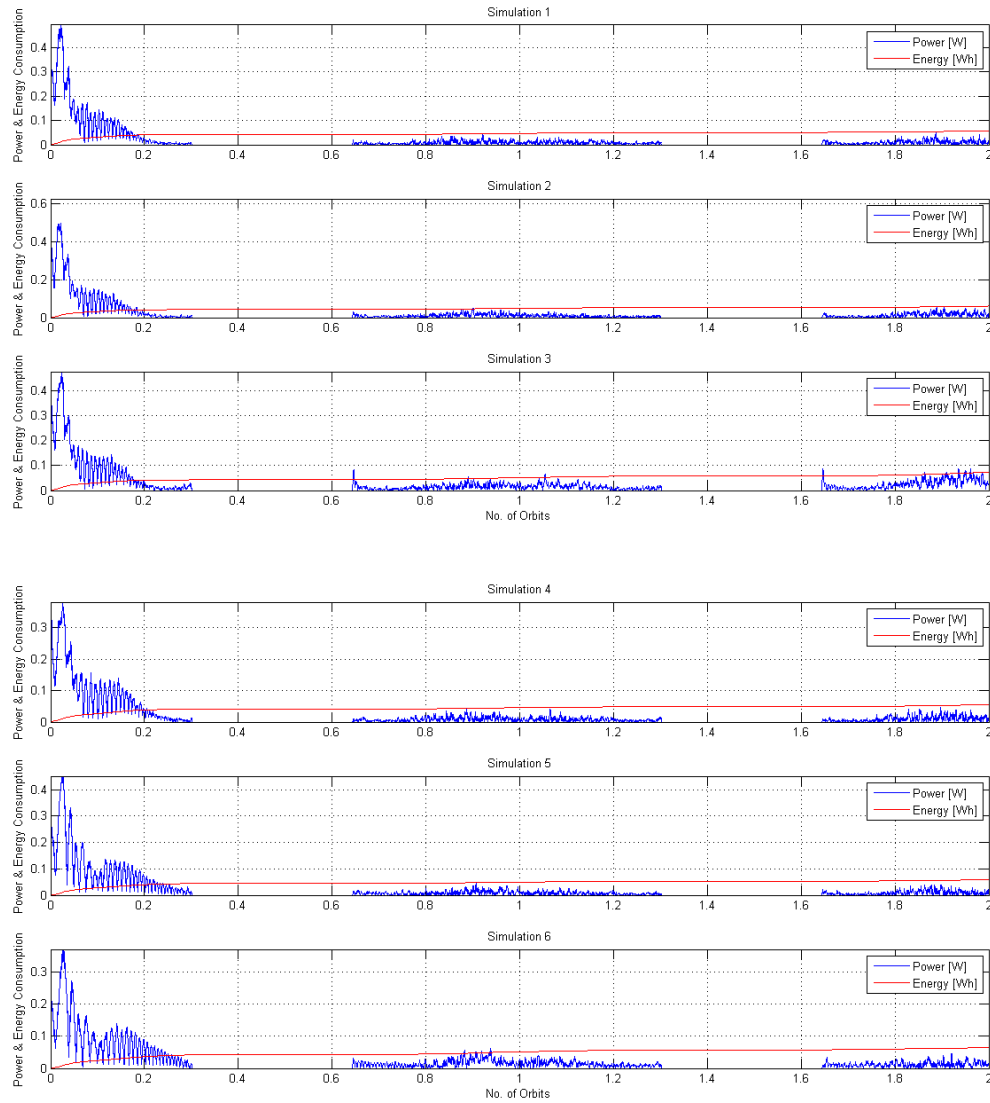




Figure 8-10 Power & Energy consumption in Sun Pointing mode

	PW-Sat2	Preliminary Design Review	
	2016-11-22	Attitude Determination and Control System	
	Phase B		

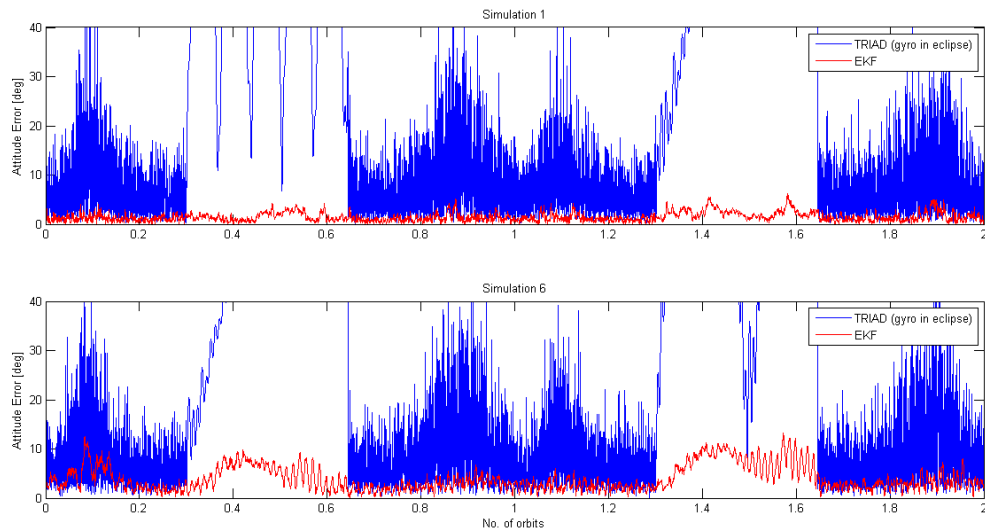


Figure 8-11 Attitude error between EKF & true and TRIAD & true (gyro integration in eclipse) for Sim. 1 & 6, small rotation vector norm

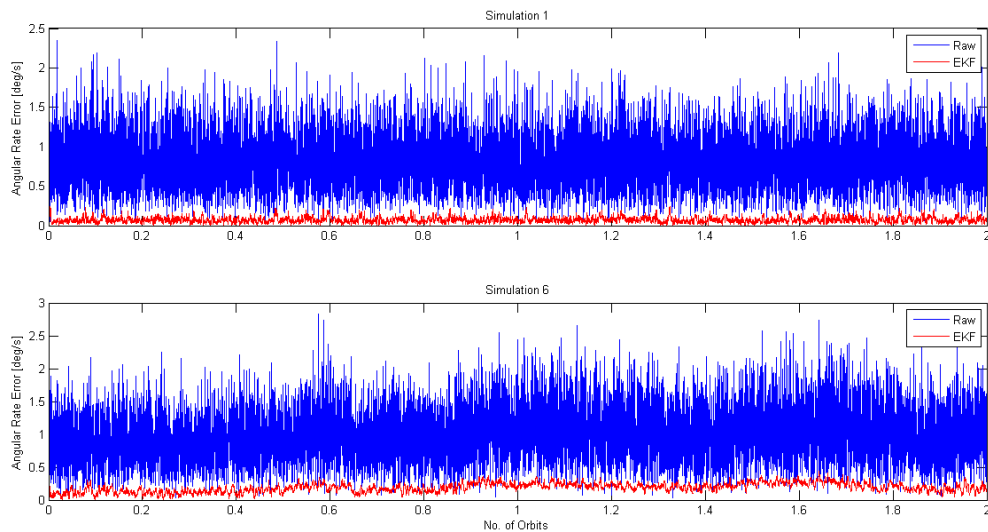




Figure 8-12 Angular rate error between EKF & true and gyro raw data & true for Sim. 1 & 6, vector norm

	PW-Sat2	Preliminary Design Review	
	2016-11-22	Attitude Determination and Control System	
	Phase B		

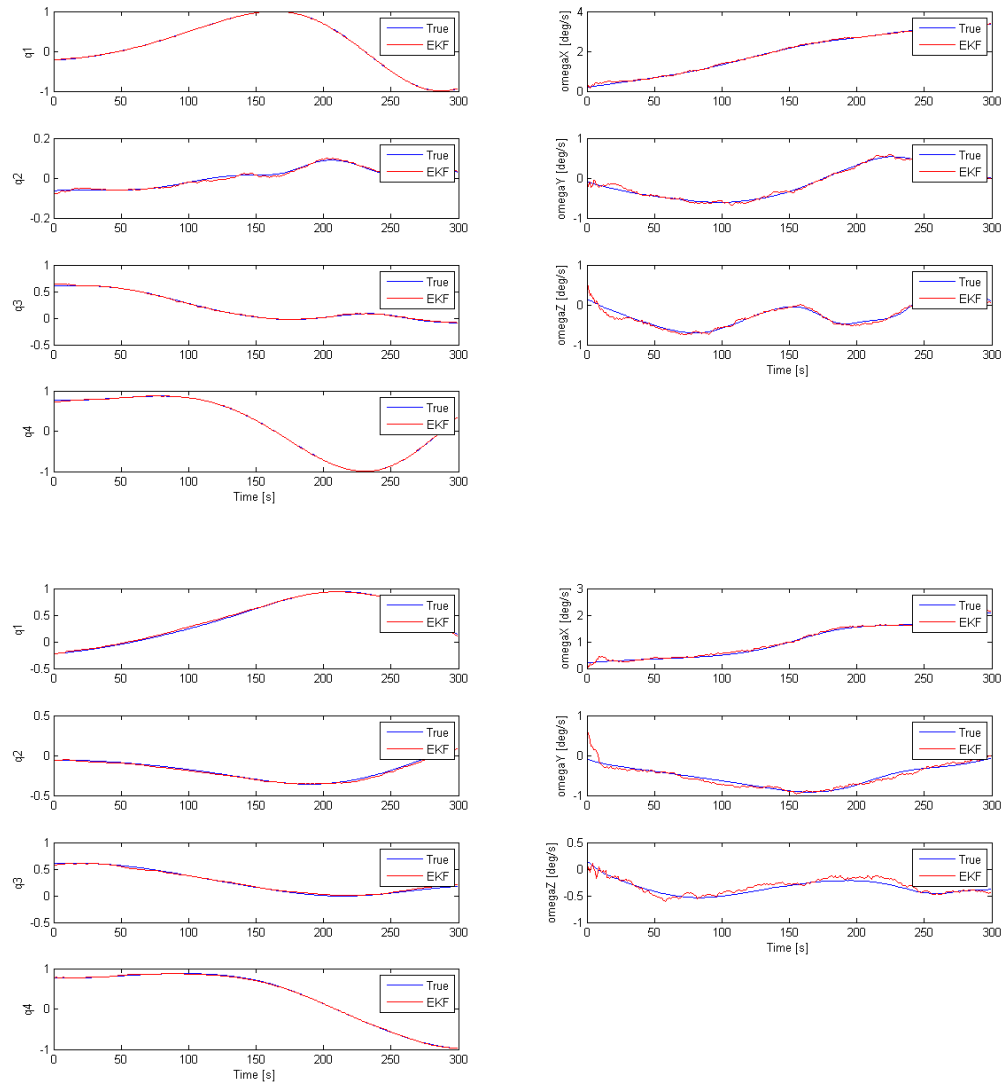




Figure 8-13 EKF convergence in initial 300s for Sim. 1 & 6 in Sun Pointing mode

	PW-Sat2	Preliminary Design Review	
	2016-11-22	Attitude Determination and Control System	
	Phase B		



The table below presents the results comparison for each simulation. The mean values are calculated when the satellite reaches its commanded state, i.e. it tracks the Sun. The range of deviation from the mean values can be seen in the figures above. The mean values are calculated in eclipse and in daylight.

Table 8-3 Sun Pointing mode simulations' results

			Sim. 1	Sim. 2	Sim. 3	Sim. 4	Sim. 5	Sim. 6
EKF Attitude Error [deg]	Daylight		1.4	2.4	9.4	1.1	1.3	3
	Eclipse		2.5	4.1	98.6	1.3	2.2	8.3
EKF Angular Rate Error [deg/s]	Daylight		0.08	0.1	0.31	0.07	0.07	0.19
	Eclipse		0.07	0.1	0.54	0.07	0.07	0.25
Sun Pointing Error [deg]	Daylight		0.8	1	1.1	1.2	0.9	1
	Eclipse		1.4	1.3	1.4	1.6	1.3	1.4
Angular Rate in SBRF [deg/s]	X	Daylight	5.001	5.026	5.228	5.022	5.023	5.022
		Eclipse	4.997	4.991	5.151	5.001	5.028	5.002
	Y	Daylight	0.044	0.046	0.006	0.042	0.052	0.026
		Eclipse	0.059	0.064	0.061	0.068	0.07	0.058
	Z	Daylight	-0.012	-0.015	-0.023	-0.014	-0.012	-0.005
		Eclipse	-0.008	-0.009	-0.01	-0.011	-0.01	-0.009
Total energy consumption after 2nd orbit [Wh]			0.056	0.061	0.073	0.055	0.058	0.064
Power consumption [W]			0.01	0.015	0.028	0.011	0.009	0.013

First of all, it should be noted, that the simulation 6 is not necessarily the worst case scenario. Some errors have greater value in other simulations. This is due to the robustness of the spin stabilization control law and the randomness of the sensors' noise, especially not predictable nature of random walk. The drift utilized in simulation 3 results in significantly greater attitude errors than in simulation 6 in which the drift is accommodated as well.

The EKF attitude error is calculated as the norm of the small rotation vector describing the error between "true" and estimated attitude. The estimated attitude error is greater in eclipse, because the Sun sensor measurement is not available. The filter uses predicted value for Sun sensor measurement, therefore, no correction is incorporated. The filter's sensitivity for gyro drift can be seen in Simulation 3 and 6. The drift is modeled as a random walk, thus its divergence is not predictable. However, the estimated attitude error can be as large as 100°

	PW-Sat2	Preliminary Design Review	
	2016-11-22	Attitude Determination and Control System	
	Phase B		

when the drift is not included in EKF. Only first order term was used in calculating the small rotation vector. For this reason, for greater attitude error, the computed value is less accurate.

The satellite's estimated attitude is less accurate in the parts of the orbit when the Earth's magnetic field is weaker. The magnetometer's noise standard deviation is defined as an absolute value. Therefore, when the Earth's magnetic field is weaker, the magnetometer's relative error is greater.

Satellite's angular rate error is calculated as the norm of the difference between the "true" and estimated angular rate. The greater error can be seen when drift is added. However, the filter's accuracy is comparable in eclipse and daylight.



Sun Pointing error is calculated as the angle between the satellite's X axis and the "true" Sun direction. The error is greater in eclipse, because the magnetorquers are turned off. When control is not applied, the disturbance torques destabilize the rotational movement. The error grows with time, but when the satellite leaves the eclipse, the magnetorquers are turned on and the error is corrected.

The average power consumption is calculated for all 3 magnetorquers. It is relatively low after the satellite is stabilized and small deviations are being corrected. However, for magnetorquer's current control, the PWM will be used. Thus the power corresponding to the magnetic dipole nominal values at 5V should be available at any time (approximately 1W). The energy was calculated recursively, based on power consumption. Calculated value was divided by 3600 to obtain the energy consumption in Wh.

The inertia error does not influence the accuracy of Sun tracking. Also, when one magnetorquer is turned off, the ADCS is still able to track the Sun accurately. However, the time of reaching the commanded state is a bit longer. Other combinations of simulated coils malfunction were tested. They proved that at least two magnetorquers - no matter which ones - are necessary to track the Sun.

The sensitivity of Sun Pointing control law for disturbance torques was tested. The control gains utilized in the control law are dependent on the whole system's dynamics. This refers to the satellite's inertia matrix and the magnitude of the disturbance torques as well. If the models of the disturbance torques are not accurate, then the control gains loaded into the satellite's OBC memory may result in poorer controller performance. Several combinations of turning the disturbance torques on and off were tested. For each simulation, the control gains remained constant. The overall performance was not altered. This proves, that control gains can be calculated on the basis of simulation results.

The Sun Pointing control law needs not more than 30 minutes to track the Sun within 5° accuracy.

	PW-Sat2	Preliminary Design Review	
	2016-11-22	Attitude Determination and Control System	
	Phase B		

8.3.2 DETUMBLING MODE

In the table below, parameters which are variable in 3 simulations for Detumbling mode are presented:

Table 8-4 Variable simulation's parameters for Detumbling mode

Condition	Sim. 1	Sim. 2	Sim. 3
High-pass filter for B-dot on	+	-	+
Y magnetorquer rod off	-	-	+



Simulation 1 tests the nominal Detumbling mode, when all magnetorquers are working and the high-pass filter for B-dot computation is enabled.

Simulation 2 shows the Detumbling mode performance with disabled high-pass filter for B-dot calculation.

Simulation 3 shows the ADCS performance in Detumbling mode with one magnetorquer (Y) off.

For all 3 simulations, constant bias equals $[800 \ 700 \ -650]^T$ nT is added on magnetometer measurements.

On the figures below, the results for each simulation are presented.

	PW-Sat2	Preliminary Design Review	
	2016-11-22	Attitude Determination and Control System	
	Phase B		

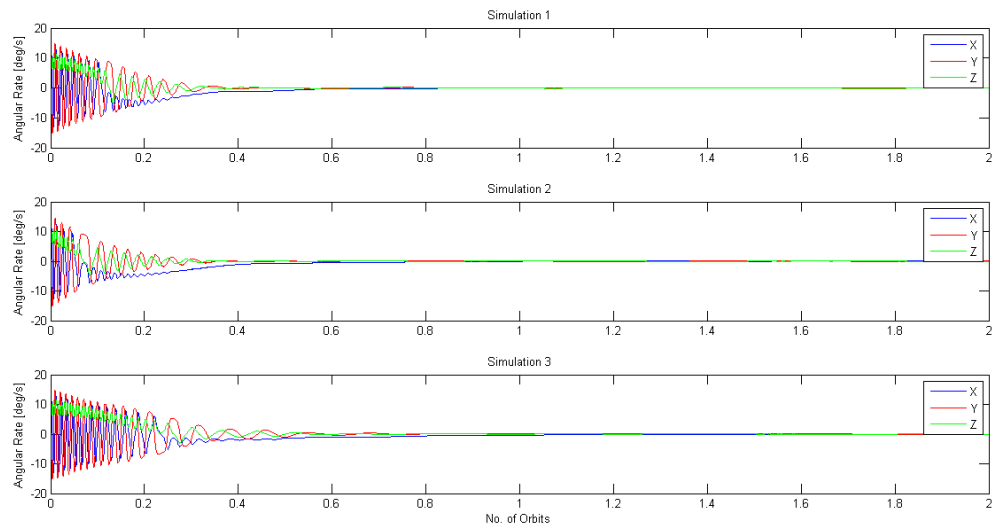


Figure 8-14 Satellite's angular rate in SBRF in Detumbling mode

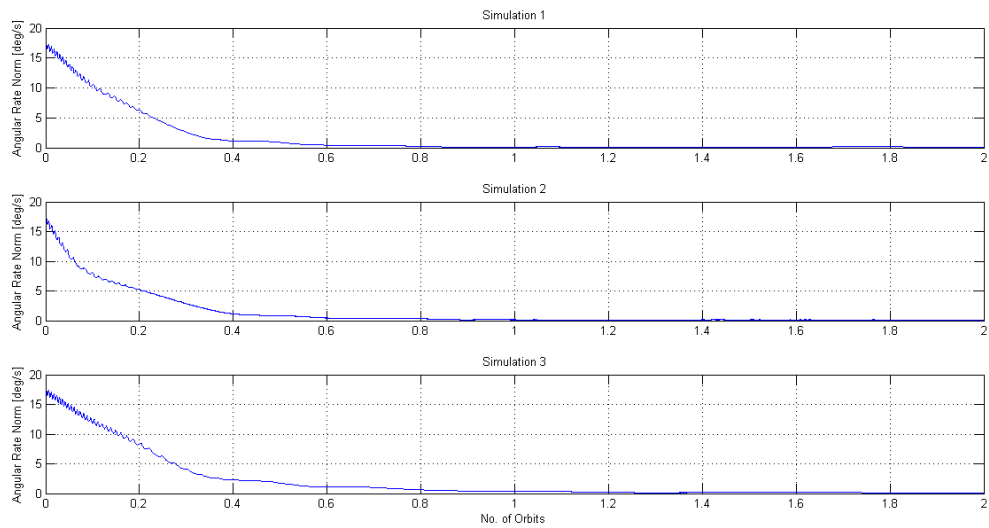


Figure 8-15 Satellite's angular rate vector norm in Detumbling mode

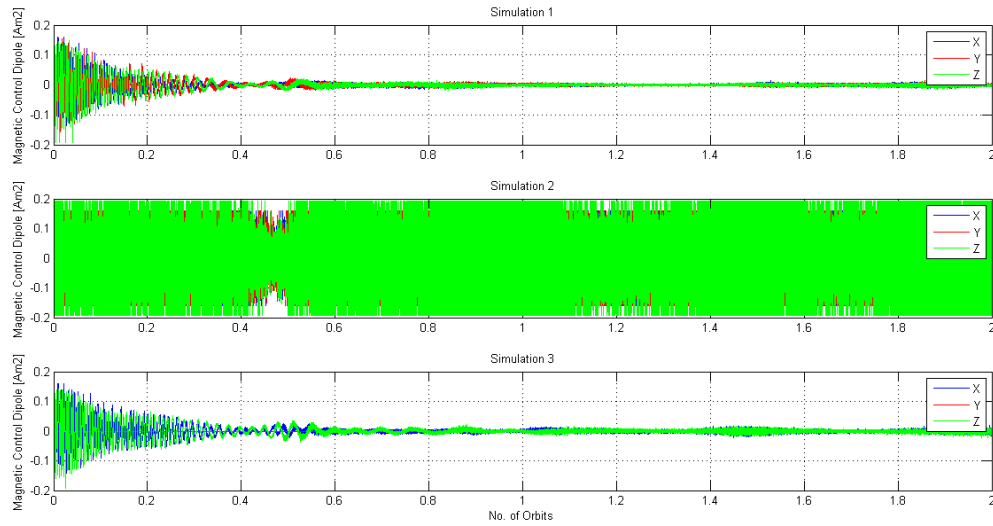


Figure 8-16 Control magnetic dipole in Detumbling mode

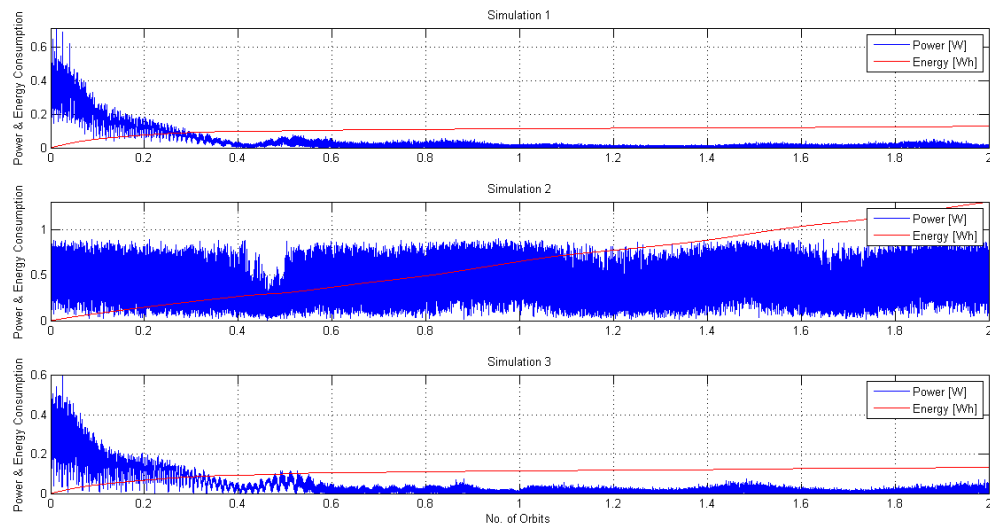




Figure 8-17 Power & Energy consumption in Detumbling mode

	PW-Sat2	Preliminary Design Review	
	2016-11-22	Attitude Determination and Control System	
	Phase B		

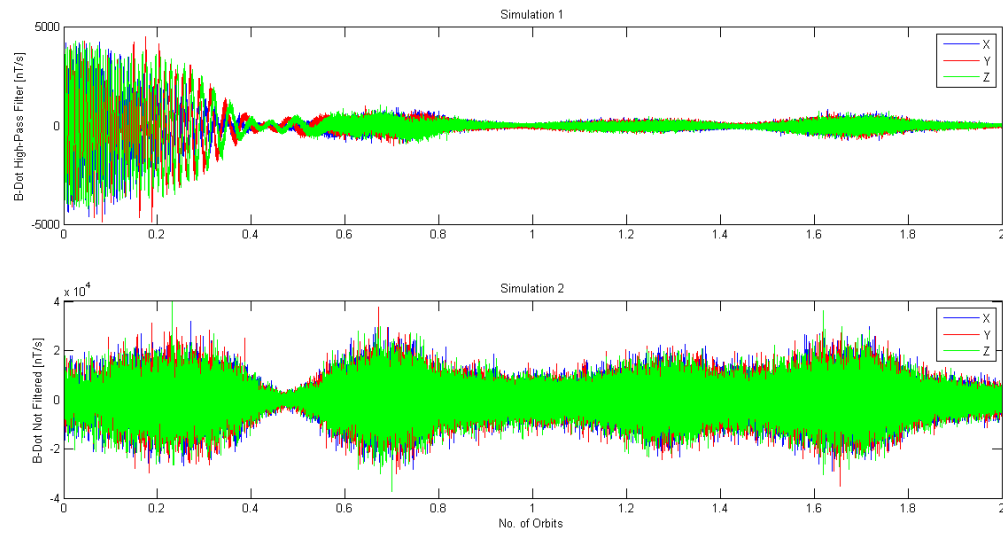


Figure 8-18 B-dot with high-pass filter (top) and without (bottom)

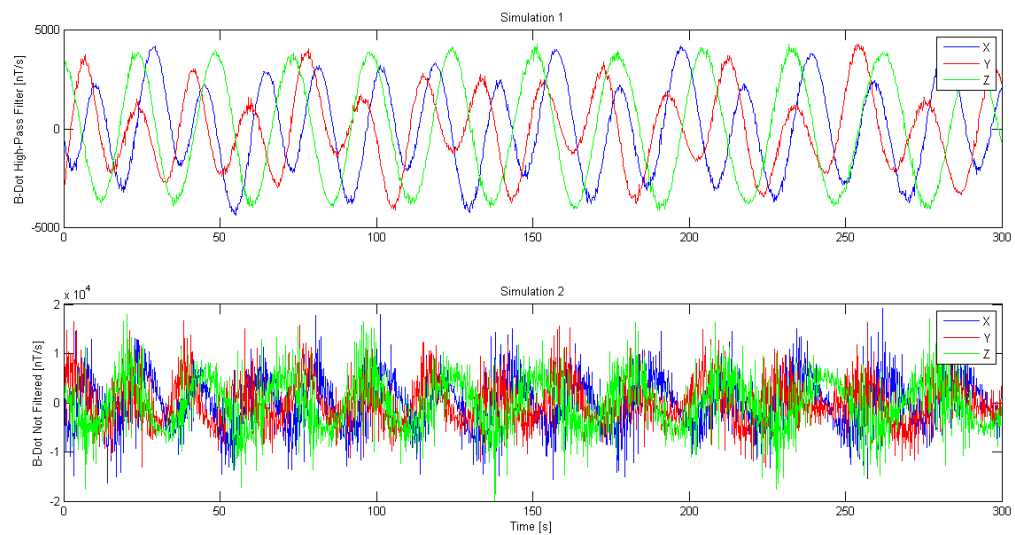




Figure 8-19 B-dot close-up in initial 300s with high-pass filter (top) and without (bottom)

	PW-Sat2	Preliminary Design Review	
	2016-11-22	Attitude Determination and Control System	
	Phase B		

The table below presents the results comparison for each simulation. The mean values are calculated during the 2nd orbit, after detumbling is finished.

Table 8-5 Detumbling mode simulations' results



	Sim. 1	Sim. 2	Sim. 3
Angular Rate Vector Norm	0.12	0.1	0.17
Total energy consumption after 2nd orbit [Wh]	0.128	1.313	0.134
Power consumption after detumbling [W]	0.009	0.409	0.012
Energy consumption per orbit after detumbling [Wh/orbit]	0.014	0.66	0.02

Satellite's angular rate after detumbling is relatively slow. The B-Dot control law tends to minimize the derivative of the Earth's magnetic field calculated in the satellite's frame. Due to the change of Earth's magnetic field vector's direction, the satellite will follow the Earth's magnetic field vector. The angular rate of Earth's magnetic field vector is approximately 0.15°/s. It can be seen that after detumbling the satellite's angular rate is approximately equal this value.

The power consumption after detumbling is relatively low when high-pass filter is used. When the high-pass filter is turned off, the power consumption is approximately 40 times greater. In this case, the coils are constantly saturated. This is due to the noisy B-dot computation. The advantage of the high-pass filter is presented in the Figure 8-18 and Figure 8-19. The Figure 8-19 presents close-up of B-dot computation for initial 300s of detumbling. It can also be seen that the magnitude of noisy B-dot computation is approximately 4 times greater in initial phase and 50 times greater after detumbling. When the satellite's angular rate is smaller, the poorer performance of high-pass filter can be seen in Figure 8-18. This is due to the damping of lower frequencies by the high-pass filter.

The time of detumbling is not influenced by high-pass filter turning on or off. However, it is influenced on the number of active coils. When all 3 coils are working, the detumbling time equals approximately 45 minutes. With one coil turned off, the time of detumbling does not exceed 1 orbit ~96min.

Other combinations of simulated coils malfunction were tested. They proved that at least two magnetorquers - no matter which ones - are necessary in Detumbling mode.

	PW-Sat2	Preliminary Design Review	
	2016-11-22	Attitude Determination and Control System	
	Phase B		



9 CONCLUSIONS

In this document, the proposed ADCS architecture in Phase A was refined and verified. Attitude determination and estimation algorithms were tested with greater than expected sensors' noise. Control algorithms for spin stabilization and detumbling were implemented as well and tested, assuming certain set of errors.

Simulations results presented in chapter 8 prove that proposed ADCS design is feasible. Sun Pointing control mode is robust for sensors' noise, inertia matrix error and one coil malfunction. The Sun tracking error is less than 2° . This results in 99,9% of solar energy reaching the solar panels. The sensors' errors magnitude were modeled approximately 2 times greater than expected based on the datasheets. The accuracy of the satellite's attitude and angular rate estimation using MEKF is satisfactory. However, the attention has to be paid to unmodeled sensors' errors. The gyroscope drift and the constant bias make the MEKF performance poorer. Especially the gyro's error influence MEKF significantly. The team has to investigate the possibility of adding the sensors' biases into the state vector. Adaptive and Unscented Kalman filters should be tested in order to accommodate correlated sensors' noise. The possible divergence of MEKF will be investigated as well as methods to monitor the covariance matrix \underline{P} and reset the filter when covariance matrix elements exceed some predetermined limit.

The B-dot algorithm utilized in Detumbling mode proves to be robust for magnetometer's error and one coil malfunction. The high-pass filter is necessary in order to reduce the power consumption.

Proposed ADCS architecture satisfies the requirements presented in chapter 3 with significant safety range. The real ADCS accuracy is expected to be worse but within the accepted error region. Simulations results show that the Sun Pointing control law and the B-dot algorithm are very robust for broad range of errors. Therefore, the Sun pointing error and time of detumbling, which are major ADCS performance requirements, are proven to be within an expected bounds.

	PW-Sat2	Preliminary Design Review	
	2016-11-22	Attitude Determination and Control System	
	Phase B		

10 FUTURE WORK



Several issues has to be specified before the whole ADCS design is confirmed. Future work will focus on testing the sensors and actuators. Expected noise and overall accuracy has to be determined in order to tune the MEKF properly. After testing several types of sensors, final decision about the hardware will be made. The team will determine whether the external magnetometer and reference Sun sensor will be bought. The photodiodes configuration will be chosen and optimized. Expected sensors' errors will be modeled in Kalman filter and set of simulations will be run in order to determine the ADCS performance. In the simulation software, the sensors' noise should be altered in order to accommodate the correlated noise. Adaptive and Unscented Kalman filters will be tested and compared with simple EKF equations. The state vector should include the sensors' biases.

However, it may happen that the proposed approach will be too computationally demanding for the OBC's capabilities. In this case, the trade-offs will be proposed. For instance, the calibration of the magnetometer doesn't need to be performed in real time Kalman filter formulation. Adding more state vectors elements requires more computational load. The calibration can be performed in initial phase or sequentially, after some predetermined period. For on-orbit magnetometer calibration, the widely used TWOSTEP algorithm can be utilized [1].

When the exact ADCS architecture will be determined and verified, the algorithms will be rewritten on the OBC's microcontroller. TLE algorithm for orbit propagator (not used so far) will be tested and loaded on-board. The transitions between the ADCS modes will be programmed as well.

The team will also focus on the ADCS telemetry and telecommand data structure. Data sent to the ground will let the team estimate the ADCS performance and overall accuracy.

Issues presented above will be realized until September 2015, i.e. the end of Phase C.

	PW-Sat2	Preliminary Design Review	
	2016-11-22	Attitude Determination and Control System	
	Phase B		

11 APPENDIX A COORDINATE SYSTEMS

In this document, three Cartesian coordinate systems are used. These are: ECI inertial frame, orbital frame and satellite's body frame denoted with subscripts i , o and s , respectively.

ECI – Earth Centered Inertial

Fixed, inertial coordinate system $O_i x_i y_i z_i$ which origin coincides with the Earth's center of mass. The $O_i z_i$ axis is collinear with the Earth's axis of rotation and points towards North Pole. The $O_i x_i y_i$ plane coincides with the Earth's equatorial plane, the $O_i x_i$ axis is fixed at the vernal equinox and the $O_i y_i$ axis completes the right handed cartesian coordinate system. ECI inertial frame is pseudo inertial, i.e. its origin accelerates and the axes change their orientation in space due to the Sun and Moon perturbations. However, these effects can be neglected in most navigation applications.

ORF – Orbital Reference Frame

The origin and the axes orientation of the orbital frame $O_o x_o y_o z_o$ depend on the satellite's position on orbit. Its origin O_o coincides with the satellite's body frame origin O_s . The $O_o z_o$ axis points toward the center of the Earth, O_i . The $O_o x_o$ axis lies in the orbital plane and is collinear with the satellite's velocity vector for circular orbits. The $O_o y_o$ axis completes the right handed coordinate system $O_o x_o y_o z_o$ and is perpendicular to the orbital plane.

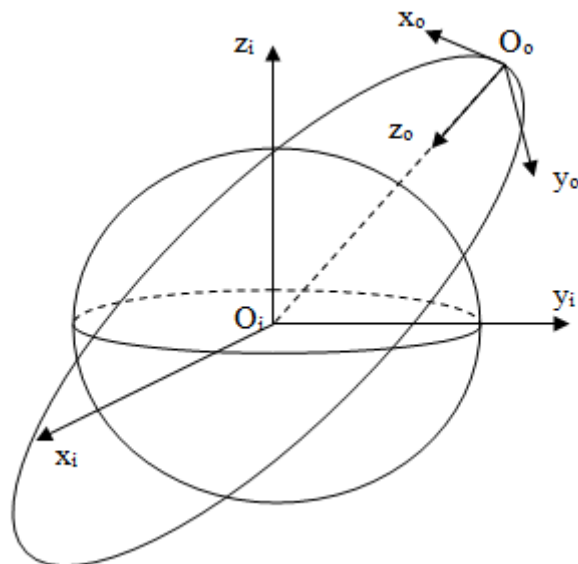




Figure 11-1 ECI inertial and ORF orbital coordinate systems

	PW-Sat2	Preliminary Design Review	
	2016-11-22	Attitude Determination and Control System	
	Phase B		

SBRF – Satellite's Body Reference Frame

The SBRF coordinate system $O_s x_s y_s z_s$ is fixed with reference to the satellite. The origin O_s coincides with the satellite's center of mass. The $O_s x_s$ axis is perpendicular to the deployed solar panels and points outwards. The $O_s z_s$ axis is parallel to the deployed solar panels' plane and points towards the communication antennas. The $O_s y_s$ axis completes the right handed coordinate system $O_s x_s y_s z_s$. In the figure below, the SBRF's origin is moved away from the satellite for clarity.

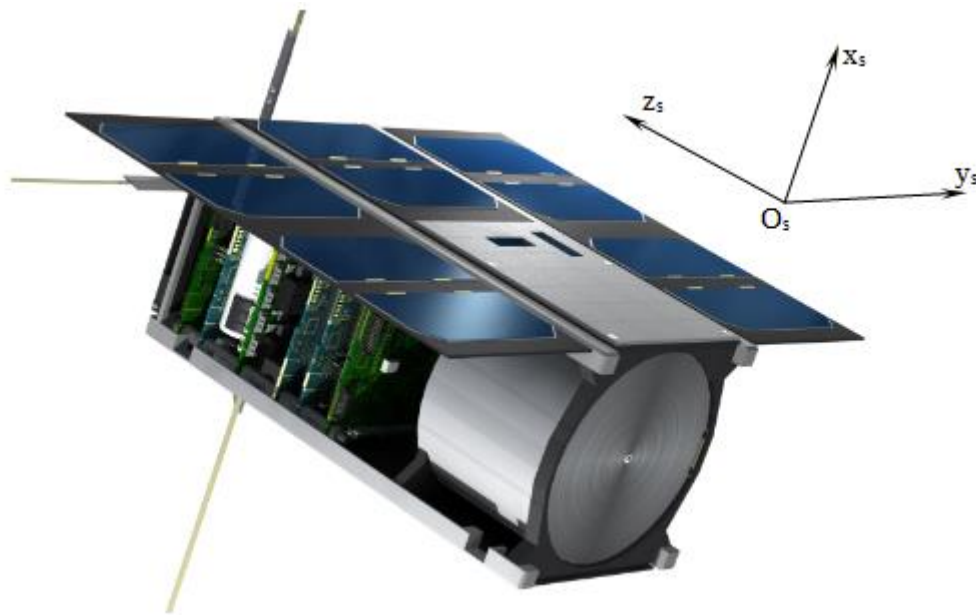






Figure 11-2 SBRF satellite's body coordinate system

	PW-Sat2	Preliminary Design Review	
	2016-11-22	Attitude Determination and Control System	
	Phase B		

12 APPENDIX B NOMENCLATURE

In this appendix, the mathematical notation used in this document is described.

1. Bold font describes vector, e.g. \mathbf{a}
2. Bold font, capital letter and the underline describe matrix, e.g. $\mathbf{\underline{B}}$, however the matrix $\mathbf{\underline{A}}$ is reserved for orthogonal transformation matrices
3. Left superscript describes the coordinate system in which the vector is expressed, e.g. ${}^s\mathbf{a}$
 - 3.1. 'i' – ECI inertial frame
 - 3.2. 'o' – ORF orbital frame
 - 3.3. 's' – SBRF satellite's body frame
4. Matrix ${}^s\mathbf{\underline{A}}$ describes the rotation from coordinate frame denoted 'i' to the 's' coordinate frame
5. Quaternion ${}^s\mathbf{q}$ describes the rotation from coordinate frame denoted 'i' to the 's' coordinate frame
6. Transformation matrix formed from a quaternion ${}^s\mathbf{q}$ is denoted ${}^s\mathbf{\underline{A}}(\mathbf{q})$
7. The angular rate vector of a 's' coordinate system relative to 'i' coordinate system is denoted $\boldsymbol{\omega}_{s/i}$
8. The element in i -th row and j -th column in matrix $\mathbf{\underline{B}}$ is denoted $\mathbf{\underline{B}}(i, j)$
9. Skew-symmetric 3x3 matrix formed with the 3x1 vector's \mathbf{a} components is denoted $[\mathbf{a}\times]$

	PW-Sat2	Preliminary Design Review	
	2016-11-22	Attitude Determination and Control System	
	Phase B		

13 REFERENCES

-
- [1] F. L. Markley, J. L. Crassidis, *Fundamentals of Spacecraft Attitude Determination and Control*, Springer 2014
 - [2] M. J. Sidi, *Spacecraft Dynamics & Control, A Practical Engineering Approach*, Cambridge University Press, 1997
 - [3] J. F. Kasper, V. Kasper, *Attitude Determination and Control System for AAUSat3, Master Thesis*, Aalborg University 2010
 - [4] A. Slavinskis, U. Kvell, E. Kulu, I. Sunter, H. Kuuste, S. Latt, K. Voormansik, M. Noorma, *High Spin Rate Controller for nanosatellites*, Acta Astronautica 95 (2014)
 - [5] OSRAM SFH2430 Photodiode Datasheet v.1.0
 - [6] CubeMagnetometer, ESL, Interface Control Document
 - [7] G. Michalareas, S. B. Gabriel, E. Rogers, *Spacecraft Attitude Estimation based on Magnetometer Measurements and the Covariance Intersection Algorithm*, University of Southampton
 - [8] J. C. Springman, J. W. Cutler, *Photodiodes Placement & Algorithms for CubeSat Attitude Determination*, CubeSat Developer's Workshop 2012
 - [9] ISIS Magnetorquer Board User Manual, v.1.1 2011
 - [10] SSBV Cubesat Sun Sensor Datasheet
 - [11] XEN1210 Magnetic Sensor Datasheet, v.1.7 2013
 - [12] J. C. Springman, J. W. Cutler, *Initial Attitude Analysis of the RAX Satellite*
 - [13] Analog Devices ADXRS453 Gyroscope Datasheet, rev.B
 - [14] D. Air, S. Claridge, *Surface Albedo Estimation*
 - [15] P. Furła, M. Kwas, J. Toruniewska, *Słonecznik – Symulator Słońca do Komory Próżniowej, Sprawozdanie merytoryczne*, Warszawa 2012
 - [16] A. Łukasik, *Construction of a test stand for satellite's attitude determination system tests, Bachelor Thesis*, Warsaw 2014
 - [17] T. S. Kelso, *Validation of SGP4 and IS-GPS-200D Against GPS Precision Ephemerides*, 17th AAS/AIAA Space Flight Mechanics Conference, Arizona 2007
 - [18] International Association of Geomagnetism and Aeronomy, Working Group V-Mod, *International Geomagnetic Reference Field: the eleventh generation*, Geophysical Journal International, September 2010
 - [19] AzurSpace 28% Triple Junction GaAs Solar Cell Datasheet 2012
 - [20] C. Fruh, T. M. Kelecý, M. K. Jah, *Attitude Dynamics Simulation of MLI Space Debris Objects in Geosynchronous Earth Orbits*